Microwave Magnonics at Millikelvin Temperatures

Sandoko Kosen
St Cross College
University of Oxford

A thesis submitted for the degree of
Doctor of Philosophy

Trinity 2019

Abstract

This thesis reports on three recent experimental studies of microwave magnons in yttrium iron garnet (YIG) systems at millikelvin temperatures.

We begin with an introduction to the emerging field of quantum magnonics and its underpinning motivations. Basic theory of dipolar spin-wave or magnon dynamics in various sample geometries is presented. This introduction is followed by a brief description of the specificities of our experimental setup and properties of YIG — the magnetic material used in our studies.

The first experiment involves a hybrid system combining a YIG sphere and a niobium-based superconducting planar resonator. The device is measured at millikelvin temperatures and signals of strong magnon-photon coupling are observed when the excitation energy is at the level of single photons. The superconducting resonator is shown to maintain a good quality factor even under sizeable in-plane magnetic field that is required to support the excitation of magnons in YIG.

The second experiment demonstrates the operation of a magnonic crystal based on an etched YIG film at millikelvin temperatures. A magnonic bandgap is successfully observed both under continuous- and pulsed- microwave excitation. High magnon damping is observed in the device at low temperature.

The third experiment involves the measurement of magnon damping in YIG films. Comparisons between results from different samples and at different temperatures provide insight into the role of the substrate and two-level fluctuators at low temperature. A brief review of the known damping processes in bulk YIG from room temperature down to millikelvin temperature is also presented.

The final chapter summarises results in this thesis and suggests possible future research directions.

Personal Note

The time spent in Oxford is one of the best I've ever had in my life. The city, the school, and the people — they have truly coloured my experience in various ways and shall leave an indelible memory for me. I came to this place to pursue my intellectual curiosity in physics. Deliberately, I chose a topic that has almost zero overlap with my past works, with the full intention to explore a new research direction. Unsurprisingly, the journey is a challenging one, but it was a fun one as well. Totally enjoyed it. More importantly, I hope that it will make impactful contribution to the field in any way it can. This thesis is the culmination of this adventure. I owe it to a number of individuals and institutions to acknowledge their contributions in making this work possible.

First of all, I would like to thank Dr Alexy Karenowska, my supervisor, for giving me the opportunity to work in this emerging field. She has been supportive in allowing me to grow as an independent researcher. I'm still sorry for unintentionally breaking the newly-bought YIG disc, for in the spur of the moment, I forgot that magnet attracts ferrite! Her feedbacks have helped turn this thesis into a more readable version as it is now, occasionally suggesting words that I would've never thought of using in a million lifetimes. The enthusiasm she displayed in exploring unconventional fields using physics is exemplary and I shall always be inspired by that.

The second person to thank is Dr Arjan van Loo, the postdoctoral researcher that I have worked with throughout my time in the group. His unmatched word nitpicking skill is very impressive — sometimes making me wonder if it should be considered as a superpower instead. He is always available to give me advice when I am stuck and is ready to criticise when my work is sloppy — for that, I am really grateful. His comments on the early draft of this thesis are also critical in shaping its structure. Equally important, he has successfully made drinking coffee — perhaps his most favourite drink after water — to be a daily routine for me. I shall forever remember the jiggling sound of a coffee pod in a mug that he made to signal the time for coffee! For the record, I just drank another cup of coffee after writing this paragraph.

The next person in line is Dr Richard Morris, the lab partner-in-crime that I worked with during my first two years in Oxford. He has been very helpful

with introducing me to many things in the lab and other lab-related routines. I promise to remain ‘still alive’ for many decades to come; unfortunately though, I may not have the opportunity to pass on the legacy of ‘Extreme Magnonics’ to future group members!

I would like to thank Prof John Gregg, for allowing me to use the room-temperature magnet facility — it is critical in producing all of the room-temperature results in this thesis. To our collaborators at Kaiserslautern — Dr Andrii Chumak, Dr Dmytro Bozhko, and Ms Laura Mihalceanu — your feedbacks and samples have been important in my works. To all magnonicians in 174: thank you for always being there to discuss anything about magnons. To all officemates in 105: you are all really awesome and I regret not spending enough time with you — I will make up for it somehow in the future!

To Prof Stephen Blundell and Prof Silvia Viola-Kusminskiy, thank you for agreeing to be the examiners of my thesis. I am grateful for the comments and suggestions that have helped me correct a number of errors and also make this thesis more readable!

On an even more personal level, I am immensely grateful to both my parents and family for their unwavering support throughout all this time — *Kam Sia* very much! On all non-physics related discussions, I have the Indonesian community in Oxford — especially everyone at PPI Oxford — to thank for. I benefited a lot from your constant companion — you taught me many things and have been (reasonably) successful in keeping me sane when I was one step away from going crazy over things that didn’t work in the lab. *Terima Kasih!*

Financial support from taxpayers in Indonesia (Indonesia Endowment Fund for Education, for funding my education), taxpayers in United Kingdom (EPSRC for funding the research), APS GMAG (travel fund for the 2019 Joint MMM-Intermag conference), and St Cross College (travel fund for the 2019 APS March Meeting) is gratefully acknowledged.

Last but not least, to all magnons$_{\text{(minions)}}$ that have been unintentionally involved in our experiments, thank you for being there! ☺

Contents

1

Introduction

Magnons or spin waves are phase-coherent precessional excitations of spins in a magnetically ordered system (illustrated in fig. 1.1) [1]. The phase difference $\Delta\phi$ between the precessional angle of neighbouring spins determines the corresponding wavelength (λ) and wavenumber ($k = 2\pi/\lambda$). If all spins precess in phase ($k = 0$), the excitation is called a uniform precession mode (Kittel mode). While the terms “spin wave” and “magnon” describe the same collective phenomenon, the former is commonly used to describe its wave-like nature and the latter to describe its corpuscular nature. In this thesis, both are used interchangeably depending on the context.

Since their first observation by Griffiths in the Clarendon Laboratory more than 70 years ago [2], a large body of work has grown up around spin waves, encompassing both their basic physics and technological applications [1, 3–16]. Enthusiasm for

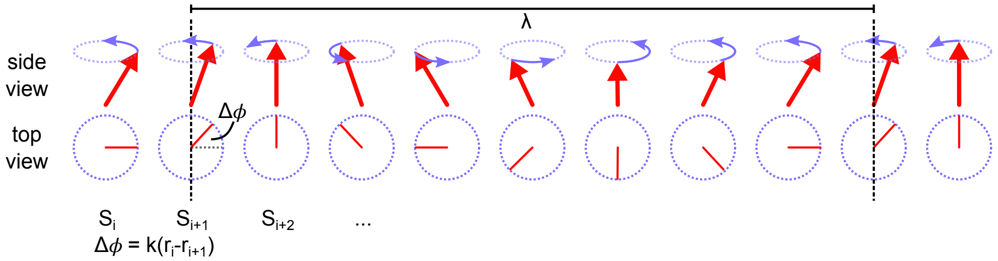

Figure 1.1: Illustration of a 1D array of precessing spins. Such excitations are called magnons or spin waves.

experimental magnon dynamics has been largely driven by their exceptionally rich dispersive properties and the availability of materials with low magnetic damping, notably the electrically-insulating ferrimagnet yttrium iron garnet (YIG). Spin waves can be excited and observed across a wide range of frequencies – from high megahertz to terahertz-regime – with wavelengths typically being much smaller than photons of the same frequency in vacuum. These unique properties have motivated the search for miniaturised magnon-based devices that are fast and energy-efficient, and catalysed the emergence of the field now known as *magnonics*. Notable works in this area include the creation and study of: room-temperature condensates of magnons [17], magnon transistors [18], and systems for all-linear time-reversal of signals [19].

In recent years, there has developed increasing interest in combining magnonic systems with other microwave-frequency structures. The goal is to realise *hybrid* devices that combine the best features of both constituent systems, with a view to achieve novel technological functionality, and access new basic physics. For instance, there is much interest in coupling magnons to microwave photons in cavities as well as to optical photons. The former gives rise to so-called microwave cavity-magnon polaritons, which have been used to explore the fascinating physics of coupled oscillators [20]. Coupling magnons to optical photons is important from a technological point of view as it opens up a potential path to microwave-to-optical conversion [21–26]: a much sought-after goal in the context of the quest to efficiently transfer quantum information between spatially-separated and/or operationally distinct quantum nodes (or systems) [27].

The work in this thesis concerns a class of hybrid magnonic systems that holds particular promise: the combination of microwave magnon-based systems with superconducting circuits. Superconducting circuits are considered to be one of the most promising candidates for the implementation of a fully functioning solid-state quantum computer and form the focus of the field known as circuit quantum electrodynamics (QED) [28]. Through the realisation of new magnon-based quantum devices based on superconducting circuits, the highly sensitive control and measurement techniques developed in the context of circuit QED can be used to explore the physics of magnons at the quantum level.

In this emerging field of *quantum magnonics*, two approaches have thus-far been used to couple magnons to quantum circuits. In the first, a *standing-wave* magnon excitation in *bulk* YIG is coupled to an aluminium-based superconducting circuit via virtual photons within a three-dimensional microwave cavity. This approach was successfully demonstrated for the first time by the group of Y. Nakamura in Japan [29–32]. In the second, a *travelling* magnon excitation in a YIG *film* is coupled to a planar superconducting circuit. It is this 2D approach that motivates the work detailed in this thesis. The 2D-travelling wave architecture is highly challenging to realise because of the need to locate a magnon-bearing magnetic structure in close proximity to a superconducting thin film. The moderate magnetic field required to magnetically bias such a structure ($\sim$100 mT in the case of a YIG film) rules out the use of aluminium-based superconducting circuits (the most common and well-developed technology in the context of mainstream circuit QED) due to aluminium's low critical field (see Chapter 4 and [33]). For this reason, in our work we employ niobium-based superconducting circuits. Niobium, being a type II superconductor, is much more magnetic-field tolerant and has a significantly higher critical field.

In comparison with the 3D-cavity approach which is somewhat restricted in the device functionalities it is able to support, 2D-circuits allow for the easy fabrication of a wide variety of structures with different functionalities within a single chip. This opens doors to both quantum-optics-like experiments exploiting the peculiar dispersion relation of magnons in YIG films and to new technology for use in quantum computing.

To ensure that quantum-level signals within a superconducting circuit are not drowned out by thermal phonons, it has to be operated at very low temperature. In practice, microwave-frequency quantum circuits are usually cooled down to the millikelvin temperature range ($k_\mathrm{B}T \ll hf$). If a hybrid quantum system consisting of a YIG film and a superconducting circuit is to be successfully realised, it is crucial to understand the behaviour of magnons in YIG films at these millikelvin temperatures. The work presented in this thesis represents some of the very first steps in developing the knowledge required to progress this emerging field.

First, we report on strong coupling between standing-wave magnon modes in a YIG *sphere* with standing-wave photons in a superconducting *planar* resonator. The superconducting resonator is shown to retain a sufficiently good quality factor at the typical field required to excite magnons. This result opens up the path for us into incorporating a non-linear element into the superconducting device and couple it to magnon-based systems in the future. Secondly, we give an account of the first measurement of a YIG-based magnonic crystal (an artificial crystal structure in a YIG *film*) at millikelvin temperatures. This measurement allows to assess the potential of using YIG-based magnonic crystals for magnon-based quantum devices. The high damping observed in our YIG-based magnonic crystal measurements inspired us to further investigate the nature of magnon damping in YIG films. Against this background, the third and final investigation presented in this thesis represents the first comprehensive study of magnon damping in YIG films at millikelvin temperatures. Our results highlight additional damping mechanisms in typical YIG films that are not present in bulk or at higher temperature regime, which have to be addressed if YIG film-based devices are to fulfill its potential for quantum applications.

2

Theory of Dipolar Spin Waves

This chapter introduces the basic theory of dipolar spin waves or magnons in several material and field geometries relevant to the experimental work presented later. The discussion draws heavily from Refs. [34–37].

2.1 Introduction

We focus on the properties of so-called dipolar or "magnetostatic" spin waves that can be externally (as distinct from thermally) excited in a magnetic material. Dipolar waves have wavelengths much smaller than the wavelength of free-space electromagnetic radiation of the same frequency, i.e. $\lambda_\mathrm{m} \ll \lambda_\mathrm{f}$, but not so small as to be significantly influenced by the short-range exchange interaction between neighbouring spins. At this length scale, spin-wave dynamics are mainly governed — as the name suggests — by the relatively long-range magnetic-dipolar interaction.

In the case of ferromagnetic materials supporting dipolar spin-wave propagation, the exchange interaction is assumed only to produce the long-range order necessary to align neighbouring magnetic dipoles. When the spin-wave wavelength is small enough to be comparable to the exchange length of the material, the exchange interaction begins to influence the dynamics. This places a lower bound on the wavelength of spin waves that can be analysed by the method presented below. To further understand the role of the exchange interaction in the spin-wave dynamics, readers are referred to Refs. [38] and [34] for more information.

The approach we shall adopt here is to first obtain the response of the magnetic material (i.e. its magnetic permeability tensor) under the presence of a magnetic field. The permeability tensor will then be incorporated into the Maxwell equations from which we can derive expressions for all the various fields that can exist inside the material. Finally we shall show that one part of this solution corresponds to dipolar spin waves, the main focus of this chapter.

In the following, the material we consider is assumed to be *electrically insulating*, *isotropic*, and *magnetically saturated* by the application of an external bias field. In the first instance, the material is considered to be infinite in size such that the boundary effect can be conveniently ignored in the analysis. The second part of the chapter deals in more detail with the effect of finite sample size.

2.2 Linearised equation of motion

As a starting point, we consider a magnetic material that is saturated by an externally-applied constant bias field $\mathbf{H}_0$ [1]. The material can be thought as a three-dimensional lattice of magnetic dipoles. Each lattice node has a magnetic moment $\mathfrak{m}_i = \gamma \mathbf{J}_i$ where $\mathbf{J}_i$ is the angular momentum, γ is the gyromagnetic ratio, and i denotes the position of that node. The gyromagnetic ratio for all magnetic ions in the S state (an appropriate model for YIG) can be approximated as the gyromagnetic ratio of a free electron, i.e. $|\gamma/2\pi| \approx e/2\pi m_e \approx 28\,\mathrm{GHz/T}$ [34].

Suppose that the magnetic dipoles are perturbed from equilibrium. In such a case, each experiences a torque which in turn causes it to precess around the bias field as illustrated in fig. 2.1(a). The equation of motion that governs the dynamics is [39, 40]

$$\frac{d\mathbf{J}_i}{dt} = \mu_0 \mathfrak{m}_i \times \mathbf{H}(\mathbf{r}_i, t), \tag{2.1}$$

---

[1] For mathematical convenience, we work in terms of H-field rather than B-field. For an externally applied magnetic field H, the corresponding magnetic flux density or B-field is $B = \mu_0 H$.

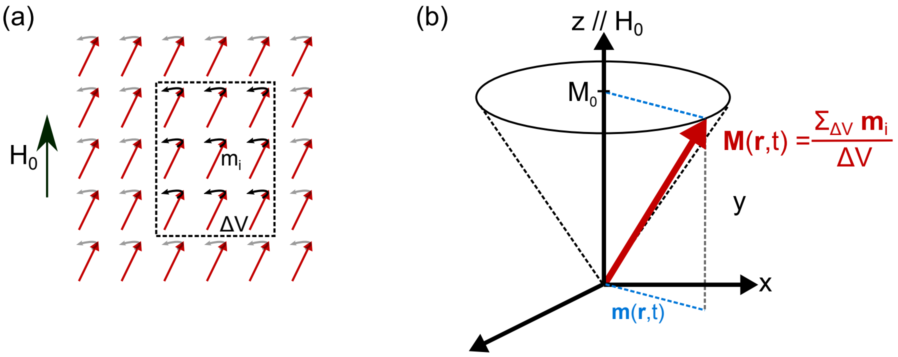

Figure 2.1: (a) Illustration of a two-dimensional array of magnetic dipoles precessing around an external bias field H_0. (b) Illustration of a magnetisation vector $\mathbf{M}(\mathbf{r},t)$ precessing around $\mathbf{H}_0 = H_0\mathbf{e}_z$. The small-signal magnetisation $\mathbf{m}(\mathbf{r},t)$ is the projection of $\mathbf{M}(\mathbf{r},t)$ on the xy-plane, and is assumed to be much smaller in magnitude than the latter.

where $\mu_0/4\pi = 10^{-7}\,\text{H/m}$ is the vacuum permeability and $\mathbf{H}(\mathbf{r}_i,t)$ is the magnetic field at the position of the dipole.

At this point, we transition into a continuum description of the magnetic material by defining a magnetisation vector $\mathbf{M}(\mathbf{r})$ that quantifies the average volume density of magnetic moments at position $\mathbf{r}$, i.e.

$$\mathbf{M}(\mathbf{r}) = \frac{\Sigma_{\Delta V}\mathfrak{m}_i}{\Delta V}, \tag{2.2}$$

where $\Sigma_{\Delta V}\mathfrak{m}_i$ is the sum of magnetic moments in a small volume ΔV around position $\mathbf{r}$. The corresponding equation of motion that governs the magnetisation vector is obtained by taking a volume average of eq. (2.1),

$$\frac{\partial \mathbf{M}(\mathbf{r},t)}{\partial t} = \gamma\mu_0 \mathbf{M}(\mathbf{r},t) \times \mathbf{H}_{\text{eff}}(\mathbf{r},t). \tag{2.3}$$

It should be noted that eq. (2.3) does not incorporate any damping mechanism (i.e. the magnitude of $\mathbf{M}(\mathbf{r},t)$ is conserved; $\frac{\partial}{\partial t}|\mathbf{M}(\mathbf{r},t)|^2 = 0$). Damping is commonly introduced using the phenomenological *Gilbert* damping model where the damping linewidth linearly scales with the resonance frequency with a proportionality constant α (commonly referred to as the Gilbert damping constant) [35]. In line with standard practice, $\mathbf{H}$ in eq. (2.3) has been replaced with an *effective field* $\mathbf{H}_{\text{eff}}$. This allows us to incorporate, where appropriate, the magnetocrystalline anisotropy and the exchange interaction, by defining an effective field corresponding to each interaction term and parcelling them in $\mathbf{H}_{\text{eff}}$ [34].

In the following, we shall consider only the external bias field $\mathbf{H}_0$ and the dipole field within the magnetic material $\mathbf{h}(\mathbf{r},t)$. The vector $\mathbf{M}(\mathbf{r},t)$ can be expressed in terms of a steady-state component $\mathbf{M}_0$ (parallel to $\mathbf{H}_0$) and a small-signal component denoted by $\mathbf{m}(\mathbf{r},t)$ as illustrated in fig. 2.1(b); i.e.,

$$\mathbf{M}(\mathbf{r},t) = \mathbf{M}_0 + \mathbf{m}(\mathbf{r},t). \tag{2.4}$$

The same decomposition can be applied to $\mathbf{H}(\mathbf{r},t)$, i.e.

$$\mathbf{H}(\mathbf{r},t) = \mathbf{H}_0 + \mathbf{h}(\mathbf{r},t). \tag{2.5}$$

To simplify the discussion, a Cartesian coordinate system will now be employed with $\{\mathbf{e}_x, \mathbf{e}_y, \mathbf{e}_z\}$ being the set of orthogonal unit vectors for the x-, y-, and z-axes. The externally applied field is assumed to be constant and always applied along the z-axis, i.e. $\mathbf{H}_0 = H_0\mathbf{e}_z$ with $H_0 > 0$. In the low-power limit, we can assume that the deviation of the magnetisation from equilibrium is very small, i.e. $\mathbf{M}_0 \approx M_\mathrm{s}\mathbf{e}_z$, where M_s is the saturation magnetisation of the material. By neglecting second-order terms in small signals, we arrive at a linearised equation of motion:

$$\frac{\partial \mathbf{m}(\mathbf{r},t)}{\partial t} \approx \gamma\mu_0 \left[M_\mathrm{s}\mathbf{e}_z \times \mathbf{h}(\mathbf{r},t) + \mathbf{m}(\mathbf{r},t) \times H_0\mathbf{e}_z\right]. \tag{2.6}$$

2.3 Polder susceptibility tensor

In the continuous-wave limit, it is reasonable to assume the small-signal fields to be monochromatic and their time-dependent behaviour to be proportional to $e^{-i\omega t}$, i.e. $\mathbf{m}(\mathbf{r},t) = \mathbf{m}(\mathbf{r})e^{-i\omega t}$ and $\mathbf{h}(\mathbf{r},t) = \mathbf{h}(\mathbf{r})e^{-i\omega t}$. In such a case, eq. (2.6) may be further simplified into

$$-i\omega\mathbf{m}(\mathbf{r}) = \mathbf{e_z} \times \left[-\omega_\mathrm{M}\mathbf{h}(\mathbf{r}) + \omega_0\mathbf{m}(\mathbf{r})\right] \tag{2.7}$$

where

$$\omega_\mathrm{M} = -\gamma\mu_0 M_\mathrm{s}, \tag{2.8}$$

$$\omega_0 = -\gamma\mu_0 H_0. \tag{2.9}$$

The quantity ω_0 is the *Larmor frequency*: the precessional frequency of a magnetic dipole under a magnetic field H_0 in free space. It should be noted that in a bounded medium, the field quantity H_0 in ω_0 must be replaced with the *internal* field H_{int} to account for the demagnetising field; this will be discussed further in the second part of this chapter.

Equation (2.7) can be rewritten in tensorial form:

$$\mathbf{m}(\mathbf{r}) = \overline{\boldsymbol{\chi}} \cdot \mathbf{h}(\mathbf{r}) \tag{2.10}$$

where $\overline{\boldsymbol{\chi}}$ is the *Polder susceptibility tensor* [41]. In a Cartesian basis, it is expressed as

$$(\overline{\boldsymbol{\chi}})_{x,y,z} = \begin{pmatrix} \chi_s & -i\chi_a & 0 \\ i\chi_a & \chi_s & 0 \\ 0 & 0 & 0 \end{pmatrix} \tag{2.11}$$

with

$$\chi_s = \frac{\omega_0 \omega_{\mathrm{M}}}{\omega_0^2 - \omega^2}, \tag{2.12}$$

$$\chi_a = \frac{\omega \omega_{\mathrm{M}}}{\omega_0^2 - \omega^2}. \tag{2.13}$$

A magnetic permeability tensor can be further defined which relates the magnetic flux density $\mathbf{b}$ to the magnetic field intensity $\mathbf{h}$:

$$\mathbf{b}(\mathbf{r}) = \mu_0 \left[\mathbf{h}(\mathbf{r}) + \mathbf{m}(\mathbf{r})\right], \tag{2.14}$$

$$= \mu_0 \left[\overline{\mathbf{1}} + \overline{\boldsymbol{\chi}}\right] \cdot \mathbf{h}(\mathbf{r}), \tag{2.15}$$

$$= \mu_0 \overline{\boldsymbol{\mu}} \cdot \mathbf{h}(\mathbf{r}), \tag{2.16}$$

where $\overline{\boldsymbol{\mu}} = \overline{\mathbf{1}} + \overline{\boldsymbol{\chi}}$ and $\overline{\mathbf{1}}$ is the identity tensor. It is important to note that the Polder susceptibility tensor is not diagonal. This means that either the x- or y-component of the $\mathbf{h}(\mathbf{r})$ vector can excite both the x- and y- components of the magnetisation vector $\mathbf{m}(\mathbf{r})$. Also, two of the eigenvectors of $\overline{\boldsymbol{\chi}}$ are exactly circularly polarised fields, i.e. $h_x = \mp i h_y$, and $h_z = 0$. Denoting these with appropriate $+$ and $-$ subscripts, it can be shown that

$$m_{\pm} = \chi_{\pm} h_{\pm} \tag{2.17}$$

where,

$$\chi_{\pm} = \chi_s \pm \chi_a = \frac{\omega_{\mathrm{M}}}{\omega_0 \mp \omega}. \tag{2.18}$$

Equations (2.17) implies that a right- (or left-) circularly polarised field (with its polarisation plane normal to the z-axis) will only excite a right- (or left-) circularly polarised magnetisation vector. The eigenvalue χ_+ diverges when $\omega = \omega_0 = \gamma\mu_0 H_0$ and in a ferromagnetic material, this phenomenon is called the *ferromagnetic resonance* (FMR). In reality, damping prevents true divergence at the FMR frequency and spins precess until interaction with the environment causes the energy in the magnetic system to die away completely.

2.4 Dipolar spin waves in an unbounded medium

The Polder susceptibility tensor, as detailed in the previous section, is the response of a magnetic material to a *given* field $\mathbf{h}(\mathbf{r})$. In this section, we shall incorporate this susceptibility tensor into the Maxwell equations to derive a solution for the *arising* small-signal field $\mathbf{h}(\mathbf{r})$.

The Maxwell equations [42, 43] in a magnetic material that is electrically-insulating, source-free, and has a scalar dielectric constant are:

$$\boldsymbol{\nabla} \cdot \mathbf{D}(\mathbf{r}, t) = 0, \tag{2.19}$$

$$\boldsymbol{\nabla} \cdot \mathbf{B}(\mathbf{r}, t) = 0, \tag{2.20}$$

$$\boldsymbol{\nabla} \times \mathbf{E}(\mathbf{r}, t) = -\frac{\partial \mathbf{B}(\mathbf{r}, t)}{\partial t}, \tag{2.21}$$

$$\boldsymbol{\nabla} \times \mathbf{H}(\mathbf{r}, t) = \frac{\partial \mathbf{D}(\mathbf{r}, t)}{\partial t}. \tag{2.22}$$

where $|\mathbf{E}(\mathbf{r}, t)|$ and $|\mathbf{D}(\mathbf{r}, t)|$ are the electric field intensity (V/m) and the electric flux density (C/m^2), $|\mathbf{H}(\mathbf{r}, t)|$ and $|\mathbf{B}(\mathbf{r}, \mathbf{t})|$ are the magnetic field intensity (A/m) and the magnetic flux density (T), μ_0 and ϵ_0 are respectively the magnetic vacuum permeability ($4\pi\,10^{-7}$ H/m) and electric vacuum permittivity ($\approx (10^{-9}/36\pi^2)$ F/m). The constitutive relations that relate $\mathbf{B}(\mathbf{r}, t)$, $\mathbf{H}(\mathbf{r}, t)$, $\mathbf{D}(\mathbf{r}, t)$, and $\mathbf{E}(\mathbf{r}, t)$ are:

$$\mathbf{B}(\mathbf{r}, t) = \mu_0 \left[\mathbf{H}(\mathbf{r}, t) + \mathbf{M}(\mathbf{r}, t)\right], \tag{2.23}$$

$$\mathbf{D}(\mathbf{r}, t) = \epsilon_0 \epsilon \mathbf{E}(\mathbf{r}, t). \tag{2.24}$$

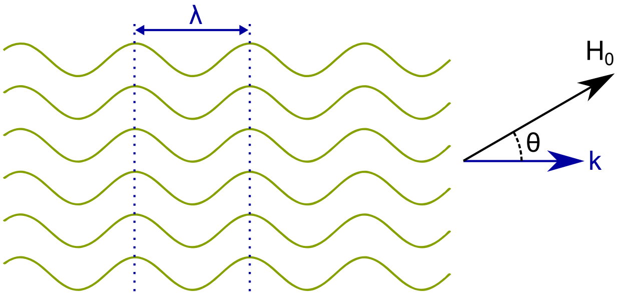

Figure 2.2: Illustration of waves of wavelength λ and wavevector $\mathbf{k}$ propagating at an angle θ with respect to the external bias field $\mathbf{H}_0$.

As discussed in the previous section, we assume the total field to be the sum of a static (steady-state) field and a small-signal one. Since the static field is constant across the material, the field quantities in eqns. (2.19-2.22) can be directly replaced by the small-signal components:

$$\boldsymbol{\nabla} \cdot \mathbf{d}(\mathbf{r}, t) = 0, \tag{2.25}$$

$$\boldsymbol{\nabla} \cdot \mathbf{b}(\mathbf{r}, t) = 0, \tag{2.26}$$

$$\boldsymbol{\nabla} \times \mathbf{e}(\mathbf{r}, t) = -\frac{\partial \mathbf{b}(\mathbf{r}, t)}{\partial t}, \tag{2.27}$$

$$\boldsymbol{\nabla} \times \mathbf{h}(\mathbf{r}, t) = \frac{\partial \mathbf{d}(\mathbf{r}, t)}{\partial t}. \tag{2.28}$$

Now, we shall consider monochromatic plane-wave solutions of the form $\mathbf{e}(\mathbf{r}, t) = \mathbf{e}\, e^{(i\mathbf{k}\cdot\mathbf{r} - i\omega t)}$ and $\mathbf{h}(\mathbf{r}, t) = \mathbf{h}\, e^{(i\mathbf{k}\cdot\mathbf{r} - i\omega t)}$. These waves are assumed to be propagating at an arbitrary angle θ with respect to the bias field $\mathbf{H}_0$ as shown in fig. 2.2. By incorporating the constitutive relations and the susceptibility tensor $\overline{\boldsymbol{\chi}}$ into the Maxwell's equations (eqns. (2.25-2.28)), we arrive at

$$\mathbf{k} \cdot \mathbf{e} = 0, \tag{2.29}$$

$$\mathbf{k} \cdot \mathbf{h} = -\mathbf{k} \cdot \overline{\boldsymbol{\chi}} \cdot \mathbf{h}, \tag{2.30}$$

$$\mathbf{k} \times \mathbf{e} = \omega \mu_0 (\overline{\mathbf{1}} + \overline{\boldsymbol{\chi}}) \cdot \mathbf{h}, \tag{2.31}$$

$$\mathbf{k} \times \mathbf{h} = -\omega \epsilon_0 \epsilon \mathbf{e}. \tag{2.32}$$

In a final trick, we perform a cross product of eq. (2.32) with the vector $\mathbf{k}$. This leads to

$$\left[\mathbf{k}\mathbf{k}^{\mathrm{T}} - k^2 \overline{\mathbf{1}} + k_0^2 \epsilon \overline{\boldsymbol{\mu}}\right] \mathbf{h} = 0 \tag{2.33}$$

where $\mathbf{k}\mathbf{k}^{\mathrm{T}}$ is an outer product between the vector $\mathbf{k}$ with itself, $k = |\mathbf{k}|$, and $k_0 = \omega\sqrt{\mu_0\epsilon_0}$ is the free-space wavevector. For a non-trivial solution $\mathbf{h}$ to exist, we require the determinant of matrix in eq. (2.33) to be zero, that is

$$\det\left[\mathbf{k}\mathbf{k}^{\mathrm{T}} - k^2\overline{\mathbf{1}} + k_0^2\epsilon\overline{\boldsymbol{\mu}}\right] = 0. \tag{2.34}$$

The solution to eq. (2.34) yields the dispersion relation of a plane wave in a magnetic material. We shall consider two limiting cases when the wave propagation is parallel ($\theta = 0$) to the bias field, i.e. $\mathbf{k} \parallel \mathbf{H}_0$, and when they are perpendicular ($\theta = \pi/2$) to each other, i.e. $\mathbf{k} \perp \mathbf{H}_0$.

We remind the reader that the bias field is always applied along the z-axis, i.e. $\mathbf{H}_0 = H_0\mathbf{e}_z$.

In the first limiting case of parallel propagation, i.e. $\theta = 0$ and $\mathbf{k} = k\mathbf{e}_z$, the non-trivial solutions to eq. (2.34) are

$$k_\pm^2 = k_0^2\epsilon(\mu_s \pm \mu_a), \tag{2.35}$$

where $\mu_s = 1 + \chi_s$ and $\mu_a = \chi_a$. If expressed in term of the frequency variables, we obtain

$$k_+^2 = k_0^2\epsilon\left(\frac{\omega_0 + \omega_{\mathrm{M}} - \omega}{\omega_0 - \omega}\right), \tag{2.36}$$

$$k_-^2 = k_0^2\epsilon\left(\frac{\omega_0 + \omega_{\mathrm{M}} + \omega}{\omega_0 + \omega}\right). \tag{2.37}$$

Equations (2.36) and (2.37) are plotted in fig. 2.3. It can be shown that both k_+ and k_- correspond respectively to right- and left- circularly polarised $\mathbf{h}$ and $\mathbf{e}$ fields [34]. Following the same line of reasoning as before, only the right-circularly polarised field (k_+ solutions) can strongly interact with the precessing magnetisation in the material.

In the second limiting case of transverse propagation, i.e. $\theta = \pi/2$ and $\mathbf{k} = k\mathbf{e}_y$, the non-trivial solutions to eq. (2.34) are:

$$k_a^2 = k_0^2\epsilon\left(\frac{\mu_s^2 - \mu_a^2}{\mu_s}\right) = k_0^2\epsilon\left(\frac{(\omega_0 + \omega_{\mathrm{M}})^2 - \omega^2}{\omega_0(\omega_0 + \omega_{\mathrm{M}}) - \omega^2}\right) \tag{2.38}$$

$$k_b^2 = k_0^2\epsilon \tag{2.39}$$

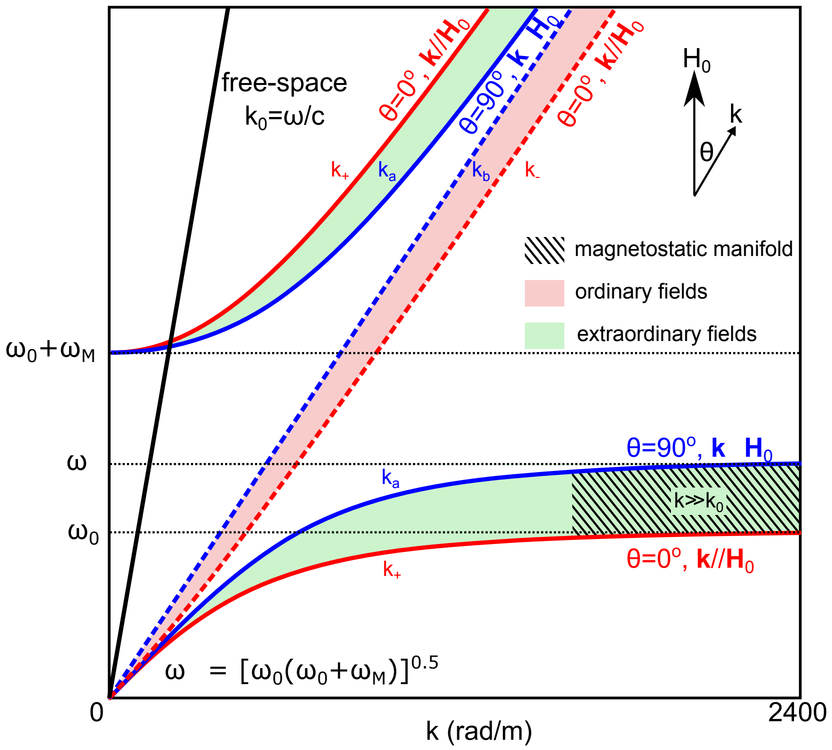

Figure 2.3: Dispersion relations of waves excited inside an electrically-insulating and isotropic magnetic material ($\epsilon = 15$, $M_\mathrm{s} = 139\,\mathrm{kA/m}$) with infinite boundary. The hatched region refers to the magnetostatic manifold where $k \gg k_0$. Inspired by fig. 3 in Ref. [44].

Equations (2.39) and (2.38) are also plotted in fig. 2.3. The k_b solution corresponds to a weakly-perturbed field that propagates through the medium almost as if it does not interact magnetically at all with the medium. Both the **h**- and **e**- fields are linearly polarised and are transverse to k_b. In contrast, the k_a solution interacts strongly with the medium. The **e**-field is linearly polarised and, interestingly, the **h**-field is *elliptically* polarised with the vector $\mathbf{k}_a$ lying parallel to the plane of the ellipse (compare this to $\theta = 0$ case where the fields are always transverse) [34].

Figure 2.3 shows that for both values of θ considered, there are the weakly-interacting solutions (k_- for $\theta = 0$, k_b for $\theta = \pi/2$). These are called the *ordinary* fields [44]. The strongly-interacting solutions (k_+ for $\theta = 0$, k_a for $\theta = \pi/2$) are the ones of interest in the context of our line of work and it is upon these – so-called *extraordinary* fields [44] – that we shall focus for the remainder of the chapter.

The extraordinary fields have two branches, as shown in fig. 2.3. Starting from very low frequencies (lower branch), the $k(\omega)$ quickly diverges with increasing ω, reaching asymptotes at $\omega = \omega_0$ for $\theta = 0$ and $\omega_\perp = \sqrt{\omega_0(\omega_0 + \omega_\mathrm{M})}$ for $\theta = \pi/2$. The asymptotes for the lower branch are usually realised in the microwave regime. There is no propagating field (a purely imaginary k) for frequencies between $\omega_0 < \omega < \omega_0 + \omega_\mathrm{M}$ for $\theta = 0$, and $\omega_\perp < \omega < \omega_0 + \omega_\mathrm{M}$ for $\theta = \pi/2$. However, as we shall see later, in a bounded sample, it is possible to excite propagating waves above the $\omega_\perp$ asymptote. The upper branch of the dispersion relation starts at $\omega_0 + \omega_\mathrm{M}$ and is usually relevant for fields of optical frequencies [34].

Henceforth, we shall focus exclusively on the asymptotic region of the lower branch. It will be shown that the asymptotic value for arbitrary propagation angle, i.e. $0 < \theta < \pi/2$, varies continuously between ω_0 and $\omega_\perp$. In this region, $k \gg k_0$ which means that the wavelength of the excitation is much smaller than the wavelength of a free-space electromagnetic field of the same frequency; the phase and group velocities ($v_\mathrm{p} = \omega/k$, $v_\mathrm{g} = d\omega/dk$) are also very much less than c.

This band of frequencies ($\omega_o \leq \omega \leq \omega_\perp$) is commonly known as the *magnetostatic region*, *magnetostatic manifold*, or *bulk band*. Due to the role that the magnetic dipolar interaction plays in shaping their dispersion, the excitations in this band are called *dipolar spin waves* or *dipolar magnons*. If a flat dispersion curve found in the magnetostatic region in fig. 2.3 were all we could access, there would not, perhaps, be reasons to get too excited about the physics of these systems. It happens though, that as soon as the boundary effects are taken into account, the magnon dispersion relation is substantially modified, giving rise to a veritable cornucopia of interesting wave properties, a few of which we shall discuss in the second part of this chapter.

2.5 Magnetostatic scalar potential

Here, we introduce the magnetostatic scalar potential that is often used as a starting point to analyse the effect of finite boundaries in the magnetostatic limit.

Firstly, we perform a cross product between $\mathbf{k}$ and eq. (2.31). By incorporating eqns. (2.30) and (2.32), we arrive at

$$\mathbf{e} = \frac{\omega\mu_0\mathbf{k} \times \mathbf{m}}{k_0^2\epsilon - k^2}. \tag{2.40}$$

In the magnetostatic limit where $k \gg k_0$, $|\mathbf{e}| \propto 1/k$ and for a very large k: $|\mathbf{e}| \approx 0$. Therefore eq. (2.28) can be simplified to

$$\boldsymbol{\nabla} \times \mathbf{h} = -i\omega\epsilon_0\epsilon\mathbf{e} \approx 0. \tag{2.41}$$

In contrast, the small-signal field $|\mathbf{h}|$ remains finite in this limit [35, 36]. The *magnetostatic approximation* generalises the condition above for any small-signal field $\mathbf{h}(\mathbf{r})$ that is slowly varying in space such that

$$\boldsymbol{\nabla} \times \mathbf{h}(\mathbf{r}) = 0. \tag{2.42}$$

This approximation allows us to express the vector $\mathbf{h}(\mathbf{r})$ in terms of the magnetostatic scalar potential $\psi(\mathbf{r})$, i.e. $\mathbf{h}(\mathbf{r}) = \boldsymbol{\nabla}\psi(\mathbf{r})$. Recall that the $\boldsymbol{\nabla} \cdot \mathbf{b}(\mathbf{r}) = 0$ and $\mathbf{b}(\mathbf{r}) = \mu_0\overline{\boldsymbol{\mu}} \cdot \mathbf{h}(\mathbf{r})$, therefore

$$\boldsymbol{\nabla} \cdot \mathbf{b}(\mathbf{r}) = 0, \tag{2.43}$$

$$\boldsymbol{\nabla} \cdot (\overline{\boldsymbol{\mu}} \cdot \boldsymbol{\nabla}\psi(\mathbf{r})) = 0, \tag{2.44}$$

$$(1+\chi_s)\left[\frac{\partial^2\psi}{\partial x^2} + \frac{\partial^2\psi}{\partial y^2}\right] + \frac{\partial^2\psi}{\partial z^2} = 0. \tag{2.45}$$

Equation (2.45) is called the *Walker* equation [37]. In free space $\chi_s = 0$, and the Walker equation therefore reduces to the Laplace equation

$$\nabla^2\psi(\mathbf{r}) = 0, \tag{2.46}$$

$$\left[\frac{\partial^2\psi}{\partial x^2} + \frac{\partial^2\psi}{\partial y^2} + \frac{\partial^2\psi}{\partial z^2}\right] = 0. \tag{2.47}$$

As promised earlier, we now derive the asymptotic values of ω in fig. 2.3 for arbitrary angle θ, i.e. $0 < \theta < \pi/2$, with the aid of the Walker equation. Under the assumption of an infinite boundary, it is reasonable to model the scalar potential as a plane wave $\psi \propto e^{(i\mathbf{k}\cdot\mathbf{r})}$. Recalling that $k^2 = k_x^2 + k_y^2 + k_z^2$ and denoting $\tan\theta = k_z/(\sqrt{k_x^2 + k_y^2})$, we obtain

$$(1+\chi_s)(k_x^2 + k_y^2) + k_z^2 = 0, \tag{2.48}$$

$$\chi_s \sin^2\theta = -1, \tag{2.49}$$

$$\omega_\theta = \sqrt{\omega_0(\omega_0 + \omega_{\mathrm{M}}\sin^2\theta)}. \tag{2.50}$$

In the limit of $\theta = 0$ and $\theta = \pi/2$, ω_θ in eq. (2.50) reduces to ω_0 and $\omega_\perp$ respectively, in agreement with the results derived above.

2.6 Dipolar spin waves in confined geometries

2.6.1 Introduction

Previously, we derived the dispersion relation of excitations in an unbounded magnetic material (see fig. 2.3). We demonstrated the existence of a magnetostatic manifold characterised by $k \gg k_0$. Now we shall extend our treatment to include the effect of finite boundaries. In samples of finite size, the dispersion relation is modified, and a wide range of travelling and standing-wave modes are possible. We shall focus particularly on two geometries: spheres and films.

Commercially, the yttrium iron garnet (YIG) spheres are available in sizes ranging from $\sim 0.2\,\mathrm{mm}$ to $\sim 1\,\mathrm{mm}$. Gigahertz-frequency standing-wave modes – precisely the frequency range that is of interest to us – can be observed in such spheres. Broadly speaking, their spin-wave spectrum can be divided into three regions [37, 45]. For low-k wave excitations whose wavelength is much larger than the size of the sphere, the boundary effect gives rise to discrete standing-wave modes. As k increases such that the wavelength becomes comparable or smaller than the sphere's size, a continuum of propagating dipolar spin waves can begin to be accessed. Finally, when the magnon wavelength becomes comparable to the exchange length, exchange excitations dominates the response.

YIG films — designed for dipolar-wave experiments — are commonly grown with µm-thickness and a much larger lateral size (a few mms). Most theoretical treatments only consider the confinement effect along one axis and approximate films to be infinite in size along the other two. Spin waves excited in such films can only propagate in the plane of the film. It is common therefore to refer to such films as *waveguides*. However, as in the case of spheres, as soon as the lateral size of the film becomes comparable to λ, it is then possible to excite discrete standing-wave modes along the lateral dimension. Standing-wave modes across the thickness also exist, but these are usually in the exchange regime and at a much higher frequencies than those at which we conduct our experiments.

Geometry	**Field configuration**	N_x	N_y	N_z
Film (normal to the y-axis)	In-plane	0	1	0
Film (normal to the z-axis)	Out-of-plane	0	0	1
Sphere		1/3	1/3	1/3

Table 2.1: Diagonal elements of the demagnetising tensor for the film and spherical geometries. We define the z-axis to be always parallel to the bias field direction.

The internal magnetic field found in a magnetic sample of finite extent is reduced due to the presence of a geometrical *demagnetising* field according to $\mathbf{H}_\mathrm{d} = \overline{\boldsymbol{N}}_\mathrm{d} \cdot \mathbf{M}$ where $\overline{\boldsymbol{N}}_\mathrm{d}$ is the demagnetising tensor such that the *internal* magnetic field is:

$$\mathbf{H}_\mathrm{int} = \mathbf{H}_0 - \overline{\boldsymbol{N}}_\mathrm{d} \cdot \mathbf{M}. \tag{2.51}$$

The demagnetising tensor is, in general, non-uniform and depends on the shape of the material. Only in certain geometries and field configurations can the tensor be expressed in a diagonal form. Helpfully for us, spheres and films are counted along those in which such a simplification is possible. Table 2.1 lists $\{N_x,\, N_y,\, N_z\}$, the diagonal elements (and the only non-zero elements) of the relevant demagnetising tensors. The internal field for a uniformly magnetised sphere is $H_0 - \frac{1}{3}M_\mathrm{s}$ and for an out-of-plane magnetised film is $H_0 - M_\mathrm{s}$. In the case of an in-plane magnetised film, the internal field is equal to the applied field H_0.

It is crucially important to note that when the demagnetising field is non-zero, it is the internal field H_int that is used (instead of simply H_0) to calculate the frequency quantity ω_0 that figures into the quantities χ_s (eq. (2.12)) and χ_a (eq. (2.13)) of the Polder susceptibility tensor.

2.6.2 Spherical geometry

Now we consider the discrete standing-wave modes that can be excited in a sphere of magnetic material. In the microwave-frequency band of interest to us experimentally and for typical sphere sizes that are available commercially, it is usually these standing-wave modes that are excited.

The problem of standing modes in magnetic spheroids was first discussed by Walker [45]. Later on, Fletcher and Bell [46] simplified the derivation for the case

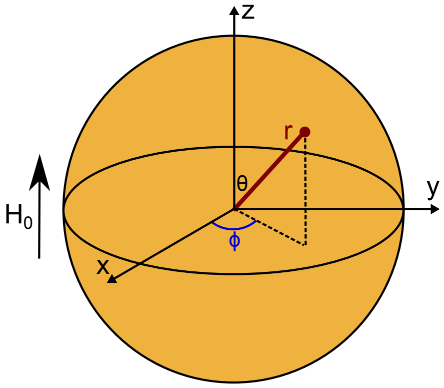

Figure 2.4: Illustration of a sphere magnetised along the z-axis by an applied field H_0.

of a sphere and provided analytical expressions for several modes. In the following, we provide an overview of the derivation based on treatment of Fletcher and Bell.

The approach we adopt is to first model the scalar potentials (Section 2.5) inside and outside the sphere (ψ_{in}, ψ_{out}). The appropriate boundary conditions at the surface of the sphere are applied to solve for the arbitrary constants within ψ_{in} and ψ_{out}. Then, the magnetisation profile and the resonance condition can be calculated.

Outside the sphere, the Walker equation reduces to the Laplace equation eq. (2.47). The appropriate coordinate system to use in this case is a spherical one $\{\mathbf{e}_r,\ \mathbf{e}_\theta,\ \mathbf{e}_\phi\}$ (fig. 2.4):

$$x = r\sin\theta\cos\phi, \tag{2.52}$$

$$y = r\sin\theta\sin\phi, \tag{2.53}$$

$$z = r\cos\theta. \tag{2.54}$$

The general solution to the Laplace equation in spherical coordinates is:

$$\begin{aligned}\psi_{\text{out}} = \sum_{n=1}^{\infty}\sum_{m=-n}^{n} & r^n P_n^m(\cos\theta)\left[A_n^m\cos(m\phi) + iB_n^m\sin(m\phi)\right] \\ & + \frac{1}{r^{n+1}}P_n^m(\cos\theta)\left[D_n^m\cos(m\phi) + iF_n^m\sin(m\phi)\right]\end{aligned} \tag{2.55}$$

where P_n^m are the associated Legendre functions. The indices n and m are used to denote the various solutions where $n \in \mathbb{N}^*$ and $m = -n, -n+1, ..., 0, ..., n$. The constants A_n^m and B_n^m describe the applied microwave field and are assumed to be defined in the problem. D_n^m and F_n^m are arbitrary constants that are to be determined.

Inside the sphere, the Walker equation cannot be easily solved in spherical coordinates and has to be transformed into prolate spheroidal coordinates $\{\mathbf{e}_\xi, \mathbf{e}_\eta, \mathbf{e}_\phi\}$ where

$$x = a(-\chi_s)^{1/2}(1-\xi^2)^{1/2}\sin\eta\cos\phi, \tag{2.56}$$

$$y = a(-\chi_s)^{1/2}(1-\xi^2)^{1/2}\sin\eta\sin\phi, \tag{2.57}$$

$$z = a\left(\frac{\chi_s}{1+\chi_s}\right)^{1/2}\xi\cos\eta. \tag{2.58}$$

Here, a is the radius of the sphere. The solution to the Walker equation in the transformed coordinates can be expressed as

$$\psi_{\text{in}} = P_n^m(\xi)P_n^m(\cos\theta)\left[G_n^m\cos(m\phi) + iH_n^m\sin(m\phi)\right], \tag{2.59}$$

where G_n^m and H_n^m are the arbitrary constants that are to be determined.

Applying the boundary condition at the surface of the sphere (continuity of both the tangential component of $\mathbf{h}$ and the normal component of $\mathbf{b}$), the four arbitrary constants in the equations above (D_n^m, F_n^m, G_n^m, H_n^m) can be determined. In this way, the resonance condition, the scalar potential ψ, and consequently m_x and m_y for the various modes can be calculated explicitly. The explicit expressions for several combinations of n and m have been conveniently compiled in [46].

The position dependence of m_x, m_y, and the resonant condition for the $(n, m=n)$ modes are as follows

$$m_x = A_{(n,n)}(x+iy)^{n-1}, \tag{2.60}$$

$$m_y = iA_{(n,n)}(x+iy)^{n-1}, \tag{2.61}$$

$$A_{(n,n)} = \left(\frac{2n!}{2^n n!}\right)^2\left(\frac{1}{a(-\chi_s)^{1/2}}\right)^n(\chi_s+\chi_a)n, \tag{2.62}$$

$$\omega_{(n,n)} = \omega_0 + \frac{n}{2n+1}\omega_{\mathrm{M}}. \tag{2.63}$$

For the $(n, m = n-1)$ modes, they become

$$m_x = B_{(n,n-1)}(x+iy)^{n-2}\frac{z}{a}, \tag{2.64}$$

$$m_y = iB_{(n,n-1)}(x+iy)^{n-2}\frac{z}{a}, \tag{2.65}$$

$$B_{(n,n-1)} = A_{(n,n)}\left(\frac{n-1}{n}\right)\left(\frac{1+\chi_s}{\chi_s}\right)^{1/2}, \tag{2.66}$$

$$\omega_{(n,n-1)} = \omega_0 + \frac{n-1}{2n+1}\omega_{\mathrm{M}}. \tag{2.67}$$

It is instructive to notice that the magnetisation vector for (n, n) and $(n, n-1)$ is circularly polarised with respect to the z-axis. The $(1, 1)$ mode is known as the Kittel mode [47] in which the magnetisation precesses uniformly in phase across the sphere. The resonance frequency of the Kittel mode is independent of the saturation magnetisation:

$$\omega_{(1,1)} = \omega_0 + \frac{1}{3}\omega_{\mathrm{M}}, \tag{2.68}$$

$$= -\mu_0\gamma(H_0 - \frac{1}{3}M_s) - \mu_0\gamma\frac{1}{3}M_s, \tag{2.69}$$

$$= -\mu_0\gamma H_0. \tag{2.70}$$

For $n \geq 2$, the small-signal magnetisation amplitude $(\sqrt{m_x^2 + m_y^2})$ for the (n, n) modes is highest at the sphere's surface. Unlike the (n, n) modes, the $(n, n-1)$ modes have magnetisation amplitudes that are z-dependent. In general, the higher $|n - m|$, the more complicated the magnetisation profile. This continues to the point where the excitation wavelength is comparable to the size of the sphere, when propagating modes start to be excited. Figure 2.5 shows some examples of the magnetisation patterns corresponding to the (n, n) and $(n, n-1)$ modes.

2.6.3 Film: out-of-plane magnetisation

We now consider magnetisation dynamics in a magnetic film that is magnetised out of plane in free space. In a derivation that follows Refs. [48] and [35], our strategy will be similar to that employed in the case of spheres. We first specify the scalar potentials both inside and outside the film. Then, by applying the appropriate boundary conditions on both surfaces of the film, we determine the magnetisation

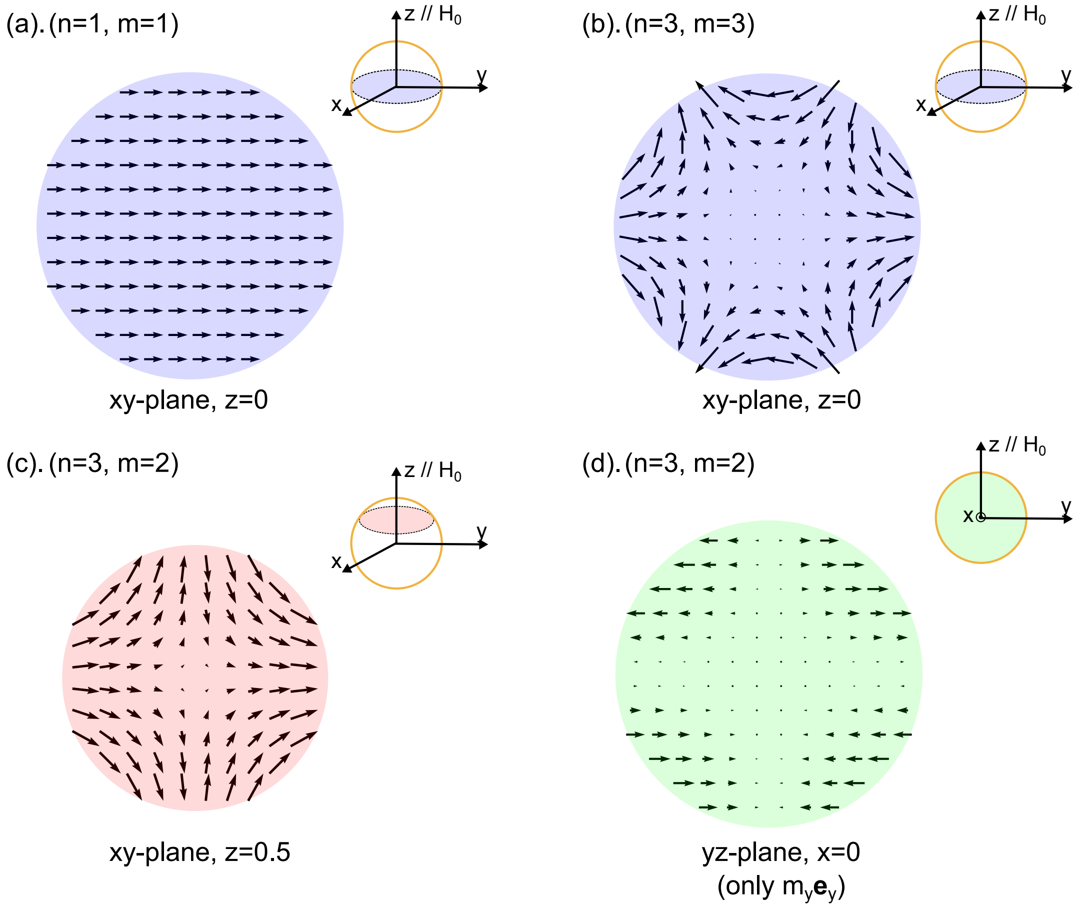

Figure 2.5: Snapshots of various magnetisation modes that can be excited in a magnetic sphere (radius is 1). The arrows denote the vector $\mathbf{m}(\mathbf{r})$ (with the exception of panel (d) that only plots the y-component of the small-signal magnetisation vector). The bias field is oriented along the z-axis. The arrow lengths within each panel have been properly normalised to ensure visibility, as such it is not possible to compare mode amplitudes across the different panels shown above.

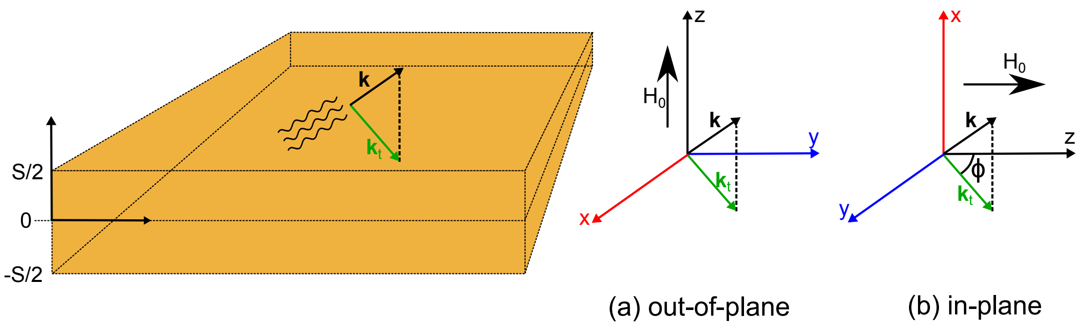

Figure 2.6: Illustration of a film (thickness S) magnetised along its normal axis (panel (a)) and parallel to the film's plane (panel (b)). Notice that the z-axis in panel (a) is oriented differently than in panel (b).

profile and the spin-wave dispersion relation. We remind the reader that the bias field is oriented along the z-axis and that the film is assumed to be infinite in extent on the xy-plane. The demagnetising field in this case is $\mathbf{H}_\mathrm{d} = -M_\mathrm{s}\mathbf{e}_z$ with $\mathbf{H}_0 = H_0\mathbf{e}_z$ (Table 2.1), therefore $\mathbf{H}_\mathrm{int} = (H_0 - M_\mathrm{s})\mathbf{e}_z$ and $\omega_0 = -\gamma\mu_0(H_0 - M_\mathrm{s})$.

Figure 2.6(a) illustrates a film of thickness S with its surface normal to the z-axis. Consider a plane wave inside the film ($|z| \le S/2$) with an arbitrary wavevector $\mathbf{k}$ that can be decomposed into a component tangential to the plane of the film ($\mathbf{k}_\mathrm{t}$) and a component normal to it ($k_z\mathbf{e}_z$), i.e. $\mathbf{k} = \mathbf{k}_\mathrm{t} + k_z\mathbf{e}_z$. Every reflection from an interface (the upper or lower boundaries of the film) flips the sign of $k_z\mathbf{e}_z$. After multiple reflections, the waves can be considered to be propagating parallel to the plane of the film while forming a standing wave along the z-axis. The scalar potential inside the film can be modelled as:

$$\psi_\mathrm{II} = \left[A\sin(k_z z) + B\cos(k_z z)\right] e^{i\mathbf{k}_\mathrm{t}\cdot\mathbf{r}_\mathrm{t}} \qquad \text{for } |z| \le S/2 \tag{2.71}$$

where $\mathbf{r}_\mathrm{t} = (x\mathbf{e}_x + y\mathbf{e}_y)$ and the constants (A and B) are determined from the boundary conditions.

Outside the film ($|z| > S/2$), the wave can be modelled as a plane wave with wavevector $\mathbf{k}_\mathrm{e}$. The scalar potential outside the film must satisfy the Laplace equation ($\nabla^2\psi_\mathrm{e} = 0$), therefore

$$k_{\mathrm{e},x}^2 + k_{\mathrm{e},y}^2 + k_{\mathrm{e},z}^2 = 0 \tag{2.72}$$

$$k_{\mathrm{e},z}^2 = -k_{\mathrm{e,t}}^2 \tag{2.73}$$

$$k_{\mathrm{e},z} = \pm i k_{\mathrm{e,t}} \tag{2.74}$$

This also allows us to express the scalar potentials outside the film as:

$$\psi_\mathrm{I} = Ce^{i\mathbf{k}_\mathrm{e}\cdot\mathbf{r}} = Ce^{i\mathbf{k}_\mathrm{e,t}\cdot\mathbf{r}_\mathrm{t}}e^{-k_\mathrm{e,t}z} \qquad \text{for } z \ge S/2 \tag{2.75}$$

$$\psi_\mathrm{III} = De^{i\mathbf{k}_\mathrm{e}\cdot\mathbf{r}} = De^{i\mathbf{k}_\mathrm{e,t}\cdot\mathbf{r}_\mathrm{t}}e^{+k_\mathrm{e,t}z} \qquad \text{for } z \le -S/2 \tag{2.76}$$

By applying the boundary conditions at both surfaces of the film (continuity of both the tangential component of $\mathbf{h}$ and the normal component of $\mathbf{b}$), we can show that

$$\mathbf{k}_\mathrm{e,t} = \mathbf{k}_\mathrm{t} \tag{2.77}$$

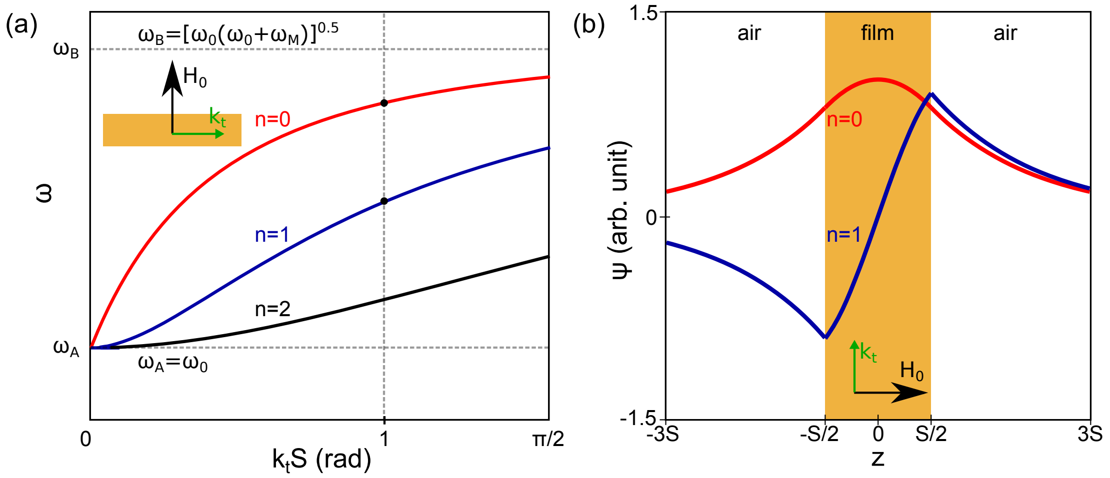

Figure 2.7: (a) Dispersion relation of forward volume waves for the lowest three thickness modes plotted for $\omega_0 = \omega_{\mathrm{M}}$. (b) The corresponding mode profile for the two lowest thickness modes plotted for $k_{\mathrm{t}}S = 1$.

and

$$\tan\left(\frac{k_z S}{2} - \frac{n\pi}{2}\right) = \frac{k_{\mathrm{t}}}{k_z} \tag{2.78}$$

where $n \in \mathbb{N}$ is indexes the different thickness modes.

Equation (2.77) tells us that the tangential components of the wavevectors inside the film ($\mathbf{k}_{\mathrm{t}}$) and outside the film $\mathbf{k}_{e,\mathrm{t}}$ are the same. We are interested in propagating-wave solutions inside the film and therefore real values of k_{t}. As a result, $k_{\mathrm{e,z}}$ is constrained to be an imaginary number (eqns. (2.77) and (2.74)), and waves outside the film quickly decay away from the surface. The higher the propagation wavenumber k_{t}, the shorter the characteristic decay length ($1/k_{\mathrm{t}}$) outside of the film.

It can be shown from eq. (2.49) (or the Walker equation) that in the case of an out-of-plane magnetised film:

$$\frac{k_{\mathrm{t}}}{k_z} = \frac{\sqrt{k_x^2 + k_y^2}}{k_z} = \frac{1}{\sqrt{-(1+\chi_{\mathrm{s}})}} = \sqrt{\frac{\omega^2 - \omega_0^2}{\omega_0(\omega_0 + \omega_{\mathrm{M}}) - \omega^2}}. \tag{2.79}$$

Equations (2.78) and (2.79) may be combined to yield the dispersion relation of dipolar spin-waves in an out-of-plane magnetised film (ω vs k_{t})

$$\tan\left(\sqrt{-(1+\chi_s)}\frac{k_{\mathrm{t}}S}{2} - \frac{n\pi}{2}\right) = \frac{1}{\sqrt{-(1+\chi_s)}}. \tag{2.80}$$

The dispersion relations corresponding to several thickness modes are plotted in fig. 2.7(a). Even values of n (including $n = 0$) correspond to potential profiles that are symmetric across the film's thickness ($A = 0, B \neq 0, C = D$); odd values of n to antisymmetric profiles ($A \neq 0, B = 0, C = -D$). Figure 2.7(b) shows both the lowest symmetric and antisymmetric mode profiles.

Spin waves of this type, i.e. propagating in an out-of-plane magnetised films, are referred to as *forward volume* magnetostatic spin waves (FVMSW) . The term "forward" originates from the fact that the phase and group velocities of the waves have the same sign [35]. We shall see that the opposite is true for so-called backward waves (Section 2.6.4). "Volume" is a reference to the fact that the magnetisation amplitude of the waves is distributed across the thickness (i.e. throughout the volume), and distinguishes the waves from surface waves which we shall meet in the Section 2.6.4. The dispersion relation of forward volume waves does not depend on the orientation of $\mathbf{k}_\mathrm{t}$ with respect to the x- and y- axes, i.e. it is isotropic in the xy-plane. As we shall see in the next section, this isotropicity in the dispersion relation is broken by an in-plane bias field.

The frequency range of the forward volume waves coincides with the magnetostatic manifold:

$$\omega(k_\mathrm{t} = 0) \leq \omega_\mathrm{forward} \leq \omega(k_\mathrm{t} \to \infty), \tag{2.81}$$

$$\omega_0 \leq \omega_\mathrm{forward} \leq \omega_\perp. \tag{2.82}$$

The uniform precession mode ($k_\mathrm{t} = 0$) corresponds to the waves only bouncing back and forth between the film's surfaces ($k = k_z \parallel H_0$). This is the bottom branch of the manifold ($\omega(k_\mathrm{t} = 0) = \omega_0$) in fig. 2.3. Conversely, in the limit $k_\mathrm{t} \to \infty$, the waves are propagating almost perpendicular to the bias field ($k \approx k_\mathrm{t} \perp H_0$). This corresponds to the upper branch of the manifold ($\omega(k_\mathrm{t} \to \infty) = \sqrt{\omega_0(\omega_0 + \omega_\mathrm{M})}$) in fig. 2.3.

2.6.4 Film: in-plane magnetisation

We now consider a magnetic film that is magnetised in-plane in free space. The derivation that follows draws on Refs. [35], [36], and [49]. We continue to orient the bias magnetic field parallel to the z-axis (fig. 2.6(b)). The normal to the surface of the film is oriented along the x-axis and the film is assumed to be infinite in extent in the yz-plane. The demagnetising field is zero in this case and therefore $H_{\mathrm{int}} = H_0$ and $\omega_0 = -\gamma\mu_0 H_0$.

As in the out-of-plane case, the waves are assumed to propagate with arbitrary direction within the film. After multiple reflections from both film surfaces, the waves can be considered to be propagating tangential to the plane of the film (parallel to the yz-plane) while forming a standing wave along its thickness (x-axis).

We shall denote the wavevector outside the film $\mathbf{k}_{\mathrm{e}} = \mathbf{k}_{\mathrm{e,t}} + ik_{\mathrm{e},x}\mathbf{e}_x$, where $\mathbf{k}_{\mathrm{e,t}}$ is the component tangential to the film's plane. Here, we take the liberty of directly defining an imaginary value for the x-component (or the component normal to the plane of the film) of $\mathbf{k}_{\mathrm{e}}$ to ensure that the scalar potential vanishes at distances far away from the film ($|x| \gg S$). This step simplifies the treatment below and can be justified in a manner similar to that presented for the out-of-plane case. The wavevector inside the film can be written as $\mathbf{k} = \mathbf{k}_{\mathrm{t}} + k_x\mathbf{e}_x$. In the first instance, we place no constraint on the value of k_x (i.e. it can be either purely real, or purely imaginary, or complex). This is a point we shall return to at the end of this section.

The scalar potentials inside and outside the film are:

$$\psi_{\mathrm{I}} = Ce^{-k_{\mathrm{e},x}x}T_{\mathrm{e}}(y,z) \qquad \text{for } x > S/2, \tag{2.83}$$

$$\psi_{\mathrm{II}} = [A\sin(k_x x) + B\cos(k_x x)]\,T_{\mathrm{i}}(y,z) \qquad \text{for } |x| \le S/2, \tag{2.84}$$

$$\psi_{\mathrm{III}} = De^{k_{\mathrm{e},x}x}T_{\mathrm{e}}(y,z) \qquad \text{for } x < -S/2, \tag{2.85}$$

$$T_{\mathrm{e}}(y,z) = e^{i\mathbf{k}_{\mathrm{e,t}}\cdot(y\mathbf{e}_y + z\mathbf{e}_z)}, \tag{2.86}$$

$$T_{\mathrm{i}}(y,z) = e^{i\mathbf{k}_{\mathrm{t}}\cdot(y\mathbf{e}_y + z\mathbf{e}_z)}. \tag{2.87}$$

By imposing the boundary conditions on both surfaces of the film (continuity of both the tangential component of $\mathbf{h}$ and the normal component of $\mathbf{b}$), it can be shown that

$$\mathbf{k}_{\mathrm{e,t}} = \mathbf{k}_{\mathrm{t}} \tag{2.88}$$

and

$$k_{\mathrm{e},x}^2 - k_x^2(1+\chi_{\mathrm{s}})^2 - \chi_{\mathrm{a}}^2 k_{\mathrm{t}}^2 \sin^2\phi + 2k_x k_{\mathrm{e},x}(1+\chi_{\mathrm{s}})\cot(k_x S) = 0 \tag{2.89}$$

where $\tan\phi = k_y/k_z$.

Equation (2.88) implies that the components of $\mathbf{k}$ and $\mathbf{k}_\mathrm{e}$ tangential to the film's plane are equal, as in the out-of-plane case (eq. (2.77)). Applying the Laplace equation to the scalar potentials outside the film and taking into account eq. (2.88), we obtain:

$$k_\mathrm{t}^2 = k_{\mathrm{e},x}^2 \tag{2.90}$$

i.e. the characteristic decay length of the wave outside the film is k_t. This means that the decay length decreases with increasing propagation wavevector k_t. Applying the Walker equation (eq. (2.45)) inside the film yields

$$\begin{aligned} k_x &= \pm k_\mathrm{t}\sqrt{-\frac{1+\chi_\mathrm{s}\sin^2\phi}{1+\chi_\mathrm{s}}}, && (2.91) \\ &= \pm k_\mathrm{t}\sqrt{\frac{\omega^2-\omega_0(\omega_0+\omega_\mathrm{M}\sin^2\phi)}{\omega_0(\omega_0+\omega_\mathrm{M})-\omega^2}}. && (2.92) \end{aligned}$$

Equations (2.89-2.91), in combination, allow us to find the dispersion relation of dipolar spin-waves propagating at an angle ϕ with respect to the bias field or the z-axis (see fig. 2.6(b)). Notice that in contrast to the out-of-plane case (eq. (2.80)), the dispersion relation now depends on the angle ϕ, i.e. it is not isotropic in the plane of the film (yz-plane). This is because the in-plane bias field breaks the symmetry.

As shown by Hurben and Patton [36], the excited waves in the case of in-plane bias field can generally be classified into so-called *backward volume* magnetostatic spin waves (BVMSW) and the magnetostatic *surface* spin waves (MSSW). Backward volume waves are solutions to eq. (2.91) in which k_x have real values. Their magnetisation profile is distributed across the film's thickness, have multiple standing-wave modes across the thickness, and its frequency range coincide with the magnetostatic manifold in fig. 2.3. The frequency range of backward volume waves generally decreases with increasing ϕ, disappearing completely at $\phi = \pi/2$. Surface waves correspond to k_x in eq. (2.91) having imaginary values, unlike forward and backward waves. They do not possess multiple thickness modes and are nonreciprocal with respect to the propagation direction. As the name suggests,

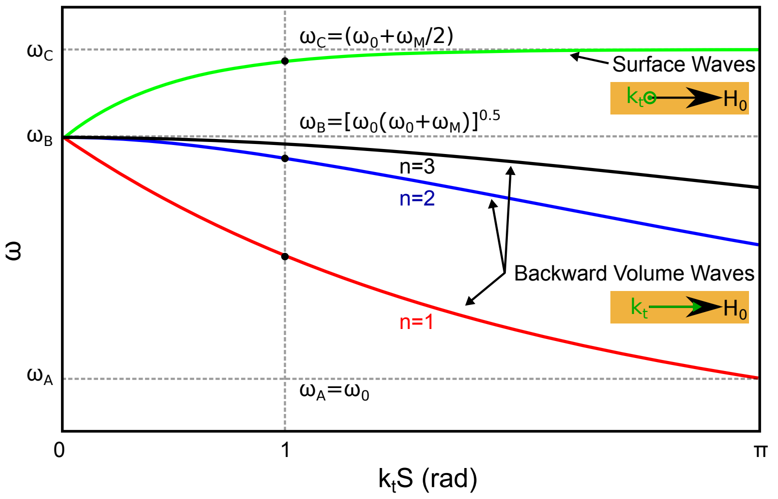

Figure 2.8: Dispersion relations of backward volume waves ($k_\mathrm{t} \parallel H_0$) and surface waves ($k_\mathrm{t} \perp H_0$) plotted for $\omega_0 = \omega_\mathrm{M}$. Note that in contrast to backward volume waves, surface waves are located outside of the magnetostatic region derived for a material with infinite boundary.

surface wave mode profiles are localised on the film's surface, and they lie outside of the magnetostatic manifold. The frequency range of surface waves is the highest at $\phi = \pi/2$, decreases with decreasing ϕ, and disappears for angles below the critical angle $\tan\phi_\mathrm{c} = \omega_0/\omega_\mathrm{M}$ [36].

We shall focus solely on the two limiting cases of parallel propagation ($\phi = 0$) and transverse propagation ($\phi = \pi/2$).

Parallel propagation: backward volume waves

In the case of parallel propagation ($\phi = 0$), only the *backward volume* magnetostatic spin waves (BVMSW) can be excited. As alluded to previously, the term “backward” references the fact that the phase and group velocities are in opposite directions [35]. The dispersion relation can be expressed as follows (eq. (2.89) for $\phi = 0$):

$$\tan\left(\frac{1}{\sqrt{-(1+\chi_\mathrm{s})}}\frac{k_\mathrm{t}S}{2} - \frac{(n-1)\pi}{2}\right) = \sqrt{-(1+\chi_\mathrm{s})} \tag{2.93}$$

where

$$\frac{k_\mathrm{t}}{k_x} = \sqrt{-(1+\chi_\mathrm{s})} = \sqrt{\frac{\omega_0(\omega_0+\omega_\mathrm{M}) - \omega^2}{\omega^2 - \omega_0^2}} \tag{2.94}$$

and $n \in \mathbb{N}^*$.

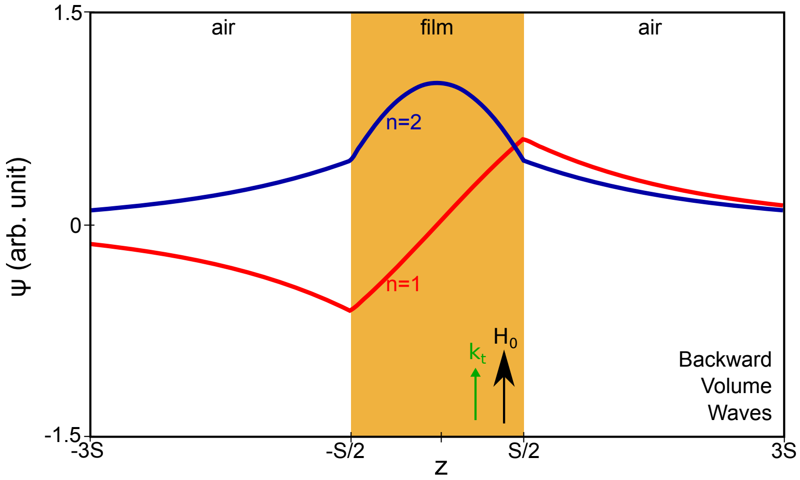

Figure 2.9: Mode profile of the two lowest order thickness modes of backward volume waves plotted for $k_tS = 1$ and $\omega_0 = \omega_M$.

Figure 2.8 shows the dispersion relation for the three lowest BVMSW thickness modes. Even values of n correspond to symmetric mode profiles across the film thickness ($A = 0, B \neq 0, C = D$). Odd values of n correspond to antisymmetric mode profiles ($A \neq 0, B = 0, C = -D$). In contrast to FVMSW, the lowest order BVMSW mode is $n = 1$ and therefore has an antisymmetric profile (fig. 2.9). Like FVMSW, BVMSW occupy the magnetostatic manifold:

$$\omega(k_t = 0) \geq \omega_{\text{backward}} \geq \omega(k_t \to \infty), \tag{2.95}$$

$$\omega_\perp \geq \omega_{\text{backward}} \geq \omega_0. \tag{2.96}$$

In the uniform precession mode ($k_t = 0$), the waves simply bounce back and forth between the film's surfaces ($k = k_z \perp H_0$). This corresponds to the upper branch of the magnetostatic band in fig. 2.3 ($\omega(k_t = 0) = \omega_\perp = \sqrt{\omega_0(\omega_0 + \omega_M)}$) in fig. 2.3. Conversely, in the limit $k_t \to \infty$, the waves propagate parallel to the bias field ($k \approx k_t \parallel H_0$) and occupy the lowest branch ($\omega = \omega_0$).

Transverse propagation: surface waves

In the case of transverse propagation ($\phi = \pi/2$), a peculiar type of spin waves called magnetostatic *surface* spin waves (MSSW) are excited. Unlike FVMSW and BVMSW, the mode profile of MSSW is always localised on the surface of the film.

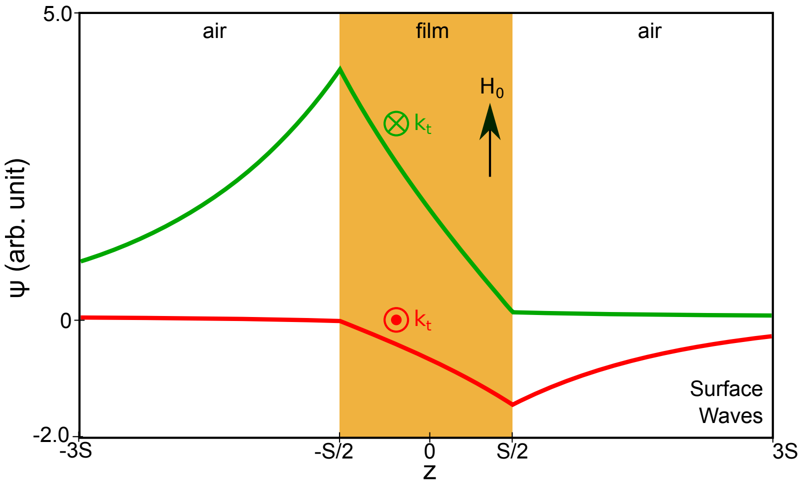

Figure 2.10: Mode profile of surface waves plotted for $\omega_0 = \omega_\mathrm{M}$ and $k_\mathrm{t}S = 1$. The surface wave propagation is non-reciprocal with the scalar potential being higher for one propagation direction. If the field direction is reversed, the other propagation direction becomes the dominant one.

The Walker equation for an in-plane magnetised film (eq. (2.91)) in the case of transverse propagation is

$$k_x = \pm i k_\mathrm{t}. \tag{2.97}$$

In order to have a propagating-wave solution, the tangential wavevector inside the film (k_t) has to be real-valued. This implies that the x-component of the wavevector inside the film (k_x) has to be an imaginary number (eq. (2.97)). As a result, the mode profile is localised at the film's surface.

Assuming that the waves propagate in the positive y- direction, i.e. $k_x = +ik_\mathrm{t}$. Equations (2.89) and (2.90) can be combined to produce:

$$\coth(k_\mathrm{t}S) = \frac{1 + (1+\chi_\mathrm{s})^2 - \chi_\mathrm{a}^2}{-2(1+\chi_\mathrm{s})} \tag{2.98}$$

$$k_\mathrm{t}S = -\frac{1}{2}\ln\left[1 + \frac{4}{\omega_\mathrm{M}^2}\left[\omega_0(\omega_0+\omega_\mathrm{M}) - \omega^2\right]\right]. \tag{2.99}$$

Equation (2.99) is the dispersion relation of MSSW. Note that the frequency range of MSSW is above the magnetostatic manifold, i.e.

$$\omega(k_\mathrm{t} = 0) \leq \omega_\mathrm{surface} \leq \omega(k_\mathrm{t} \to \infty), \tag{2.100}$$

$$\omega_\perp \leq \omega_\mathrm{surface} \leq \omega_0 + \omega_\mathrm{M}/2. \tag{2.101}$$

This is made possible by allowing an imaginary value of k_x in the Walker equation. The uniform precession mode ($k_\mathrm{t} = 0$) corresponds to the upper branch of the magnetostatic manifold ($\omega(k_\mathrm{t} = 0) = \omega_\perp = \sqrt{\omega_0(\omega_0 + \omega_\mathrm{M})}$) in fig. 2.3. The uniform precession mode of surface waves and backward volume waves thus coincide in frequency. The limit of $k_\mathrm{t} \to \infty$ corresponds to $\omega(k_\mathrm{t} \to \infty) = \omega_0 + \omega_\mathrm{M}/2$, which is outside the magnetostatic manifold in fig. 2.3 (fig. 2.8).

Surface waves have a number of interesting properties. First of all, the presence of the hyperbolic cotangent function in eq. (2.98) means that for a given film there is just one mode; this is in stark contrast with the multiple thickness modes obtained for both forward and backward volume waves. Secondly, the mode is localised at the surface of the film from which its magnetisation amplitude dies away exponentially (both inside and outside the film) with a characteristic decay length of $1/k_\mathrm{t}$. The higher the wavenumber k_t, the stronger the localisation. Thirdly, surface waves are nonreciprocal with respect to the propagation direction, a point illustrated in fig. 2.10 [36, 49]: for a given bias field, the mode is more localised on one surface of the film and if the bias field direction is reversed, the mode moves to the opposite surface. This non-reciprocity is unique to surface waves.

3

Experimental Setup and Materials

This chapter introduces our experimental setup and the magnetic material used in our experiments.

3.1 Experimental setup

At the core of our low-temperature system is a dilution fridge (fig. 3.1). The cooling function of the fridge is achieved via two main components: a pulse tube cooler (PTC) and a dilution unit. During operation, the inner part of the fridge is kept under vacuum in order to minimise heat exchange with the external environment. The PTC maintains two intermediate temperature stages (PT1 and PT2) at $\sim 60\,\mathrm{K}$ and $\sim 4\,\mathrm{K}$ respectively. The lower temperature plates are first cooled down by thermal contact with the PT2 stage. After reaching temperatures of a few Kelvin, the thermal contact is substantially reduced and the dilution unit begins to further cool them by evaporating ^{3}He from a concentrated phase to a more dilute phase in a ^{3}He-^{4}He mixture. This process in endothermic and allows sufficient heat to be removed such that temperatures of 15 mK-20 mK can be achieved at the mixing chamber stage where the sample is located [50]. In principle, the temperature at the mixing chamber stage can be controlled up to 30 K through the use of integrated resistive heaters.

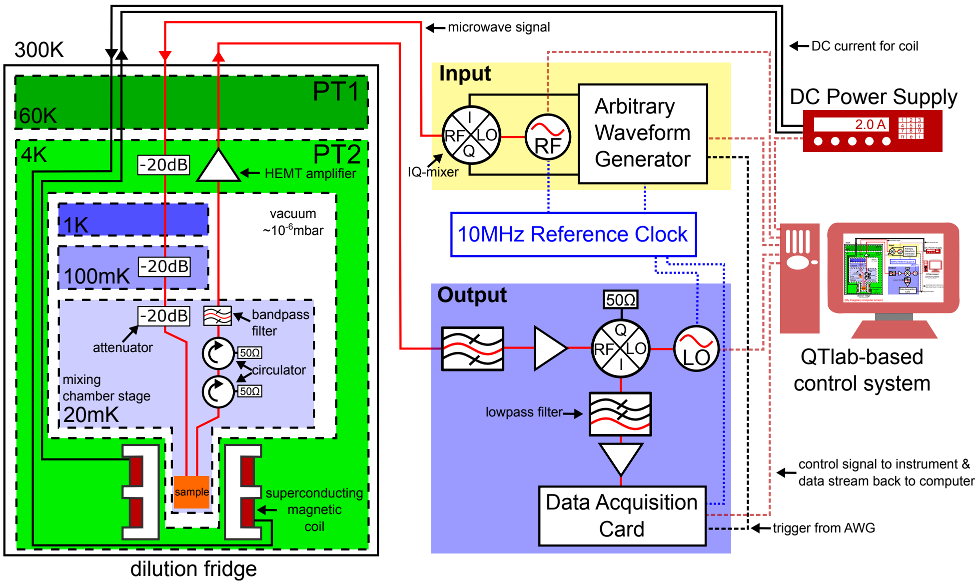

Figure 3.1: A schematic of the experimental setup, control, and measurement system.

A low-noise DC power supply provides current to a home-built superconducting magnet, which produces the field required to magnetically saturate the sample. The coil is made out of niobium-titanium wire and is in thermal contact with the 4 K PT2 stage. The magnetic field variation within the sample space was determined from simulations to be less than 0.2% and its field strength per unit current is measured to be 80 mT/Amps [51] .

A microwave source (RF in fig. 3.1) is used to generate highly monochromatic signals. For continuous-wave (CW) experiments, the signal is transmitted directly into the coaxial microwave input line. For pulsed measurements, the CW signal is modulated appropriately using an arbitrary waveform generator and an IQ-mixer, after which it is transmitted into the fridge (typical rise/fall time ~1.7 ns).

Inside the fridge, the input lines consist of semi-rigid coaxial cables and cryogenic attenuators. To minimise heat transfer between the different stages, the outer conductor of the coaxial cable is chosen to be made from stainless steel, which has low thermal conductivity. This advantageous thermal performance comes at the price of increased signal attenuation along the cables. Between the mixing chamber stage and the sample, coaxial cables with a copper-based outer conductor are used. These have lower signal attenuation and good thermal conductivity. Here, high thermal conductivity does not pose a problem because both the mixing chamber stage and the sample are at the same temperature.

There are, in total, 3×20 dB cryogenic attenuators for each input line. These attenuators help to reduce the Johnson-Nyquist noise generated by every electrical component – from the source all the way to the sample. The attenuators are positioned at various stages of the fridge such that the total Johnson-Nyquist noise temperature of the microwave signal at the sample is comparable to the mixing chamber temperature [51].

Inside the fridge, the output line consists of two cryogenic circulators, a bandpass filter, a HEMT low-noise amplifier, and several semi-rigid coaxial cables. The circulators and bandpass filter are thermally anchored to the mixing chamber stage. The circulators are usually used as isolators by terminating the third ports with $50\,\Omega$ loads. Their function is to isolate the sample from any unwanted signals propagating backward along the output line. The HEMT amplifier amplifies signals at the PT2 stage and has a gain of approximately 40 dB. To reduce the attenuation along the output line, a superconducting coaxial cable is used between the mixing chamber stage and the PT2 stage. At room temperature, the output signal is bandpass filtered, amplified, and then down-converted into a 500 MHz fixed-carrier signal using an IQ-mixer and a local oscillator signal (LO) (see fig. 3.1). The down-converted signals are then lowpass filtered and further amplified before being digitised by a fast data acquisition card (2.5 GS/s). Inside the computer, the 500 MHz carrier signal is digitally down-converted to extract its envelope (see [51]). The instrument controls, data processing (including the digital down-conversion step), and visualisations are carried out using the QTLab software platform [52]. QTLab is an open-source Python-based software that combines ease of use, compatibility with many instruments, and flexibility to adapt it to more complicated measurements.

3.2 Host materials

3.2.1 Yttrium iron garnet

One of the most commonly used magnetic materials in magnonics is single-crystal yttrium iron garnet (YIG, chemical formula: $Y_3Fe_5O_{12}$). YIG possesses a number of advantageous properties that have made it the material of choice among generations of researchers. For more than 60 years, YIG has been indispensable in prototyping magnon-based microwave devices and as a model system for the investigation of basic spin-wave physics. It is not without justification that Charles Kittel reportedly said that YIG is to ferromagnetic resonance research as what the fruit fly is to genetics [53, 54]

YIG is a ferrimagnetic insulator with a high Curie temperature (559 K) and has – in monocrystalline form – the lowest magnon damping of any known material at room temperature [53, 55–57]. Magnons can be observed to propagate in YIG over centimeter distances [3, 18]. This contrasts very favourably with magnetic metals, in which excitations can be observed over distances of no more than a few microns. Despite a complicated arrangement of 80 atoms per unit cell, YIG's crystallographic properties and optimized fabrication conditions are well known [58–60]. Today, it is possible to commercially obtain pure monocrystalline YIG of excellent quality.

Each YIG primitive unit cell has four formula units of $Y_3Fe_2^{3+}Fe_3^{3+}O_{12}^{2-}$ [59, 61]. The Fe^{3+} ions are the ones that contribute to the magnetisation. There are twenty Fe^{3+} ions in each primitive unit cell, occupying two inequivalent positions with respect to an O^{2-} environment. These are distributed over two antiferromagnetically-coupled sublattices: an octahedral lattice (eight ions) and a tetrahedral lattice (twelve ions) [3]. Each Fe^{3+} ($3d^5$) ion has a half-filled subshell ($S = 5/2, L = 0, J = 5/2, g_J = 2$) and a magnetic moment of $5\mu_B$, therefore giving rise to a total magnetic moment of $20\mu_B$ per primitive unit cell [1]. Though the material is not strictly ferromagnetic, for low energy excitations (which are our concern), we can treat

---

[1] The magnetic moments between the octahedral and tetrahedral sites are anti-parallel, therefore the net magnetisation of a primitive unit cell comes from the four Fe^{3+} ions in the tetrahedral site. As a result, the net magnetization for each primitive unit cell is $4 \times 5\mu_B = 20\mu_B$.

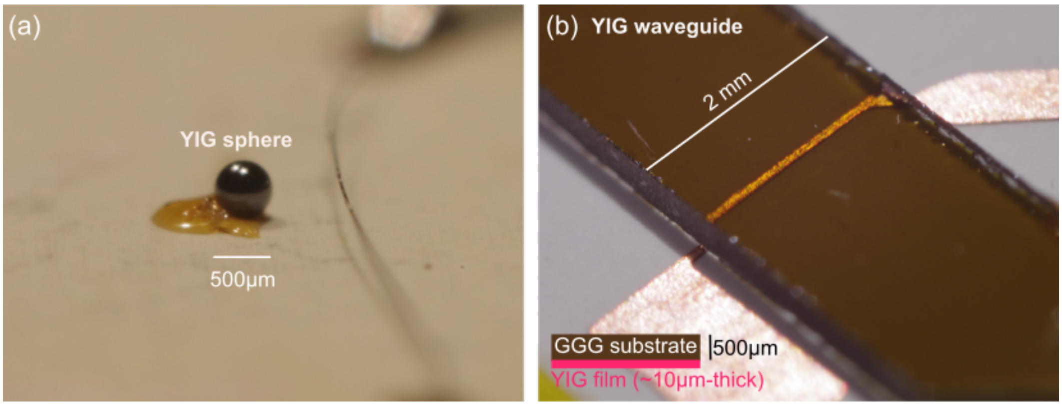

Figure 3.2: (a) A YIG sphere. (b) A YIG film on a GGG substrate. The YIG film geometry is often referred to as YIG waveguide. Photo credit: Arjan van Loo

YIG as if it were a ferromagnet. The twenty magnetic ions Fe^{3+} can be assumed to oscillate together almost in phase and are treated as one big magnetic moment [58].

YIG is produced in the form of bulk material and films (fig. 3.2). Good quality monocrystalline YIG can be grown by the floating-zone technique [62] and can be fashioned into various shapes – cubes, spheres, and discs are readily available. Of special interest in this thesis are YIG spheres. These are produced by putting a YIG cube in a tumbler, in which it is slowly shaped into a spherical shape. There are a number of commercially available widely-tunable filters and oscillators based on YIG spheres [63, 64].

The best quality YIG films are grown by liquid phase epitaxy on a gadolinium gallium garnet (GGG, $Gd_3Ga_5O_{12}$) substrate [60, 65]. GGG is used as the substrate on account of the close matching between its lattice constant (12.383 Å) and that of YIG (12.376 Å). YIG films are highly appealing in the context of the quantum circuit architecture that we are seeking to develop. Since at least the 1970s, attempts have been made to incorporate YIG-film based components into conventional silicon-based electronic systems. However this has proven to be extremely challenging due to the large lattice mismatch between YIG and silicon, and the need for a good match to assure favourable damping properties [66].

3.2.2 Other materials

Another magnetic material commonly used in magnonics is the polycrystalline metallic alloy permalloy (chemical formula: $Ni_{18}Fe_{91}$) [3]. Permalloy is more compatible with integration into silicon-based technology than YIG and is much easier to pattern, but has substantially higher damping and a lower magnon propagation speed. It is also electrically conducting, which can be inconvenient when performing experiments in which signals are able to couple to the electronic and magnonic systems simultaneously.

Other newer materials show promise of achieving low damping and compatibility with silicon-based technology, notably certain Heussler compounds [67, 68]. Moreover, recently, a new class of organic-based ferrimagnetic material, vanadium tetracyanoethylene, has been shown to have damping that is comparable to YIG [69, 70].

In our experiments, we focus our attention on YIG. The material's low damping and electrically insulating properties make it the obvious choice for prototype devices designed to operate at the quantum level.

4

Coupling Photons to Magnons

This chapter reports on the coupling between magnons in a YIG sphere and photons in a superconducting planar resonator. First, we discuss the reasons motivating the work in the area of coupled magnon-photon systems, our particular areas of interest in the context of this work, and our choice of a superconducting planar resonator as the photonic element. Next, we demonstrate and discuss the experimental observation of avoided crossings in a sphere-resonator system, which were further extended to the limit where the average number of photons and magnons are both less than one. This work has been published in [71].

4.1 Introduction

The subject of light-matter interactions has been fascinating from the outset, not just because of the beauty of the subject itself but also the broad range of emergent phenomena that it presents [20, 72, 73]. A personal favourite of the author is the inhibited spontaneous emission of an atom when placed in a mirror-cavity environment [74, 75]. The mirrors alter the available electromagnetic modes to which the excited atom can radiate, therefore modifying its spontaneous emission rate. This was a novel idea at the time when spontaneous emission was thought to be solely a property of the vacuum itself. Coincidentally, this was also one of the early pioneering ideas in the field of cavity quantum electrodynamics (cavity QED). Initially, research focused on the study of the interaction or the coupling between *single* emitters such as atoms or ions with the photonic modes within a cavity [76]. These experiments were aimed at reaching the strong coupling regime. Strong coupling is a regime in which two coupled systems are able to exchange excitations faster than the rates at which both excitations decay to the environment. In some cases, strong coupling is desirable because it enables coherent control of the quantum state of the atoms or ions (typically the non-photonic element of the coupled system) via the photons within the cavity. In addition, it is also interesting to note that the coherent exchange of excitations between light and matter can be thought as a polariton, a quasiparticle that is part light and part matter but does not behave like the individual constituent systems.

Achieving strong coupling is not an easy task experimentally, especially in the conventional single emitter and light system. This is due to the typically weak electric dipole or magnetic dipole strength of the emitter. Some of the commonly adopted strategies to achieve strong coupling regime are by increasing the photonic field amplitude within the cavity (higher cavity quality factor, tight light focusing) [77–80] or by considering alternative emitters with stronger dipole strength [28, 79]. In addition, the significant technical difficulties associated with achieving strong coupling and trapping the non-photonic system within the cavity make the process of scale-up for practical quantum information processing applications extremely challenging [27].

An alternative route is to consider the coupling between an *ensemble* of N emitters with the cavity, which offers a $\sqrt{N}$ enhancement in the coupling strength [81], making it far easier to reach the strong coupling regime. In paramagnetic spin systems such as atomic ensembles or nitrogen-vacancy centers, a high spin density is usually associated with broad linewidth due to the spin-spin interactions that tend to induce decoherence. Ferromagnetic spin ensembles are particularly interesting from this point of view because the spins are exchange-coupled and can therefore be found at a much higher number density ($\sim 10^{22}\mu_B/\mathrm{cm}^3$ vs $10^{10}\mu_B/\mathrm{cm}^3$

in paramagnetic spin ensembles)[30, 82–84]. This makes it much easier to achieve strong coupling via the $\sqrt{N}$ factor advantage.

4.2 Various implementation architectures

The investigation of coupled ferromagnetic spin ensemble and microwave cavity systems has seen considerable progress in recent years with works ranging from proofs of strong coupling in various implementation architectures to observations of the peculiar behaviours of coupled systems. Works in this area have been inspired significantly by the realisation that strong magnon-photon coupling can be easily achieved in such systems at room temperature using a relatively simpler setup than that employed in conventional cavity QED and circuit QED experiments. Some even refer to the growing field as cavity spintronics or spin cavitronics [85, 86]. Below, we summarise the recent progress in the field, which is mostly focused on experimental works.

One of the very first (if not the first) demonstrations of strong coupling between a ferromagnetic spin ensemble and a resonator is the work by Huebl et al. [87]. They measured the coupling between a slab of gallium-doped YIG and a superconducting niobium planar resonator at 50 mK in a dilution fridge. The signal-to-noise ratio in this experiment is affected by the doping of the YIG: this significantly increases the magnon damping. However, the authors of the study nonetheless observed an avoided crossing: the signature of the strong coupling regime. This work was shortly followed by those of Tabuchi et al. [30] and Zhang et al. [88], both demonstrating the strong coupling between a pure YIG sphere and a 3D rectangular cavity. Tabuchi et al. [30] performed the experiment at 10 mK in a dilution fridge and was able to extend the measurement down to the power level of single photons. Zhang et al. [88], on the other hand, performed the experiment at room temperature and demonstrated other interesting phenomena such as the Purcell effect and magnetically-induced transparency.

Following these three pioneering works, various coupling geometries were implemented as shown in table 4.1. Among these works, it should be noted that only

Resonator Architecture	**Magnetic Material**	**References**
3D rectangular cavity	YIG sphere	[30–32, 88–94]
	YIG film	[95, 96]
	GdIG	[97]
Cylindrical cavity	YIG sphere	[98–100]
	Er:YSO	[101]
	Er:YAG	[102]
Reentrant cavity	YIG sphere	[103, 104]
	YIG film	[105]
Coaxial cavity	YIG sphere	[106–108]
1D cavity	bulk YIG	[109]
	YIG sphere	[110]
Dielectric ring resonator	YIG film	[111]
Stripline resonator	YIG film	[112, 113]
Split ring resonator (SRR)	YIG film	[114–116]
Superconducting 2D resonator	YIG sphere	[71]: our work
	YIG slab	[87]
	Phosphorus-doped Si	[117]
	Permalloy stripe	[118]

Table 4.1: Various implementation architectures of magnon-photon coupling experiments.

works in [30–32, 71, 87, 89, 98, 101–105, 117] were performed at mK temperatures. In a beautiful experiment conducted in 2015, the group of Yasunobu Nakamura demonstrated strong coupling between a superconducting qubit and a YIG sphere via the 3D microwave cavity photon [31], and resolved the magnon number states [32].

The so-called *ultra*-strong coupling regime was reached by [88, 98, 103], in which the rotating wave approximation is rendered invalid and the solution to the system cannot be found analytically. There are various novel quantum phenomena anticipated to occur in the ultra-strong coupling regime [119]. It should be noted that for a sufficiently big YIG sphere (diameter above $\approx 2\,\text{mm}$), strong coupling is expected to occur within a stand alone sphere (i.e. there is no need for a cavity), between the magnon excitations and the confined photonic modes within the sphere itself [120].

Other interesting works relating to coupled magnon-photon systems include magnon gradient memory [91], magnon Kerr effect [92], cavity-mediated coupling between two magnetic moments [107], magnon-mediated coupling between two

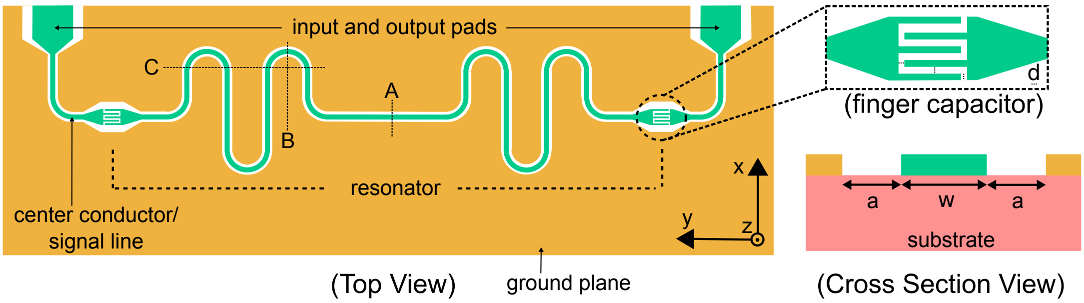

Figure 4.1: The design (top and cross sectional view) of a coplanar waveguide (CPW) resonator with two coupling capacitors on both ends acting as interface between the resonator and the external world. The inset shows the finger capacitor design in more detail. The illustration is not drawn to scale.

cavity modes [99], bistability of cavity magnon polariton [94], and level attractions due to dissipative magnon-photon coupling (instead of the usual level repulsions or anticrossings) [110].

We are interested in the experimental realisation of coupling between magnons in a YIG sphere to photons in a superconducting coplanar waveguide resonator at mK temperatures for two reasons. Firstly, such an investigation provides an ideal test-bed for our superconducting planar resonators: it is crucial that our house-designed structures retain a sufficiently good quality factor even under the presence of the sizeable in-plane magnetic field required for the experiment. This result will guide the design of our next generation superconducting device that will incorporate a non-linear element (Josephson junction). Secondly, the experimental system allows us to access high order magnetostatic modes in the YIG sphere that are otherwise difficult to address.

4.3 Superconducting planar resonator

This section discusses the coplanar waveguide (CPW) resonator used in our magnon-photon coupling experiment [121, 122].

4.3.1 Coplanar waveguide resonator

A cross-sectional view of a coplanar waveguide (CPW) is shown in fig. 4.1. It consists of a layer of centre conductor (width w) separated from two ground planes on either side (spacing a). The conducting layer sits on top of a dielectric substrate of thickness t. The CPW architecture allows for confining the electromagnetic modes in a small effective mode volume between the center conductor and the ground planes. As a result, the intensity of the electric and magnetic fields in the antinodal position can be much higher than the value typically achieved in a 3D cavity [123]. This helps in achieving strong coupling between the photon mode of the resonator and the physical system under study. Furthermore, the highly confined nature of the field means that it is very inhomogeneous around the center conductor line, making it possible to use it to couple to relatively high order magnetostatic modes.

The superconducting chip fabricated for our experiments comprises a CPW resonator in the middle with input and output pads for connections to external circuitry at either ends through wire bonds (left of fig. 4.1). Each port is connected to the resonator through a coupling capacitor. These coupling capacitors function in a similar way to the mirrors at each end of a mirror cavity, reflecting the field inside and providing an interface to the outside world. In our design, the coupling capacitors (or finger capacitors as shown in the inset of fig. 4.1) are formed from five interleaving fingers separated by a gap (width d). The meandering pattern of the CPW resonator is designed to fit the required length onto a small chip.

The transmission characteristic and the field distribution of a CPW resonator can be accurately predicted numerically. To do so, we employed the ANSYS HFSS: a high frequency structure simulator software that can calculate 3D electromagnetic fields using the finite element method. As well as being helpful in the analysis of experimental results, simulations serve as a useful tool in the iterative design of successive generations of CPW resonators (for which we may desire, for example, a narrower linewidth, or a different resonance frequency).

Figure 4.2(a) shows the predicted transmission S_{21} of a CPW resonator with parameters corresponding to the ones we used in our experiment ($w = 10\,\mu\text{m}$, $a = 4.5\,\mu\text{m}$, $d = 3\,\mu\text{m}$, resonator length 12768.5 µm, sapphire substrate). Fitting S_{21} with a Lorentzian function gives a resonance frequency of 4371.5 MHz and full-width half-maximum of 2.8 MHz.

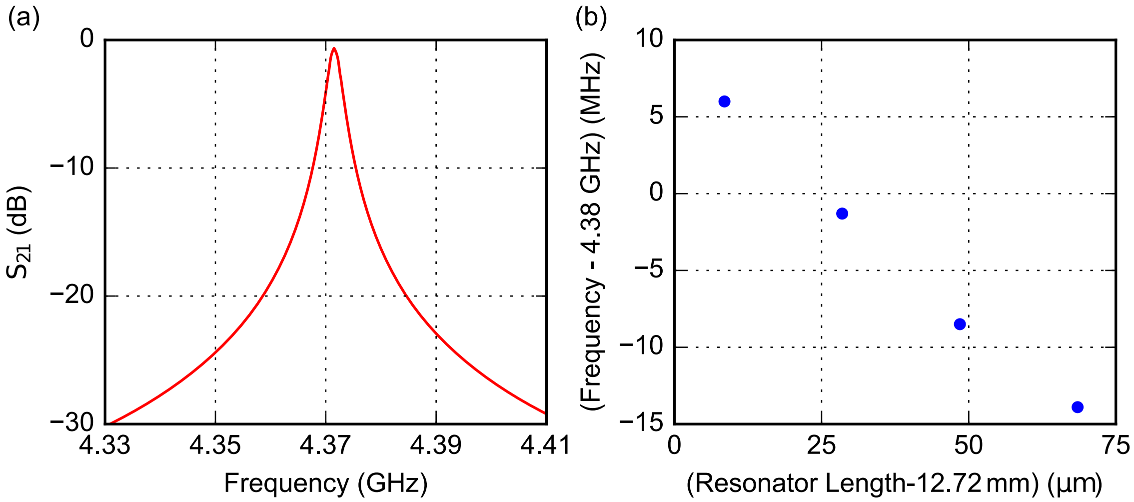

Figure 4.2: (a) Transmission of a CPW resonator calculated using HFSS. With reference to fig. 4.1, the relevant parameters are: $w = 10\,\mu\text{m}$, $a = 4.5\,\mu\text{m}$, $d = 3\,\mu\text{m}$, and the length of resonator is 12768.5 μm. The substrate is made of sapphire with a dielectric constant of 11.58 and thickness $t = 560\,\mu\text{m}$. The height of the sample-box ceiling from the surface of the chip's conducting layer is 0.5 mm. (b) The predicted resonance frequencies of a CPW resonator versus resonator length.

The thickness of the conducting layer in the simulation is intentionally set to zero. This is because the thickness of the actual conducting layer is much smaller ($\sim 150\,\text{nm}$) than the other resonator parameters. A full solution incorporating this thickness would require a mesh of comparable size. This would vastly increase the amount of computer memory and computation time without delivering any further insight into the properties of the system. The maximum mesh size on the central conductor and the finger capacitors in the simulation is set to be equal to w and d respectively. This is to ensure that the field around the finger capacitors and in the gap between the central line and the ground plane is well modelled.

To demonstrate the functionality of the model, the resonance frequencies of resonators with different lengths are extracted from the HFSS simulation. Figure 4.2(b) shows that the resonance frequency of the resonator decreases as the length of the resonator is increased. This is expected because a longer resonator is able to accommodate standing waves with longer wavelengths.

It is also possible to visualise the magnetic and electric vector fields around the resonator from the full HFSS simulation. Figure 4.3(a) shows the fields at the middle of the resonator (cross section A in fig. 4.1) where the antinode of the

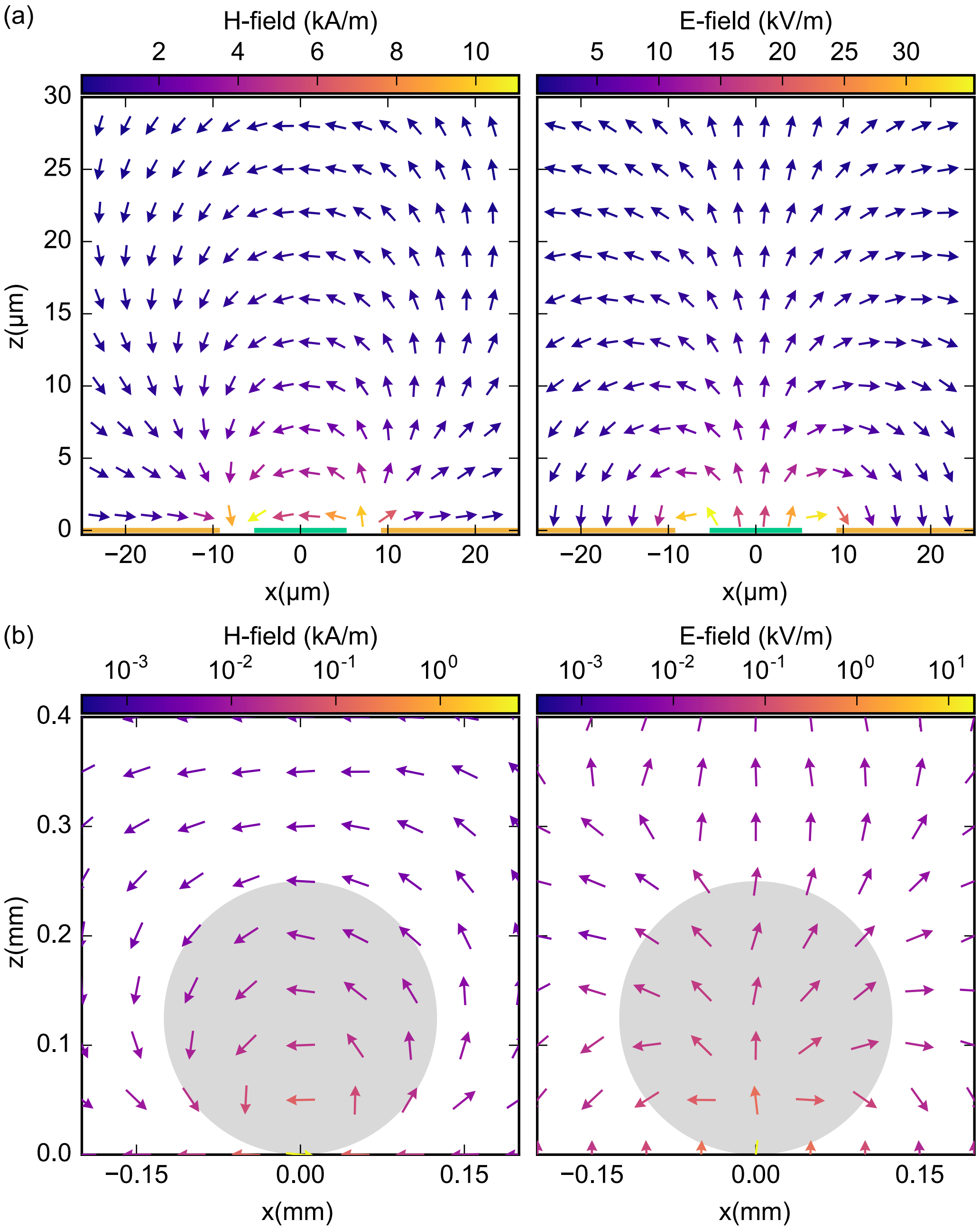

Figure 4.3: (a) Magnetic (H) and electric (E) vector fields at the central region of the resonator (cross section A in fig. 4.1), focusing on the region around the centre conductor. The size of the centre conductor and its distance from the ground planes are drawn to scale as shown on the $z = 0$ axis. The resonator is excited at its fundamental mode. (b) Similar to (a), except that the fields are drawn at a length scale comparable to the diameter of the YIG sphere used in the experiment (shown on the plot as a shaded 0.25 mm diameter circle). Note that the colour map in panel (b) is plotted on a logarithmic scale.

magnetic field of the fundamental resonator mode is expected to occur. As shown in the figure, the amplitudes of the magnetic and electric fields are the highest in the space between the centre conductor and the ground planes, decreasing rapidly as one proceeds further from the resonator.

Figure 4.3(b) shows the vector electric and magnetic fields at a length scale similar to the YIG sphere used in our experiment, which has a diameter of 0.25 mm. The direction and strength of the magnetic field across the region occupied by the YIG sphere determine the magnetostatic modes that will be preferentially excited in the experiment. By calculating the overlap integral between the field profile of the CPW resonator and the magnetisation field of the magnetostatic modes of the YIG sphere, it is possible to compare the relative coupling strength between the different modes as shown in [51, 71].

4.3.2 Aluminium and niobium thin-film resonators

The first generation resonators fabricated by our group have an aluminium thin-film conducting layer and a sapphire wafer substrate. These aluminium devices were fabricated on-site in the Clarendon Laboratory clean room. In brief, the sapphire crystal substrate is coated with a photoresist and patterned using UV photolithography. A thin layer (thickness $\sim$ 50 nm$-$100 nm) of aluminium is evaporated onto its surface, and the unwanted part of this film and the photoresist layer are lifted off. The wafer is subsequently diced to extract all of the devices. Figure 4.4(a) shows below a patterned wafer prior to dicing.

Aluminium thin films are known to have a critical magnetic field below that required to bias our samples (not more than 70 mT for a 50 nm aluminium layer at 1 K [124]). It is not possible, with our experimental setup, to tilt the direction of the magnetic field in three dimensional space while the dilution fridge is in operation. As a result, it proved very challenging to align the plane of the aluminium film with the field – a process which would, in principle, allow the superconductivity to be preserved in a more substantial applied field. In response to these difficulties, we produced a second generation of resonators using niobium as the conducting

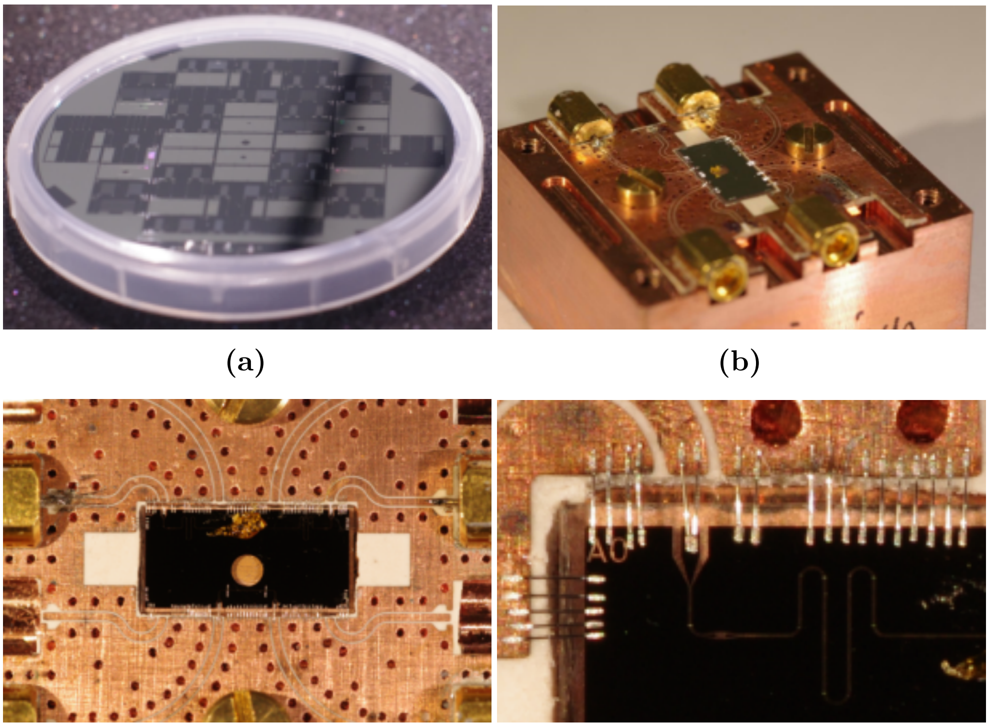

Figure 4.4: (a) Superconducting devices fabricated on a sapphire crystal substrate. (b) A printed circuit board (PCB) attached to an open sample holder. (c) A device under study is positioned at the centre of the PCB. (d) Aluminium wire-bonds connect the coplanar waveguide resonator to the PCB. [Photo credit: A. F. van Loo]

layer. Niobium is a type II superconductor with a higher critical field (200 mT for a 52 nm niobium layer at 4.5 K [125]). As we do not currently have suitable in-house etching facility, niobium device fabrication (film thickness ~ 150 nm) was outsourced to a company in the United States.

Figure 4.4(b) shows one of the niobium chips mounted into a microwave printed circuit board (PCB) and installed in a copper sample holder designed for our experiments. The PCB is attached to the sample holder using brass screws and the chip is glued onto the sample holder using GE varnish. The PCB consists of eight measurement ports in total and is designed to accept high-frequency MMPX connectors as shown in fig. 4.4(c).

The device is connected to the PCB using wire bonds which were applied in the clean room. Wire-bonding on aluminium and niobium devices is very similar in term of optimum machine parameters. Aluminium wire was used with a diameter of 25 µm. The current chip design allows for two wire-bonds to be fitted onto each signal pad. As many wire bonds as possible are applied to the ground plane so as to ensure that the whole structure sits at the same potential. Figure 4.4(d) shows an example of a wire-bonded niobium device containing a CPW resonator.

4.3.3 Experimental characterisations

A useful parameter used to characterise a resonator is the quality or Q-factor, defined as the ratio between the resonance frequency ($f_\circ$) and the full-width of the response at half its maximum value (Δf), i.e.

$$Q = \frac{f_\circ}{\Delta f}. \tag{4.1}$$

Thus, the higher the Q-factor, the narrower the linewidth [122].

Figure 4.5 shows the frequency response of both aluminium-based and niobium-based CPW resonators measured as a function of the applied magnetic field at millikelvin temperatures. The magnetic field is manually aligned (at room temperature) to be approximately parallel to the device's plane in the y-direction as shown in fig. 4.1. This in-plane field configuration is chosen to be perpendicular to the microwave magnetic field generated by the CPW resonator. This ensures that the microwave field couples efficiently to the magnetic material. In a superconducting thin film, magnetic field can penetrate through the film if its thickness is comparable to its penetration depth, even though it the material is originally a type I superconductor in bulk. This leads to the formation of Abrikosov vortices and a critical field higher than its bulk value. The energy dissipation due to Abrikosov vortices leads to a more lossy resonator and modification of its equivalent RLC-circuit, this in turns causes the shift in the resonance frequency and the Q-factor of the resonators as a function of magnetic field [51, 124, 126].

The performance of the aluminium thin-film resonator is shown fig. 4.5. Under zero field, the Q-factor of the resonator is approximately 800. As the applied magnetic field increases, the Q-factor and the signal level of the resonator start to decrease. The signal becomes very weak for magnetic fields above 40 mT. Typical

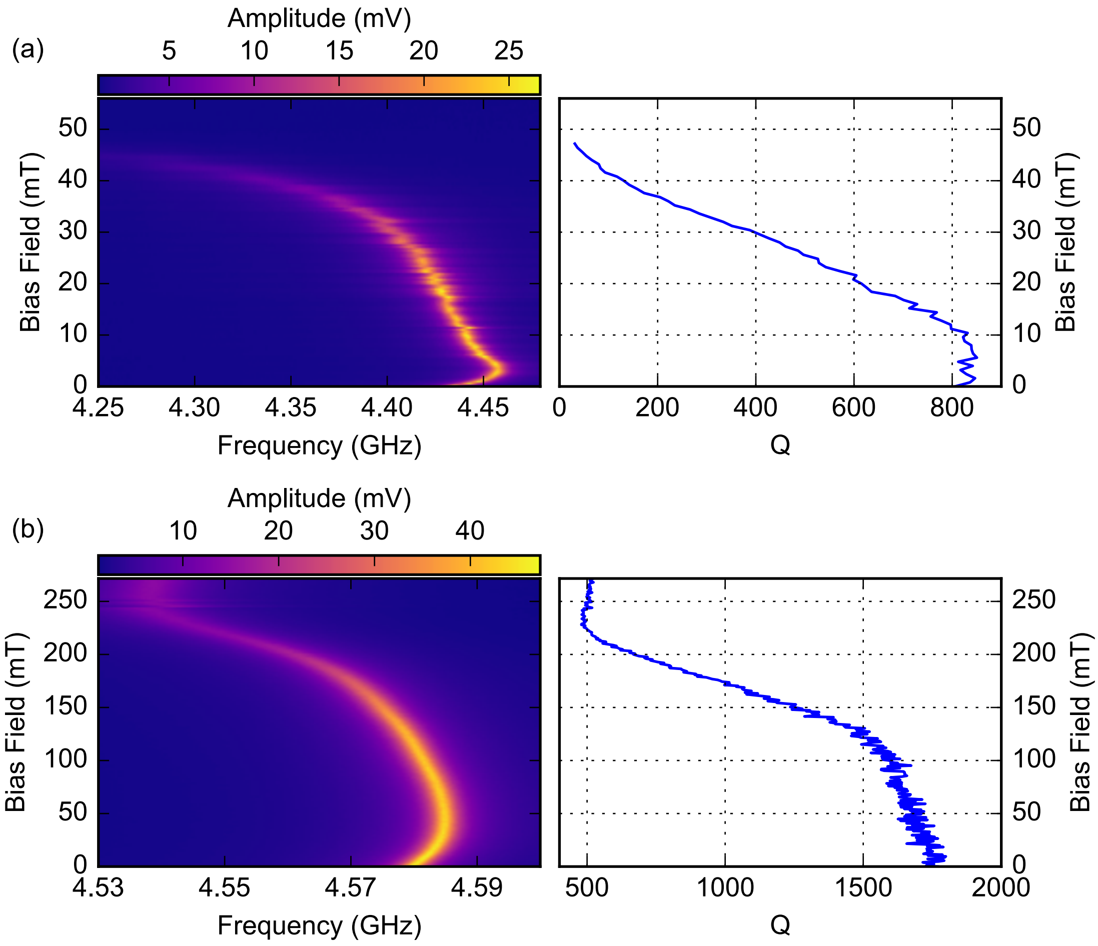

Figure 4.5: Frequency response of CPW resonators ((a) aluminium, (b) niobium) as a function of magnetic field aligned approximately parallel to the plane of the device. The amplitude scale is the voltage measured by the data acquisition card. Shown on the right is the extracted Q-factor as a function of magnetic field.

experiments involving magnon excitation in YIG require a bias magnetic field above 100 mT indicating that, at least without more sophisticated alignment equipment to more precisely position the film parallel to the applied field, the aluminium resonators have severe limitations.

The niobium thin-film resonator shows dramatically better resilience to applied magnetic field. Figure 4.5(b) shows the frequency response and the Q-factor of the niobium resonator measured up to 271 mT. The Q-factor of the Niobium resonator is substantially higher than the one obtained in the aluminium resonator across the full range of magnetic fields. The decrease in Q-factor is relatively small until the field reaches 120 mT.

4.4 Magnon-photon coupling experiments

In this section, we present measurements that demonstrate the strong coupling between photons in a niobium CPW resonator ($w = 10\mu\text{m}$, $a = 4.5\mu\text{m}$, $d = 3\mu\text{m}$, sapphire substrate) and magnons in a YIG sphere (diameter 0.25 mm) at millikelvin temperatures. The resonator is excited at its fundamental frequency with the antinode of the microwave magnetic field located at the centre of the resonator (intersection between the dashed line A in fig. 4.1 and the resonator). To maximise the likelihood of achieving strong coupling, the YIG sphere is glued directly on top of the resonator at the location of field antinode using GE varnish. The bias magnetic field is applied parallel to the y-axis in fig. 4.1. In this configuration, the bias field is parallel to the device plane and perpendicular to the microwave magnetic field generated by the resonator.

4.4.1 High power limit

Figures 4.6 shows the frequency response of the combined YIG-resonator system as a function of the bias magnetic field at relatively high input power, i.e. with many photons in the resonator. In comparison with the data shown in fig. 4.5(b) where the YIG sphere is not present, several avoided crossings are observed in these data. Each avoided crossing is a sign of strong coupling between a particular magnetostatic mode of the YIG sphere and the photons of the resonator, indicating that the combined system is able to exchange excitations faster than the rate at which the excitations leak out of the resonator and the YIG sphere. Some of the avoided crossings have been identified as the (n, n) magnetostatic modes as shown in [51]. The weak absorption lines in between the avoided crossings are indication of weakly-coupled higher-order modes.

Figure 4.7(a) shows a zoomed-in view of fig. 4.6 in the region where the $(1, 1)$ or Kittel mode of the YIG sphere is in the vicinity of the resonance frequency of the resonator. The data is obtained in the high power limit. The linecut shows the clear appearance of an avoided crossing: the sign of strong coupling.

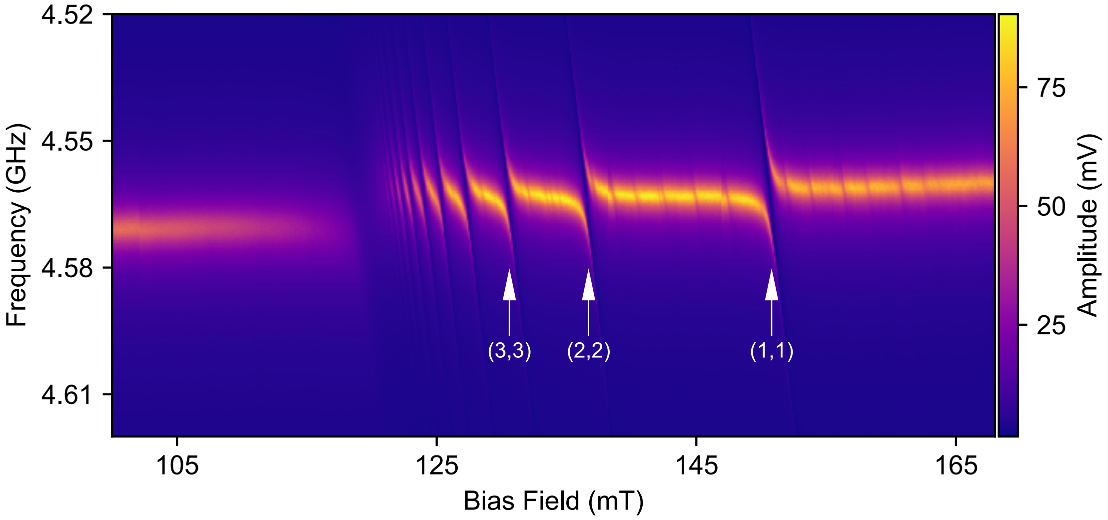

Figure 4.6: Frequency response of the coupled YIG sphere/niobium CPW resonator system as a function of bias magnetic field. The data shows a number of avoided crossings and weaker absorption lines. The (n, n) magnetostatic modes in the sphere identified in this experiment are shown in the figure. The $(1, 1)$ mode is the Kittel mode (see Section 2.6.2) and corresponds to the uniform precession mode in the sphere. In this figure, the vertical axis is plotted in decreasing frequency.

The magnon-photon coupling can be modelled as two coupled harmonic oscillators (magnons and photons) with eigenfrequencies (f) given by [20, 73, 127]:

$$f = f_{\text{o}} + \frac{\Delta}{2} \pm \frac{1}{2}\sqrt{\Delta^2 + 4g_{\text{eff}}^2}, \tag{4.2}$$

with $\Delta = f_{(1,1)} - f_{\text{o}}$ where $f_{(1,1)}$, f_{o}, and g_{eff} are respectively the frequency of the sphere $(1, 1)$ mode, the resonance frequency of the resonator, and the effective coupling strength between the oscillators. From the separation of the peaks in fig. 4.7(a), the effective coupling strength is found to be approximately $g_{\text{eff}} \approx 8\,\text{MHz}$. A more reliable way to extract the coupling parameters is to fit the data using an expression for the transmission through the coupled system derived using the input-output formalism of quantum optics as demonstrated in [51, 71].

4.4.2 Single photon power limit

Having completed a series of high-power measurements, we moved on to reduce the power of the microwave signal used to excite the resonator to the single photon power limit in which the average number of photons at the input of the resonator

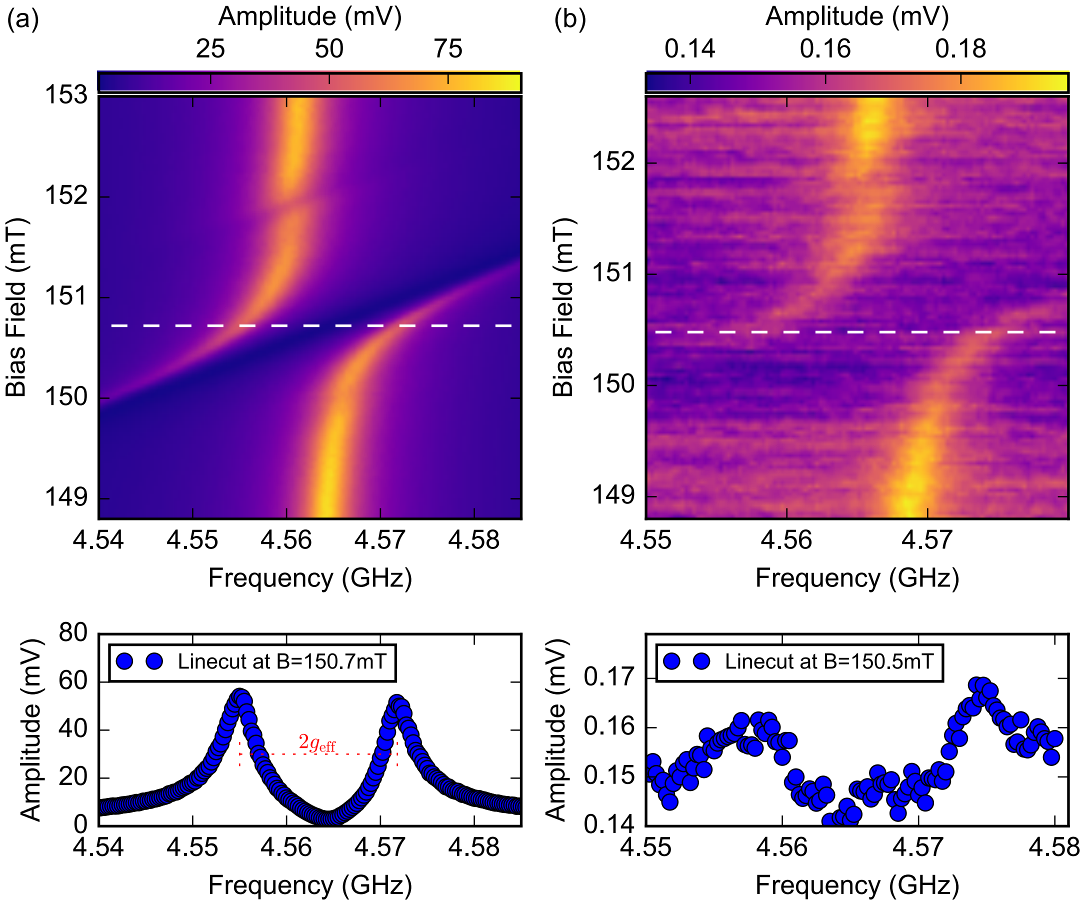

Figure 4.7: Frequency response of the system when the $(1, 1)$ magnetostatic or Kittel mode of the YIG sphere is tuned to the resonance frequency of the resonator. (a) High power regime. (b) Single photon power regime when there is, on average, less than 1 photon in the resonator.

is less than 1. The average number of photons (n) here is defined with respect to inverse of the bare resonator linewidth, i.e.

$$n = \frac{P_{\mathrm{RF}}}{hf_{\mathrm{o}}}\frac{1}{\Delta f}, \tag{4.3}$$

where P_{RF}, f_{o} and Δf are the input microwave power, the resonance frequency of the resonator, and the resonator linewidth.

Figure 4.7 shows the avoided crossing of the $(1, 1)$ mode with the photon mode at the low power limit. Our calculation shows that the average number of photons at the input of the resonator for our input power level is $n \approx 0.47$. A clear avoided crossing is still observed at this power level albeit with a much lower signal-to-noise ratio. These data were obtained by averaging the measurements for several days. The effective coupling strength in this case is similar to the one obtained in high power limit.

It should be noted that the input photon state is still a coherent state, albeit one with an extremely low average number of photons. It is not the number (Fock) state, which would require a superconducting circuit as the single photon source [31]. As well as being of interest in and of themselves, the results reported in this chapter demonstrate the capability of our system to operate in the single photon power regime while maintaining the ability to extract a clear signal from the experiment.

4.4.3 Comparison with other experiments

The experimental works listed in table 4.1 that specifically investigated the coupling between a YIG sphere and a cavity/resonator reported a wide range of coupling strengths g_{eff}. Some of the high values can be attributed to the use of larger YIG spheres — in these cases there are more spins available to couple to the cavity/resonator mode.

In order to directly compare the coupling performances of various cavity/resonator architectures, it is necessary to normalise the reported g_{eff} values. Table 4.2 compares the published g_{eff} values ($g_{\text{eff,rep}}$) and their equivalent values ($g_{\text{eff,equiv}}$) referenced to a 0.25 mm-diameter sphere. The equivalent g_{eff} value is calculated based on the $\sqrt{N}$ proportionality relation [81]. Assuming the use of pure YIG, then the spin density is a constant, and

$$\frac{g_{\text{eff,equiv}}}{g_{\text{eff,rep}}} = \sqrt{\frac{(0.25\,\text{mm})^3}{D^3}}. \tag{4.4}$$

As shown in table 4.2, our 2D/planar resonator architecture is able to achieve a coupling strength that is comparable to the ones in 3D rectangular cavities. The reentrant cavity architecture achieves the highest equivalent coupling strength: this is to be expected as such a cavity is designed to focus the magnetic field within the cavity in the region of the sample.

Coupling strength is not the sole indicator of the performance within a coupled resonator system. Another important parameters to be considered is the rate at

System	**Diameters**	**Reported g_{eff}**	**Equivalent g_{eff}**
1D cavity [110]	1 mm	39 MHz	4.9 MHz
3D rectangular cavity [30, 88, 89, 92, 94]	0.25-1.0 mm	7.5-47 MHz	5.1-10.8 MHz
Superconducting 2D resonator (our work [71])	0.25 mm	8 MHz	8 MHz
Coaxial cavity [106–108]	1 mm	130-150 MHz	16.3-18.8 MHz
Cylindrical cavity [98]	5 mm	3.6 GHz	39.7 MHz
Reentrant cavity [103, 104]	0.8-1 mm	1.5-2 GHz	183-280 MHz

Table 4.2: Comparison between the various g_{eff} values reported in the literature and their equivalent values for a 0.25 mm diameter sphere.

which energy leaks out of the coupled system. If such information is available, various coupled resonator system can also be compared using the cooperativity parameter ($C = 4g^2/(\kappa\gamma)$), where κ and γ are the dissipation rates of the resonator/cavity and the magnetic systems). For instance, without accounting for the different sphere size, the cooperativity in our system is $C \sim 66$ [51], which can be compared with other values of cooperativity that are readily available, such as: $C \sim 3000$ in the work of Tabuchi et al [30], and $C \sim 200$ in the work of Lambert et al [106].

In the case of our experiment, it is not possible to achieve a stronger coupling by using a larger YIG sphere. This is because the coupling is limited not by the size of the magnetic system, but by the strong confinement of the magnetic field around the region near the center conductor. It is this strong confinement that makes it possible to access many higher-order modes of the sphere. If larger coupling were desired, this could be achieved by modifying the resonator design in such a way as to produce a magnetic field that overlaps more significantly with one of its modes. But this would come at the price of the visibility of other modes.

In conclusion, we have demonstrated a strongly-coupled magnon-photon system combining a YIG sphere and a superconducting niobium-based CPW resonator. The quality factor of the niobium resonator is shown to remain high at the magnetic fields required for magnon-related investigations. This highlights the promise of the planar circuit architecture incorporating non-linear elements which we are developing for future low-temperature magnonic experiments.

5

YIG-based Magnonic Crystals

This chapter reports on the first measurements of a static magnonic crystal based on a YIG film at 20 mK. First, we introduce the concept of a magnonic crystal and the transfer matrix method that can be used to predict its transmission characteristics. We go on to discuss our experimental results both at room temperature and at 20 mK. This work has been published in [128].

5.1 Introduction

Magnonic crystals are magnetic waveguides or films with periodic modulations in their magnetic properties that affects the dispersion of magnons propagating through them. If the length scale of the modulations is comparable to the wavelength of the propagating magnons, the spectra of the crystals feature bandgaps, i.e. energy gaps in which magnons are not allowed to propagate. As the magnon dispersion is tuneable via an external magnetic field, the positions in frequency space of the bandgaps can be varied over a significant range. In the context of the broader class of so-called “artificial crystals”, systems which incorporate, for example, optical and acoustic structures, this tuning functionality is unique.

Magnonic crystals are one of the building blocks of room-temperature magnonics [9, 14]. They have played a central role in a number of studies looking into the basic physics of waves and quasi-particle systems, such as: energy exchange between counter-propagating spin-waves [129], all-linear time reversal of signals [19], and coherent wave trapping and recovery [130]. Magnonic crystals have also been used to create a wide range of devices including oscillators and filters [132], logic gates [133], and magnon transistors [18].

Magnonics crystals can, in principle, be one-, two-, or three- dimensional structures. However, 2D and 3D magnonic structures are complex to build and measure, and therefore one-dimensional magnonic crystals are often preferred for fundamental studies. For this reason, in our work we shall focus exclusively on the 1D structures; those curious about 2D and 3D magnonic crystals are referred to Ref. [9].

One-dimensional magnonic crystals exist in two classes — so-called static and dynamic variants. A static magnonic crystal has a modulation in its magnetic properties that is fixed and cannot be varied in time. A static magnonic crystal can be produced, for instance, by engineering periodic modulations in a magnetic waveguide's thickness (achieved in YIG [134, 135]), width (achieved in permalloy [136]), or saturation magnetisation (achieved in permalloy [137]). Modification in the geometric structure of a YIG waveguide to create a magnonic crystal is typically achieved through photolithographic patterning and hot orthophosphoric acid etching. A dynamic magnonic crystal has a modulation parameter that can be varied in time during experiments. The first example of such structure was the current-controlled dynamic magnonic crystal [138]. The operation of this device relies on the presence of a periodic array of current-carrying wires in close proximity to the surface of a YIG waveguide. When current passes through the array, the resulting magnetic field produces a periodic variation in the local bias field on a timescale that is short in comparison with the time taken for a magnon signal to propagate through it. This functionality opens doors to the possibility to observe a range of interesting physical effects [19, 129]. Other dynamic magnonic crystals have been based around thermally-induced magnetic modulations [139] and surface acoustic waves [140].

Before the work detailed in this chapter, all experiments conducted on magnonic crystal systems had been undertaken at room temperature. It is clear that the

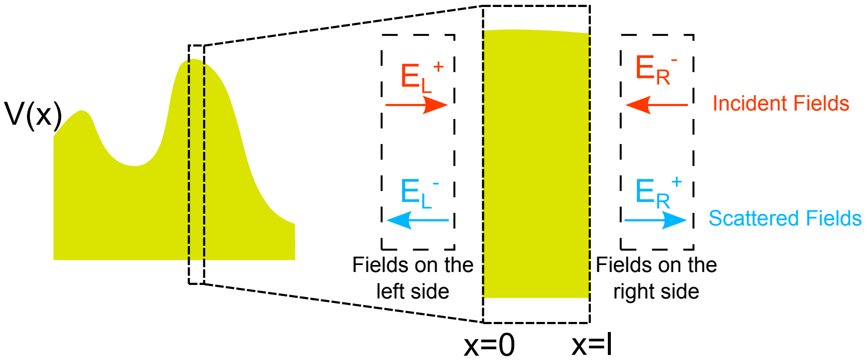

Figure 5.1: A system with a potential barrier of arbitrary shape $V(x)$ is decomposed into smaller subsystems with a potential landscape that can be represented by a simpler transfer or scattering matrix.

functionality of magnonic crystals could find significant applications in solid-state quantum devices. We set about to perform a first set of such investigations into the use of magnonic crystals at the millikelvin temperatures required for microwave-frequency quantum experiments. We chose a thickness-modulated YIG-based magnonic crystal as our test system.

5.2 Theory of magnonic crystals

Here, we introduce the basics of the transfer matrix method first employed by Chumak et al. [134] to predict the transmission characteristics of thickness-modulated magnonic crystals.

5.2.1 Transfer matrices and scattering matrices

The scattering matrix $\boldsymbol{S}$ relates the fields incident on the crystal (E_L^+, E_R^-) to those scattered from it (E_L^-, E_R^+) as shown in fig. 5.1. The matrix elements of the scattering matrix are obtained from experiments ($|S_{ii}|^2$ is the reflectance, $|S_{ij}|^2$ is the transmittance):

$$\underbrace{\begin{pmatrix} E_\mathrm{L}^-(x=0) \\ E_\mathrm{R}^+(x=l) \end{pmatrix}}_{\text{Scattered Fields}} = \boldsymbol{S} \underbrace{\begin{pmatrix} E_\mathrm{L}^+(x=0) \\ E_\mathrm{R}^-(x=l) \end{pmatrix}}_{\text{Incident Fields}}. \tag{5.1}$$

The transfer matrix $\boldsymbol{M}$ relates the fields on the left (E_{L}^{-}, E_{L}^{+}) to the fields on the right side of the crystal (E_{R}^{-}, E_{R}^{+}) (see fig. 5.1), i.e.

$$\underbrace{\begin{pmatrix} E_{\mathrm{L}}^{+}(x=0) \\ E_{\mathrm{L}}^{-}(x=0) \end{pmatrix}}_{\text{Fields on the left}} = \boldsymbol{M} \underbrace{\begin{pmatrix} E_{\mathrm{R}}^{+}(x=l) \\ E_{\mathrm{R}}^{-}(x=l) \end{pmatrix}}_{\text{Fields on the right}} . \tag{5.2}$$

For instance, if the potential is zero and the excitation simply propagates as a plane wave across the system, then:

$$\boldsymbol{M} = \begin{pmatrix} e^{(-ik+k'')l} & 0 \\ 0 & e^{(ik-k'')l} \end{pmatrix} \tag{5.3}$$

where k and k'' are respectively the wavevector and the spatial decay rate, and l is the traversed distance.

The transfer matrix formalism comes into its own for the analysis of geometrically-composed systems. It allows an arbitrary potential to be broken into an ordered sequence of independent subsystems that can be represented by simple transfer matrices, i.e. $\boldsymbol{M_1}, \boldsymbol{M_2}, ..., \boldsymbol{M_n}$. The overall transfer matrix ($\boldsymbol{M_T}$) is then the ordered product of the subsystem transfer matrices, $\boldsymbol{M_T} = \boldsymbol{M_1}\boldsymbol{M_2}...\boldsymbol{M_n}$.

For a periodic system with N repeating unit cells (the case relevant to a magnonic crystal), the overall transfer matrix $\boldsymbol{M_T}$ is simply the transfer matrix of a unit cell $\boldsymbol{M}$ raised to the power of the number of unit cells N, i.e. $\boldsymbol{M_T} = \boldsymbol{M}^N$. To calculate the transmittance or the reflectance of such system, one converts the transfer matrix to the scattering matrix through the following relations:

$$\boldsymbol{S} = \begin{pmatrix} S_{11} & S_{12} \\ S_{21} & S_{22} \end{pmatrix} = \begin{pmatrix} \frac{M_{21}}{M_{11}} & M_{22} - \frac{M_{12}M_{21}}{M_{11}} \\ \frac{1}{M_{11}} & -\frac{M_{12}}{M_{11}} \end{pmatrix}, \tag{5.4}$$

$$\boldsymbol{M} = \begin{pmatrix} M_{11} & M_{12} \\ M_{21} & M_{22} \end{pmatrix} = \begin{pmatrix} \frac{1}{S_{21}} & -\frac{S_{22}}{S_{21}} \\ \frac{S_{11}}{S_{21}} & S_{12} - \frac{S_{11}S_{22}}{S_{21}} \end{pmatrix}. \tag{5.5}$$

It should be pointed out that for a system in which energy is conserved, the transfer matrix satisfies the following relations: $M_{22} = M_{11}^{*}$ and $\mathrm{Tr}(\boldsymbol{M})$ is real. In such a system, any solutions that are propagating waves must obey: $|\mathrm{Tr}(\boldsymbol{M})| \leq 2$. If $|\mathrm{Tr}(\boldsymbol{M})| > 2$, the solution is located within the bandgap, i.e. it is a bound state. This trace criterion enables us to quickly determine the bandgap regions of the system. For further information, the reader is directed to Ref. [141].

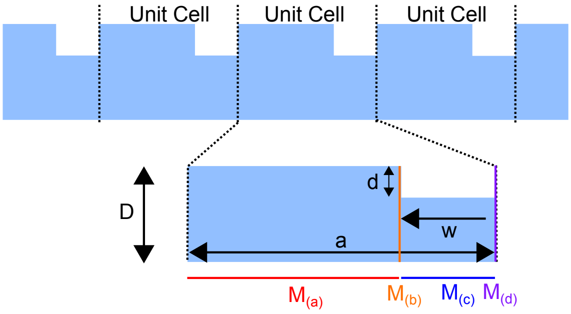

Figure 5.2: Illustration of a thickness-modulated magnonic crystal with its unit cells.

5.2.2 Transfer matrix method applied to magnonic crystals

The magnonic crystal used in our study is a thickness-modulated YIG waveguide with a structure illustrated in fig. 5.2. The thickness of the un-etched region is D, the width and depth of each groove are w and d respectively, and a is the spacing between neighbouring grooves. We apply a bias field parallel to the plane of the film.

The cross section of each groove is assumed to be rectangular-shaped with sharp edges and to be identical to all others. In reality, the true profile of the groove is usually narrower at its bottom due to the inherent anisotropy of the chemical etching process used to create it [134]. The macroscopic size of our crystal means that we only need to consider the transport of dipolar magnons.

As the magnonic crystal consists of identical periodically-spaced etched grooves, simulating the transmission properties can be simplified to finding the transfer matrix of a single unit cell of the magnonic crystal $\boldsymbol{M}$ and raising this matrix to the power of the number of the grooves. We divide the unit cell into 4 simple segments as shown in fig. 5.2, each with a corresponding transfer matrix:

- $\boldsymbol{M}_{\mathbf{(a)}}$: propagation across the un-etched region of the waveguide (length $a - w$ and thickness D),
- $\boldsymbol{M}_{\mathbf{(b)}}$: transition from the un-etched to the etched region of the waveguide,
- $\boldsymbol{M}_{\mathbf{(c)}}$: propagation across the etched region of the waveguide (length w and thickness $D - d$),
- $\boldsymbol{M}_{\mathbf{(d)}}$: transition from the etched to the un-etched region of the waveguide.

The overall transfer matrix for a single unit cell is then $\boldsymbol{M} = \boldsymbol{M_{(a)}}\boldsymbol{M_{(b)}}\boldsymbol{M_{(c)}}\boldsymbol{M_{(d)}}$. The matrices $\boldsymbol{M_{(a)}}$ and $\boldsymbol{M_{(c)}}$ are both represented by propagation matrices that incorporate the appropriate phase delay and propagation decay. Letting $k_{(\mathrm{a})}$ and $k_{(\mathrm{c})}$ be, respectively, the wavevectors of magnons in the un-etched and the etched regions, and $k''_{(\mathrm{a})}$ and $k''_{(\mathrm{c})}$ be the associated spatial decay rates, then:

$$\boldsymbol{M_{(a)}} = \begin{pmatrix} e^{(-ik_{(\mathrm{a})}+k''_{(\mathrm{a})})(a-w)} & 0 \\ 0 & e^{(ik_{(\mathrm{a})}-k''_{(\mathrm{a})})(a-w)} \end{pmatrix}, \tag{5.6}$$

$$\boldsymbol{M_{(c)}} = \begin{pmatrix} e^{(-ik_{(\mathrm{c})}+k''_{(\mathrm{c})})w} & 0 \\ 0 & e^{(ik_{(\mathrm{c})}-k''_{(\mathrm{c})})w} \end{pmatrix}. \tag{5.7}$$

The dispersion relation of magnons propagating between grooves (in the un-etched region) is assumed to be the same as if they were propagating in an unstructured waveguide with thickness D. This approximation is most valid in the limit where the groove width is much smaller than the inter-groove spacing ($w \ll a$) or the groove depth is much smaller than waveguide's thickness ($d \ll D$). We recall that the dipolar magnon dispersion relations for films (see Sections 2.6.3 and 2.6.4) can always be divided into a term that depends on the product of the wavevector and the film thickness ($k_{\mathrm{t}}S$), and another that depends solely on other variables ($\omega_0, \omega_{\mathrm{M}}, \omega$). Therefore, the magnon wavevector in the etched region can be expressed as

$$k_{(\mathrm{c})}(D-d) = k_{(\mathrm{a})}D, \tag{5.8}$$

$$k_{(\mathrm{c})} = k_{(\mathrm{a})}\frac{D}{D-d}. \tag{5.9}$$

The spatial decay rate in the un-etched region can be written as [35]:

$$k''_{(\mathrm{a})} = \gamma\mu_{\circ}\frac{\Delta H}{2v_{\mathrm{g}}} \tag{5.10}$$

where γ is the gyromagnetic ratio of an electron, ΔH is the linewidth of the uniform precession mode (a measure of the magnon damping), and v_{g} is the magnon group velocity. The spatial decay rate in the etched region is:

$$k''_{(\mathrm{c})} = k''_{(\mathrm{a})}\frac{D}{D-d}\left(1+\zeta\frac{d}{D}\right) \tag{5.11}$$

where the phenomenological parameter ζ accounts for additional loss due to enhanced two-magnon processes originating from the surface roughness of the grooves.

The transfer matrices $\boldsymbol{M}_{\mathbf{(b)}}$ and $\boldsymbol{M}_{\mathbf{(d)}}$ are related to the transmission and reflection of magnons across the boundary of the etched and the un-etched region of the waveguide. The magnon reflection coefficient Γ across the boundary is the magnetic analogue of the reflection coefficient across transmission lines of different characteristic impedance (from Z_0 to Z) [122], i.e.

$$\Gamma_{\mathrm{TL}} = \frac{Z - Z_0}{Z + Z_0}. \tag{5.12}$$

Continuing with the transmission-line analogy, the change in waveguide's thickness is equivalent to a change in the effective inductance of a lossless line. The characteristic impedance of a lossless transmission line is $Z = \sqrt{\frac{L}{C}} = \frac{1}{\omega C}\omega\sqrt{LC} = \frac{k}{\omega C}$, where L and C are, respectively, the inductance and the capacitance per unit length. Therefore, the reflection coefficient of magnons moving from the un-etched to the etched region is:

$$\begin{aligned}
\Gamma = \eta\Gamma_{\mathrm{TL}} &= \eta\frac{k_{\text{etched}} - k_{\text{un-etched}}}{k_{\text{etched}} + k_{\text{un-etched}}}, & (5.13)\\
&= \eta\frac{k_{(\mathrm{c})} - k_{(\mathrm{a})}}{k_{(\mathrm{c})} + k_{(\mathrm{a})}}, & (5.14)\\
&= \eta\frac{D - (D - d)}{D + (D + d)}, & (5.15)\\
&= \eta\frac{d}{2D + d}, & (5.16)
\end{aligned}$$

where η is a phenomenological parameter introduced to account for the fact that the experimentally observed reflection amplitude depends on whether the magnons are of backward-volume type (BVMSW) or surface type (MSSW). It is easily shown that the reflection coefficient for magnons going from the etched to the un-etched region is $-\Gamma$. Therefore the corresponding transfer matrices are

$$\begin{aligned}
\boldsymbol{M}_{\mathbf{(b)}}(\Gamma) &= \begin{pmatrix} \frac{1}{1-\Gamma} & \frac{\Gamma}{1-\Gamma} \\ \frac{\Gamma}{1-\Gamma} & \frac{1}{1-\Gamma} \end{pmatrix}, & (5.17)\\
\boldsymbol{M}_{\mathbf{(d)}}(\Gamma) &= \begin{pmatrix} \frac{1}{1+\Gamma} & \frac{-\Gamma}{1+\Gamma} \\ \frac{-\Gamma}{1+\Gamma} & \frac{1}{1+\Gamma} \end{pmatrix}. & (5.18)
\end{aligned}$$

The matrix elements of a single unit cell's transfer matrix are:

$$M_{11} = \frac{1}{1-\Gamma^2} e^{\left(-ik_{(\mathrm{a})}+k''_{(\mathrm{a})}\right)(a-w)} \left(e^{\left(-ik_{(\mathrm{c})}+k''_{(\mathrm{c})}\right)w} - \Gamma^2 e^{\left(ik_{(\mathrm{c})}-k''_{(\mathrm{c})}\right)w}\right), \tag{5.19}$$

$$M_{12} = \frac{\Gamma}{1-\Gamma^2} e^{\left(ik_{(\mathrm{a})}-k''_{(\mathrm{a})}\right)(a-w)} \left(e^{\left(ik_{(\mathrm{c})}-k''_{(\mathrm{c})}\right)w} - e^{\left(-ik_{(\mathrm{c})}+k''_{(\mathrm{c})}\right)w}\right), \tag{5.20}$$

$$M_{21} = \frac{\Gamma}{1-\Gamma^2} e^{\left(-ik_{(\mathrm{a})}+k''_{(\mathrm{a})}\right)(a-w)} \left(-e^{\left(ik_{(\mathrm{c})}-k''_{(\mathrm{c})}\right)w} + e^{\left(-ik_{(\mathrm{c})}+k''_{(\mathrm{c})}\right)w}\right), \tag{5.21}$$

$$M_{22} = \frac{1}{1-\Gamma^2} e^{\left(ik_{(\mathrm{a})}-k''_{(\mathrm{a})}\right)(a-w)} \left(e^{\left(ik_{(\mathrm{c})}-k''_{(\mathrm{c})}\right)w} - \Gamma^2 e^{\left(-ik_{(\mathrm{c})}+k''_{(\mathrm{c})}\right)w}\right). \tag{5.22}$$

The expressions above allow us to find the matrix elements of the overall transfer matrix of the magnonic crystal $\boldsymbol{M_\mathrm{T}}$ and to obtain the corresponding scattering parameters.

Figure 5.3 compares the transmission through a magnonic crystal and an unstructured waveguide, calculated using the transfer matrix method. The dips apparent in the transmission curve of the magnonic crystals are bandgaps. Notice that the bandgap depth varies periodically as k increases and that the 9^{th} bandgap is shallower than its neighbours. To understand this behaviour, it is helpful to simplify the model and assume that we have a lossless medium, i.e. $k''_{(a)}$ and $k''_{(c)}$ are zero. The transfer matrix for a unit cell in the lossless limit is

$$\boldsymbol{M} = \frac{1}{1-\Gamma^2} \begin{pmatrix} e^{-ik_{(\mathrm{a})}(a-w)}\left(e^{-ik_{(\mathrm{c})}w} - \Gamma^2 e^{ik_{(\mathrm{c})}w}\right) & 2i\Gamma\sin\left(k_{(\mathrm{c})}w\right)e^{ik_{(\mathrm{a})}(a-w)} \\ -2i\Gamma\sin\left(k_{(\mathrm{c})}w\right)e^{-ik_{(\mathrm{a})}(a-w)} & e^{ik_{(\mathrm{a})}(a-w)}\left(e^{ik_{(\mathrm{c})}w} - \Gamma^2 e^{-ik_{(\mathrm{c})}w}\right) \end{pmatrix}. \tag{5.23}$$

The system of eq. (5.23) satisfies the conservation of energy criteria. From the previous discussion, the condition for bound states is $|\mathrm{Tr}(\boldsymbol{M})| > 2$. Furthermore, we notice that the diagonal elements of $\boldsymbol{M}$, i.e. M_{11} and M_{22}, are conjugates of one another. As a result, the condition for bound states or bandgaps becomes $|\mathrm{Re}[M_{11}]| > 1$. Letting $\phi = k_{(\mathrm{a})}(a-w) + k_{(\mathrm{c})}w$, i.e. the phase accumulated by the magnons as they traverse a unit cell, the bandgap condition becomes

$$|\mathrm{Re}[M_{11}]| > 1, \tag{5.24}$$

$$\left|\cos(\phi) - \Gamma^2\cos\left(\phi + 2k_{(\mathrm{c})}w\right)\right| > |1-\Gamma^2|. \tag{5.25}$$

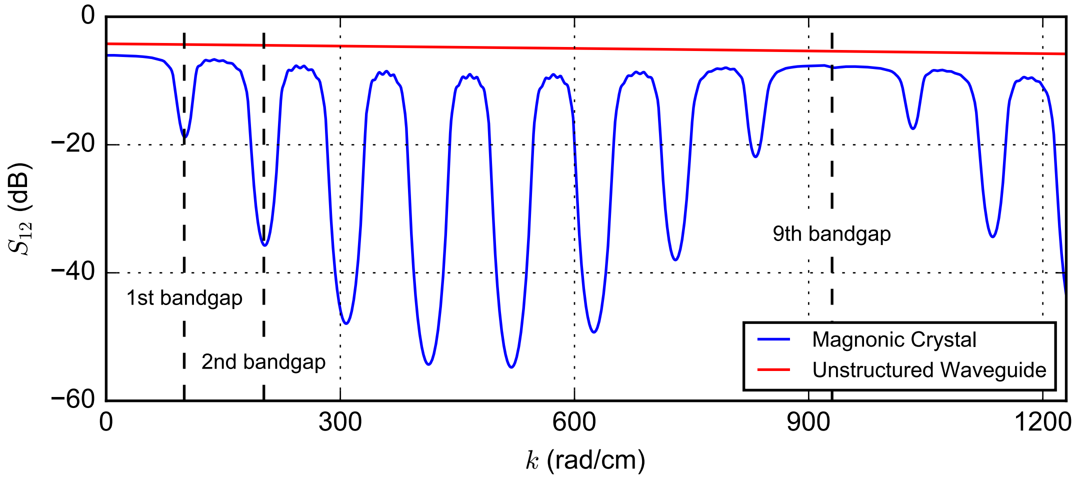

Figure 5.3: Predicted transmission (S_{21}) through a magnonic crystal ($D = 5.19\,\mu\text{m}$, $a = 300\,\mu\text{m}$, $w = 30\,\mu\text{m}$, $d = 0.5\,\mu\text{m}$, $\eta = 8$, $\zeta = 30$, $\Delta H = 0.05\,\text{Oe}$, $B = 100\,\text{mT}$) and an unstructured waveguide ($D = 5.19\,\mu\text{m}$, $\Delta H = 0.5\,\text{Oe}$, $B = 100\,\text{mT}$). Both are calculated for magnons in the BVMSW configuration.

Magnons with wavevectors ($k_{(\text{a})}$, $k_{(\text{c})}$) that satisfy eq. (5.25) are located within the bandgaps. We can define equivalent Bragg points as $\phi_n = n\pi$ ($n \in \mathbb{N}$, denotes the order of the bandgap), therefore:

$$k_{(\text{a}),n}(a - w) + k_{(\text{c}),n}w = n\pi, \tag{5.26}$$

$$k_{(\text{a}),n}\left[(a - w) + w\frac{D}{D - d}\right] = n\pi. \tag{5.27}$$

The corresponding Bragg wavevectors ($k_{(\text{a}),n}$, $k_{(\text{c}),n}$) identify the approximate position of the bandgaps. Intuitively, when the phase accumulated across a unit cell ϕ is a multiple of π, there is constructive interference between the reflected waves and destructive interference between the transmitted waves within the crystal.

However, when $\phi_n = n\pi$ and $k_{(\text{c}),n}w = m\pi$ (where $m \in \mathbb{N}$) are simultaneously satisfied, the bandgap condition (eq. (5.25)) is not met since

$$\left|\cos(\phi_n) - \Gamma^2 \cos\left(\phi_n + 2k_{(\text{c}),n}w\right)\right| = |1 - \Gamma^2|. \tag{5.28}$$

When the phase accumulated by the magnons across the etched section ($k_{(\text{c})}w$) is a multiple of π, magnons reflected from the etched to the un-etched interface interfere destructively with magnons reflected from the un-etched to the etched interface. In fig. 5.3, this occurs around the 9^{th} bandgap. When $k_{(\text{c}),n}w = m\pi/2$ (where $m \in \mathbb{N}$),

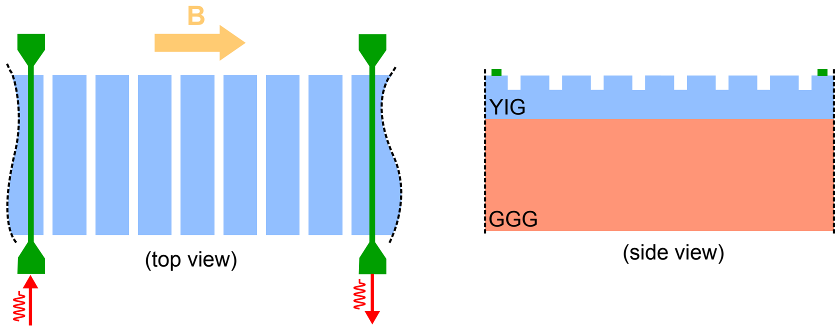

Figure 5.4: Illustration of a magnonic crystal with two microwave antennae on its surface. In our experiments, the magnetic bias field is applied in plane and parallel to the waveguide axis. (the relative size is not shown to scale).

there is a full constructive interference of magnons reflected from both interfaces, giving rise to strong rejection. For $k_{(c),n}w \neq m\pi/2$, the rejection is weaker. It is for this reason that the bandgap depths vary as k increases as shown in fig. 5.3.

5.3 Room-temperature characterisation

In this section, we consider the transmission characteristics of two magnonic crystal samples measured at room temperature and explain the reasons behind our choice of field configuration and sample in our low-temperature experiment.

Both samples are thickness-modulated YIG waveguides (unstructured thickness $D = 5.19\,\mu\text{m}$) epitaxially grown on a GGG substrate (details are summarised in table 5.1). They consist of a series of eight equally-spaced grooves with a groove depth of $d = 0.5\,\mu\text{m}$. The distance between grooves is $a = 300\,\mu\text{m}$. In the first sample (MC1), the width of the groove is $w_1 = 40\,\mu\text{m}$ and in the second (MC2) it is $w_2 = 150\,\mu\text{m}$. Magnons are excited and detected by 25 µm-wide niobium microstrip antennae fabricated 2.66 mm apart on a sapphire crystal substrate in direct contact with the magnonic crystal. This measurement configuration is illustrated in fig. 5.4.

All measurement results at room temperature are made using a network analyzer with a constant biasing field B, while sweeping the frequency of the input microwave signals f.

sample's name	MC1	MC2
inter-groove spacing (a)	300 µm	300 µm
groove's width (w)	40 µm	150 µm
groove's depth (d)	0.5 µm	0.5 µm
film's thickness (D)	5.19 µm	5.19 µm

Table 5.1: Magnonic-crystal sample specifications.

5.3.1 Choice of field configuration

To ensure compatibility with the thin-film superconducting measurement structures, the required bias magnetic field is applied in-plane, parallel to the film. We chose to carry out our experiments in the backward volume magnetostatic spin-wave geometry (BVMSW) (bias field parallel to the magnon propagation direction ($\mathbf{k} \parallel \mathbf{B}$), along the longitudinal axis of the waveguide).

Crystals measured in the backward volume configuration have been shown to display bandgaps with a higher rejection ratio (600 times larger) than in the magnetostatic surface spin-wave geometry (MSSW) ($\mathbf{k} \perp \mathbf{B}$, in-plane field) [135]. This enhanced rejection is attributed to the ability of the lowest thickness BVMSW mode to scatter into higher order thickness BVMSW modes and the fact that the MSSW mode is non-reciprocal.

Figure 5.5(a) and (b) show the transmission characteristics for MC1 (see table 5.1 for the crystal parameters) measured in both the BVMSW and MSSW configurations. The data is relative to the measured transmission at zero field, i.e. when there are no magnons excited within the film and only directly-coupled electromagnetic signals propagate between the input and output antennae in free space. Compared to the BVMSW result, the bandgaps are hardly visible in the MSSW configuration.

For the BVMSW, the uniform precession mode ($k = 0$) corresponds to the highest frequency at which the magnon signal can be observed. Propagating modes ($k \neq 0$) have lower frequencies. For the MSSW data, the uniform precession mode has the lowest frequency and propagating modes have higher frequencies. This is in accordance with the discussion in Section 2.6.4.

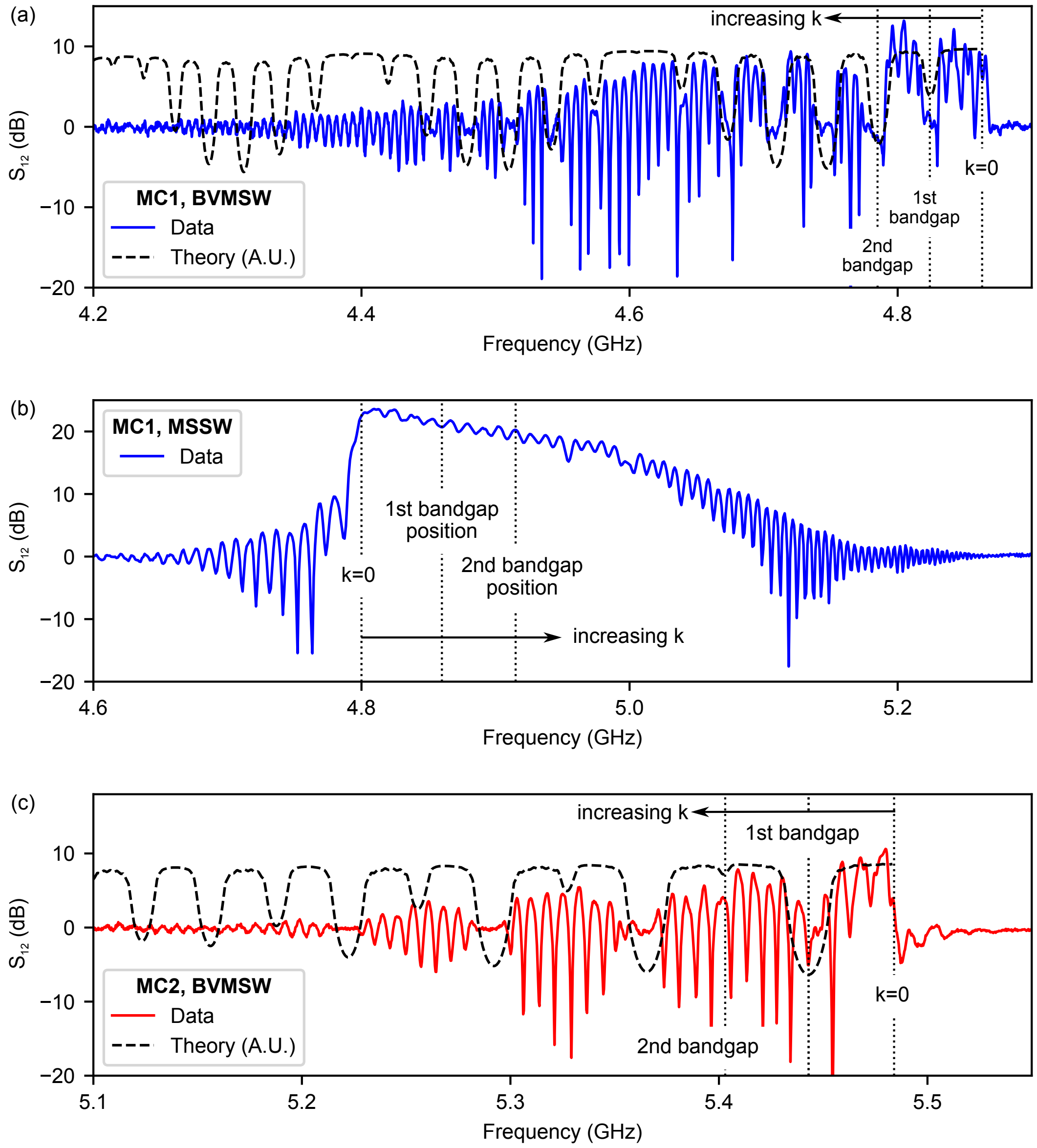

Figure 5.5: Continuous-wave transmission characteristics of magnonic crystals at room temperature. (a) Sample MC1, BVMSW, $B = 107\,\mathrm{mT}$. (b) Sample MC1, MSSW, $B = 105\,\mathrm{mT}$. (c) Sample MC2, BVMSW, $B = 127\,\mathrm{mT}$. The predicted transmission characteristics are calculated using the transfer matrix method with $M_\mathrm{s} = 139\,\mathrm{kA/m}$, $\Delta H = 0.5\,\mathrm{Oe}$, $\eta = 8$, $\zeta = 0$. The theoretical plots do not take into account the k-dependent coupling to the antennae. Note that the horizontal and vertical scales are different for the three plots.

For propagating modes, there are oscillations in the data which are caused by the interference between the magnon signal and the directly-coupled signal. Specifically, as the dispersion relations of the superposed magnonic and photonic waves are different, these signals accumulate different phases when travelling to the output antenna, resulting in interference fringes. The magnonic bandgaps of the crystal appear as gaps in this pattern. In the bandgap regions, the transmitted spin-wave signal is suppressed while the directly-coupled signal is unaffected. As a result, no oscillations are observed in this region.

It should be noted that high-k excitations couple less well than low-k ones to the antenna structures and the coupling becomes negligible once the wavelength is smaller than the antenna width [35]. It is for this reason that the observed signal strength decreases at high-k as shown in fig. 5.5.

5.3.2 Choice of samples

Figures 5.5(a) and 5.5(c) compare the measured characteristics of both samples in the BVMSW configuration with theoretical prediction made by the transfer matrix method. The theory (dotted lines) is consistent with the observed positions and widths of the bandgaps. In our calculations ζ is set to zero and η is adjusted to fit the measured widths of the gaps.

Notice that the even-order bandgaps for the MC2 sample (fig. 5.5(c)) appears relatively weak compared to those of odd order. This is a manifestation of the behaviour discussed in the previous section: magnons reflected from the etched-unetched boundary interfere destructively with those reflected from the unetched-etched boundary when the phase acquired from propagating across the etched groove is a multiple of π, i.e. $k_{(c),n}w = m\pi$ $(m \in \mathbb{N})$. For a smaller groove width w, this happens at much higher k-values as shown by the MC1 BVMSW data in fig. 5.5(a).

As we shall discover later, the damping in the magnonic crystal becomes higher at low temperature. To maximise our chances of getting measurable transmission signals at low temperature, we chose to use the magnonic crystal sample with the best room-temperature damping properties. From the data in fig. 5.5, MC1

($w_1 = 40\,\mu\mathrm{m}$) is the obvious choice. It should be noted that the higher damping in MC2 is also in accordance with our damping model that attributes a larger damping for a magnonic crystal with larger groove width.

5.4 Experiments at 20 mK

Here, we shall present results relating to both continuous and pulsed excitations of a magnonic crystal at 20 mK. In contrast to the room-temperature measurements shown in the previous section, all measurement results at 20 mK are obtained with a fixed-frequency microwave signals while sweeping the magnitude of the bias field B.

5.4.1 Continuous excitation

Figure 5.6 compares the transmission characteristics of an unstructured magnonic waveguide (11 µm film thickness, 1 mm inter-antennae spacing) and the magnonic crystal MC1, both under continuous-wave excitation at 20 mK. An offset has been applied to the data to shift the baseline to 0 dB.

The system is excited using a fixed-frequency microwave tone at 4 GHz with a power of ~ -70 dBm at the input of the antenna. The lowest field at which the backward volume magnons are observed corresponds to the uniform precession mode ($k = 0$). Signals at higher fields are propagating modes ($k \neq 0$).

At 20 mK, the measurement of the unstructured waveguide (fig. 5.6(a)) shows oscillations across the magnon band that decay in amplitude as k increases (i.e. as B increases). As described previously, these oscillations are caused by interference between the magnon and directly-coupled signals. As anticipated, no magnonic bandgap is present in the transmission characteristic of the unstructured waveguide. In the case of magnonic crystal measurement (fig. 5.6(b)), a single bandgap is observed. Its position at $B \sim 66.2$ mT is in agreement with the value predicted using the transfer matrix method ($M_\mathrm{s} = 197\,\mathrm{kA/m}$ [142, 143]).

It should be noted that in the transfer matrix method, the position and the width of the bandgaps are not significantly affected by changing the parameter ΔH. For this reason, the low-temperature calculation shown in fig. 5.6(b) uses

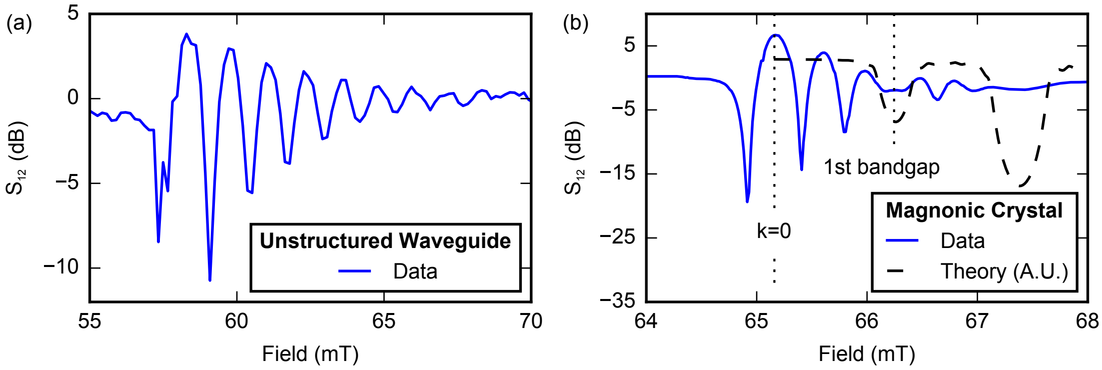

Figure 5.6: Continuous-wave transmission measurements at 20 mK corresponding to: (a) an unstructured YIG waveguide (11 µm-thickness, 1 mm antenna separation), (b) a magnonic crystal (sample MC1, 5.19 µm-thickness, 2.66 mm antenna separation). Both data sets are obtained in the BVMSW configuration with a fixed input frequency of 4 GHz. An offset has been applied to the data to shift the baseline to 0 dB. The theoretical curve plotted in panel (b) is calculated using the transfer matrix method with $M_s = 197\,\mathrm{kA/m}$, $\eta = 8$, $\zeta = 0$, $\Delta H = 0.5\,\mathrm{Oe}$.

the room-temperature value of this parameter. However, this does not imply that the actual low-temperature value of ΔH in the sample is the same as the room-temperature value. Here, our theoretical model is used solely a tool to identify the position and width of the bandgaps

The maximum k-values at which magnon signals are still measurable is found to be much smaller at low temperature than at room temperature ($\sim 168\,\mathrm{rad/cm}$ at 20 mK versus $\sim 1060\,\mathrm{rad/cm}$ at room temperature), indicating a higher damping in the former case. The effect of higher damping on the measured signal is more severe at higher k (higher field in fig. 5.6(b), lower frequency fig. 5.5(a)). This is due to the fact that the magnitude of the BVMSW group velocity decreases with increasing wavenumber. Accordingly, excitations with higher k take longer to traverse the waveguide and are therefore more severely damped [135]. In our 20 mK experiments, the magnon signal at the k-value corresponding to the second bandgap is too weak to be detected.

5.4.2 Pulsed excitation

The presence of a magnonic bandgap can also be observed in time-resolved measurements at 20 mK. When working with pulsed dipolar magnons excited in waveguides via microwave antennae, it is typically possible to achieve full temporal separation between the magnon signals and the electromagnetic signal that arises from direct coupling between the input and output antennae. This is because magnons propagate more slowly than the directly-coupled signal, which travels at c. Therefore, for sufficiently short excitation pulses, the two signals can be separated in time. However, to successfully measure a bandgap in a magnonic crystal, it is essential to ensure that the pulses are not so short such that their frequency bandwidth become larger than the width of the bandgap. In such a case, the gap cannot be observed since the microwave pulse, regardless of centre frequency, will always have some frequency components away from the bandgap that can propagate freely through the magnonic crystal.

Figure 5.7 shows the time responses of the magnonic crystal to a narrow Gaussian pulse (panel (a), halfwidth $\sigma = 3\,\text{ns}$) and a wide Gaussian pulse (panel (b), halfwidth $\sigma = 30\,\text{ns}$), both with a carrier frequency of 4 GHz. For the short Gaussian pulse, the directly-coupled signal ($5\,\text{ns} < t < 15\,\text{ns}$) and the magnon signal ($\sim 30\,\text{ns} < t < \sim 100\,\text{ns}$) are well separated in time. However, in this case, there is also no observable gap in the magnon signal (as shown by the linecuts in fig. 5.7(a)) since the spectral width of the short Gaussian pulse (∼165 MHz) is wider than the magnonic bandgap (which is estimated to be ∼ 15 MHz).

The response of the crystal to the wider Gaussian pulse is very different (fig. 5.7(b)). A Gaussian pulse with $\sigma = 30\,\text{ns}$ (spectral width ∼ 17 MHz) is slightly too long to allow for complete separation between the directly-coupled signal and the magnon signal. However, it nonetheless allows us to make a convincing observation of the bandgap. Initially, only the directly-coupled signal is observed ($\sim 40\,\text{ns} < t < \sim 100\,\text{ns}$). When the magnons start to arrive at the output antenna ($\sim 100\,\text{ns} < t < \sim 160\,\text{ns}$), they overlap in time with the directly-coupled signals, interfering destructively at the positions marked 'X' in fig. 5.7(b). Beyond 160 ns, the directly-coupled signal completely disappears and the transmitted magnon signal alone is observed. Linecuts through the data at $t = 160\,\text{ns}$ and $t = 200\,\text{ns}$ (lower panel of fig. 5.7(b)) clearly show the first bandgap of the magnonic crystal

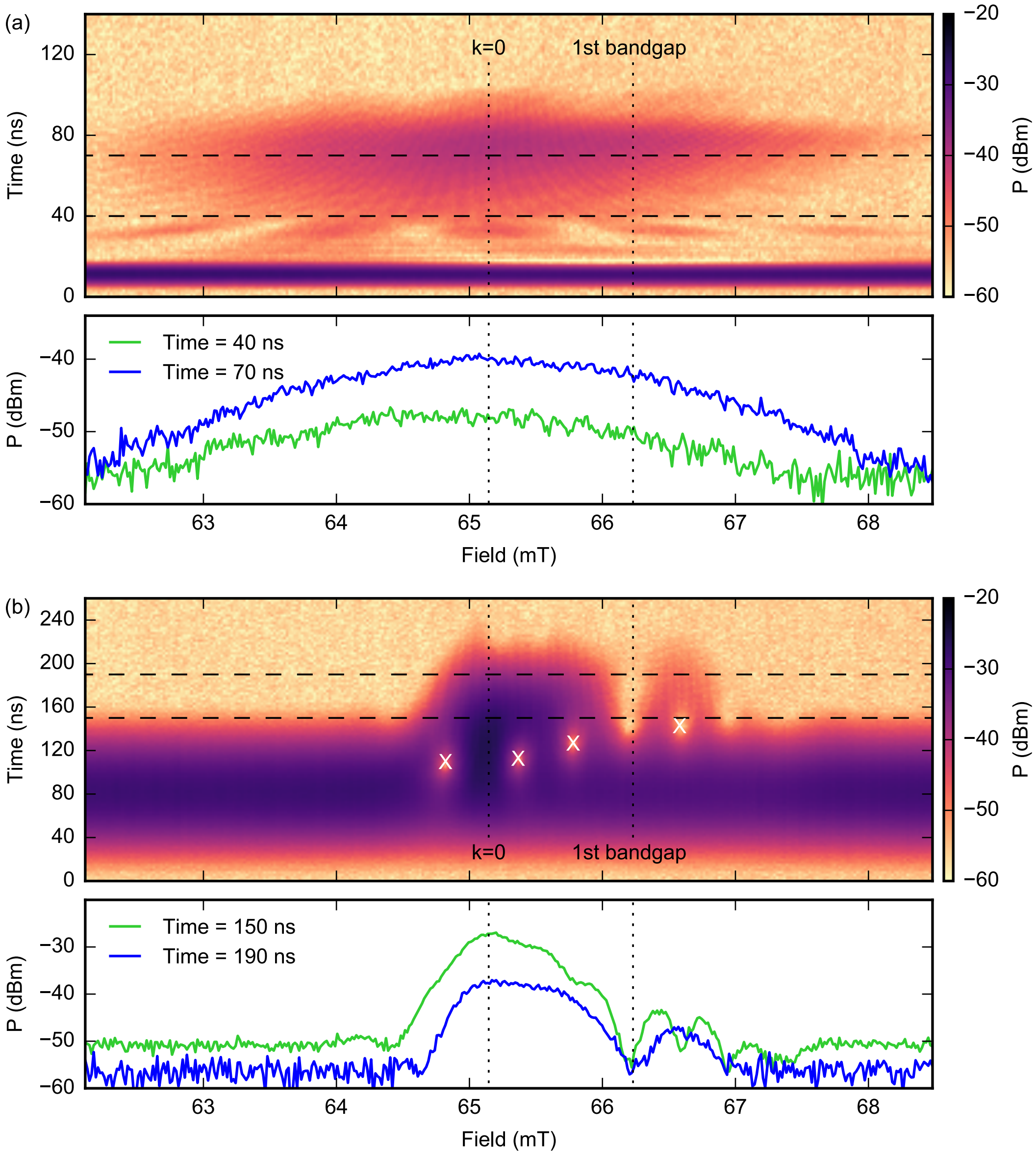

Figure 5.7: Time-resolved measurements of pulsed BVMSW signals through a magnonic crystal at 20 mK using: (a) a narrow Gaussian pulse (halfwidth or $\sigma = 3\,\text{ns}$), and (b) a wide Gaussian pulse ($\sigma = 30\,\text{ns}$). The carrier frequency of the pulse is fixed at 4 GHz. The markers 'X' indicate where the magnon and the direcly-coupled signals interfere destructively. The bandgap is not visible in panel (a) due to the wide spectral width of the Gaussian pulse. Note that the colourbar is logarithmic.

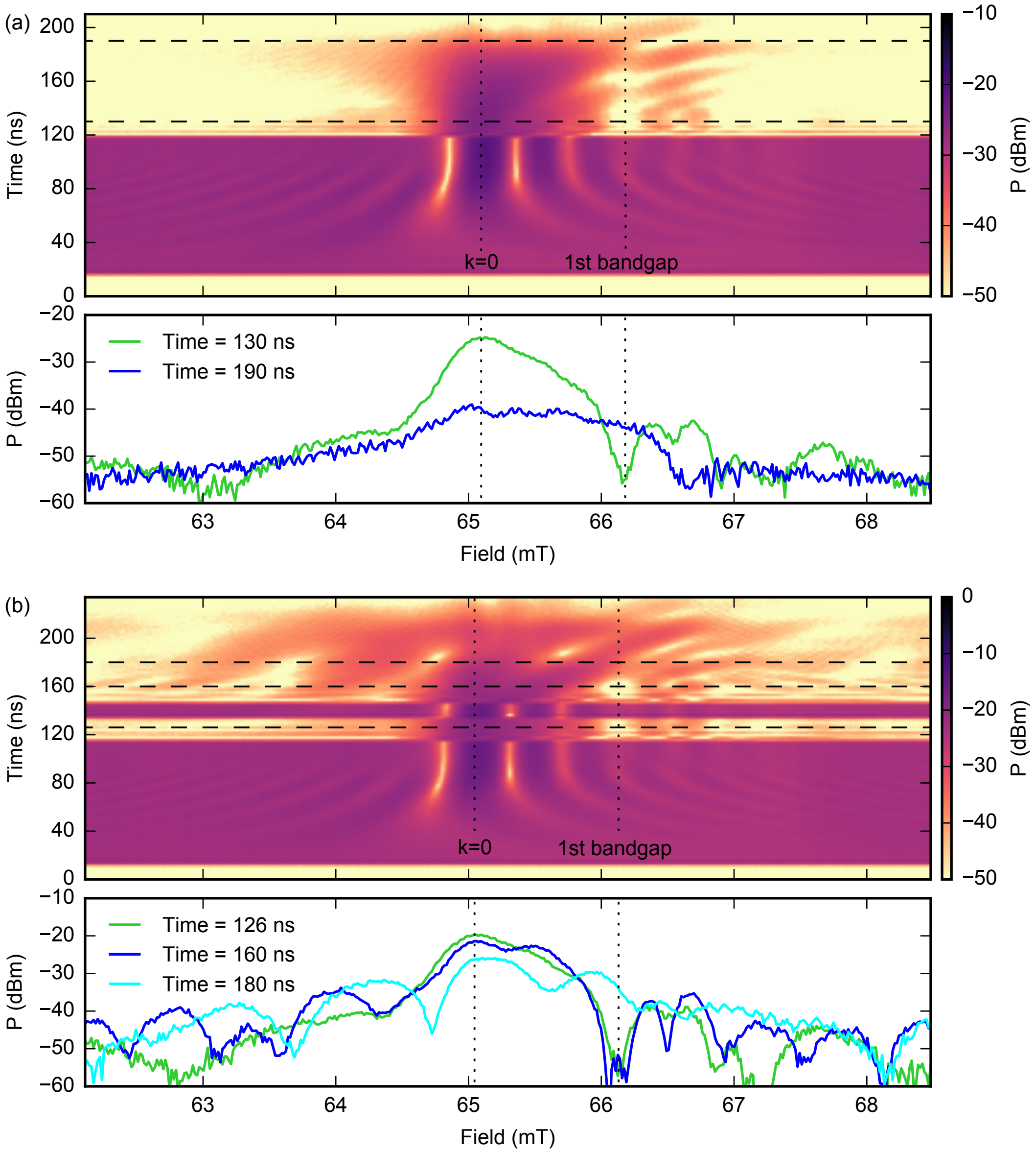

Figure 5.8: Time-resolved measurements of pulsed BVMSW signals through a magnonic crystal at 20 mK using: (a) a 100 ns-wide square pulse (directly-coupled signals at ~ 20 ns $< t < \sim 100$ ns), and (b) 100 ns-wide square pulse (~ 15 ns $< t < \sim 115$ ns) followed 20 ns later by a 10 ns-wide square pulse (~ 135 ns $< t < \sim 145$ ns). Note that the colourbar is logarithmic.

at 66.2 mT, a result which is consistent with the continuous-wave measurement data, displayed in fig. 5.6(b).

Figure 5.8(a) shows the response of the magnonic crystal to a 100 ns-wide square pulse. Here, as in fig. 5.7(b), there is an overlap between the directly-coupled and the magnon signals. Due to the sharp edges of the square pulse, the distinction between the two signals is much clearer than the results from the Gaussian excitation (which always has non-zero tail amplitude). After the directly-coupled signal ends, the bandgap is visible in the magnon signal (see the linecut at $t = 130\,\mathrm{ns}$ in the lower panel). However, in contrast with the data of fig. 5.7(b), the bandgap disappears toward the end of the magnon signal (see the linecut at $t = 190\,\mathrm{ns}$), which is different from what is observed in fig. 5.7(b). This feature can be attributed to the sharp edge of the square pulse — the typical rise time of which is $\sim 2\,\mathrm{ns}$ — whose associated wide spectral width obscures the bandgap.

Figure 5.8(b) shows the response of the magnonic crystal to wide square pulse followed 20 ns later by a narrow square pulse. As in the data of fig. 5.7(b), the bandgap is clear initially but quickly obscured due to the sharp edges of the square pulses.

5.5 Increased damping at low temperatures

A comparison between the room-temperature (fig. 5.5(a)) and the 20 mK data (fig. 5.6(b)) indicates the presence of a significant increase in the magnon damping at millikelvin temperatures. This potentially heralds a complication for YIG-based magnonic crystals at low temperature.

When considering the origin of this additional loss, there are four possible sources that warrant discussion: rare-earth magnetic impurities in the YIG, ensembles of the two-level-system-type impurities, scattering processes associated with uneven etching of the grooves, and the GGG substrate upon which the YIG film is grown.

Previous measurements [143–146] have shown that the linewidth of the uniform precession mode in YIG initially increases as the temperature of the material is reduced below 100 K, reaches a maximum value, and then begins to reduce again back to the room-temperature values. This effect is generally attributed to the presence of rare-earth impurities in YIG with temperature-dependent relaxation times [53]. Even though these earlier works have never reached the millikelvin temperature regime (the lowest temperature attained is about 5 K), they consistently report decreasing linewidths when the temperature is reduced below 10 K. Furthermore, the linewidths of bulk YIG measured in Refs. [30] and [89] at millikelvin temperatures are similar to the values observed at room temperature. From this, we can conclude that it is feasible to produce pure YIG with a linewidth at millikelvin temperatures comparable to the room-temperature value.

Tabuchi et al. [30] have observed an additional damping mechanism in a *bulk* YIG at 20 mK that is attributed to the presence of impurities that behave as two-level systems [147]. However, due to the relatively high level of microwave drive power used in our measurements and the fact that the magnonic crystal is in direct contact with the antennae, it is possible that the such impurities do not, in fact, provide a damping channel in our system. This damping process will be discussed in more detail in Chapters 6 and 7.

The surface roughness of a ferrite material is known to influence its magnon linewidth because it enhances two-magnon processes [34]. Spencer et al. showed that better polished YIG spheres do exhibit lower linewidths across a range of temperature, from 300 K down to 5 K [144]. Rough surfaces inside the grooves which define an etched MC are also known to contribute to damping [135].

The GGG substrate upon which the YIG film is grown is paramagnetic below 70 K [148]. At a relatively high field (~ 1 T), GGG is well-known to have a frustrated spin system with an ordered antiferromagnetic state below 400 mK [149]. At low field, the material undergoes a spin-glass transition below ~ 200 mK [150]. Its behaviour in the intermediate field ranges relevant to our experiments is not well-documented. However, given these known magnetic properties and the relatively narrow linewidths measured in bulk, i.e. GGG-free YIG, at low temperature, it seems highly likely that low-temperature losses due to the GGG's magnetic system coupling to YIG are an important contributor to the increased damping we observe.

In conclusion, we have measured a bandgap in a magnonic crystal based on an etched YIG waveguide at 20 mK. The result underlines the potential of these devices in low-temperature signalling and measurement systems. However, if the full potential of YIG-based magnonic crystals is to be realised in the context of manipulating magnons at the quantum level, it is essential to gain further insight into the nature of the damping in YIG films at millikelvin temperatures. This will be our focus in the remaining chapters of this thesis.

6

Damping Processes in Bulk YIG

This chapter briefly discusses the known damping processes in bulk YIG from room temperature down to the millikelvin temperature regime. Readers in search of further insight are advised to consult Refs. [34, 53, 58, 147], around which much of the discussion here is based.

6.1 Introduction

In the early years of YIG (first synthesised in 1954), much effort was focused on understanding its damping at room temperature [151]. These studies were motivated, on the one hand, by the realisation that YIG might help further understanding of the ferromagnetic resonance phenomenon discovered a decade before [2], and on another, by curiosity about what might ultimately be the narrowest magnon linewidth that could be achieved in this remarkable new material.

By the 1990s, the dominant damping mechanisms in YIG up to the Curie temperature were thought to be mostly understood [34]. The intense experimental research into the damping mechanisms of YIG and the commercial appeal of a narrow-linewidth ferrite have also led to better mastery of the techniques required to produce high-purity YIG over the last six decades. Nowadays, it is relatively easy to purchase commercially-produced bulk YIG with a MHz-linewidth at room temperature.

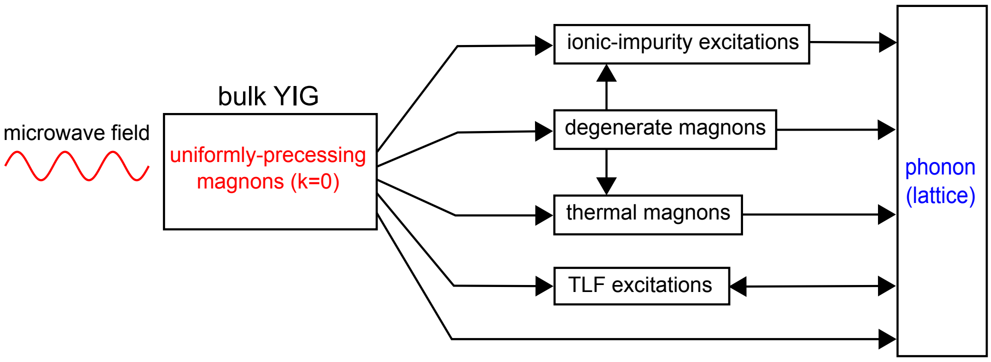

Figure 6.1: Known relaxation paths for uniformly precessing microwave magnons ($k = 0$ mode) in *bulk YIG*, from millikelvin to room temperature. Diagram is inspired by fig. 2.14 in Ref. [53].

With increasing interests in recent years in the study of microwave magnons at mK temperatures [30, 31, 71, 89, 128, 142], an understanding of the very low-temperature properties of YIG has emerged as a new priority. As will be discussed in this chapter and the next, damping mechanisms in YIG at mK temperatures are more complicated than at room temperature. In this chapter, we shall focus on the known damping mechanisms in *bulk* YIG from room temperature down to the mK temperature regime. Chapter 7 will build on this insight to develop an understanding of damping mechanism in YIG *films* below 9 K.

6.2 Overview of damping processes

In the following, we shall focus on the damping of uniformly precessing magnons ($k = 0$) excited by a low-power external microwave field. Figure 6.1 shows the known relaxation paths for uniformly precessing magnons in bulk YIG.

Thermal magnons are those excited by thermal fluctuations within the system. Relaxation involving thermal magnons can occur through a number of mechanisms such as scattering with optical phonons or magnons (notably through the Kasuya-LeCraw processes [152] and Kolokolov-L'vov-Cherepanov process [58, 153]), and inherent spin-spin processes [34]. These processes become weaker as the temperature is lowered. Degenerate magnons are thermal magnons that have the same energy as the precessional mode but possess nonzero k-values. A two-magnon process can relax a $k = 0$ magnon to a degenerate magnon [34, 53]. Such interactions can be the dominant damping process across the whole temperature range. Magnon relaxation through ionic impurities occur through so-called temperature-peak processes [34, 53]. These typically dominate in the temperature range between $\sim 1\,\mathrm{K}$ and $\sim 150\,\mathrm{K}$. Relaxation involving two-level fluctuators (TLFs) only dominates for temperatures below $1\,\mathrm{K}$ [30, 147].

After the initial relaxation event, thermal magnons can further relax through mixing with other thermal magnons (via three-magnon, four-magnon processes, etc.), through temperature-peak processes to ionic impurity excitations, or directly to the lattice [53]. Ionic impurity excitations relax exclusively to the lattice [34]. In principle, TLFs can also relax by interacting with other excitations within the system. However, as the origin of TLFs in the YIG system is unclear, it is perhaps premature to speculate about this mechanism, and therefore we add just one extra line connecting TLFs with phonons [147].

Direct relaxation to the lattice is caused by the magnetoelastic interaction; in the low-k regime, this is known to be much weaker than the other processes discussed above [34]. As such, it is seldom considered to be the dominant relaxation mechanism for $k = 0$ magnons. However, this interaction may still play an important role in relaxing high-k thermal magnons generated during subsequent relaxation events.

6.3 Scattering with optical phonons or magnons

Damping in pure YIG is known to have a linear frequency dependence at room temperature [57]; its magnitude decreases as the temperature is reduced from room temperature to about $\sim 150\,\mathrm{K}$ [154]. There are two competing theories used to describe this behaviour: the Kasuya-LeCraw mechanism and the Kolokolov-L'vov-Cherepanov mechanism.

In the Kasuya-LeCraw theory, there are two processes through which the $k = 0$ magnons can relax [53, 152]. Both of these are caused by the modulation of the local uniaxial anisotropy by a phonon [58]. The first process involves the confluence of a $k = 0$ magnon with an optical phonon to form a thermal magnon in the lowest branch of the magnon spectrum (referred to as the ferromagnon branch in Ref. [58]). This mechanism reproduces the observed linear frequency and temperature dependences of the damping between $\sim 150\,\mathrm{K}$ and $350\,\mathrm{K}$; the predicted temperature dependence is shown to drop below linearity as the temperature is reduced below $150\,\mathrm{K}$ [53]. The analytical derivation for the linewidth contribution from the first Kasuya-LeCraw process is described in Ref. [53], it can be expressed as:

$$\Delta H_{\mathrm{KL}} = \left(C_{\mathrm{KL}} F(T)\right) \omega \tag{6.1}$$

where

$$F(T) = \frac{(\hbar\omega_{q2})^2}{k_{\mathrm{B}}^2 T} \exp\left(\frac{\hbar\omega_{q2}}{k_{\mathrm{B}}T}\right) \left[\exp\left(\frac{\hbar\omega_{q2}}{k_{\mathrm{B}}T}\right) - 1\right]^{-2} . \tag{6.2}$$

Here, C_{KL} is a constant related to the interaction strength and phonon properties, ω_{q2} is the phonon frequency, and ω is the magnon frequency.

The second Kasuya-LeCraw process involves the confluence of a $k = 0$ magnon with a thermal magnon to form another thermal magnon in the ferromagnon branch. This mechanism predicts a damping that is linear in frequency and quadratic in temperature [152]. The latter suggests that this process dominates at high temperatures ($T > 350\,\mathrm{K}$) where the observed temperature dependence is indeed above a linear behaviour [53].

A little less than three decades after the Kasuya-LeCraw theory was published, a new theory by Kolokolov, L'vov, and Cherepanov [153] pointed out that the quadratic dispersion relation assumed in the Kasuya-LeCraw theory is incorrect. As a result, they suggested that the linewidth contribution was overestimated by one order of magnitude. The Kolokolov-L'vov-Cherepanov theory proposed an alternative relaxation process involving the confluence of a $k = 0$ magnon with an optical magnon to produce another optical magnon; an interaction produced by the uniaxial crystallographic anisotropy of the Fe^{3+} ions in the octahedral sites. The authors claim that this mechanism can reproduce a substantial contribution to the

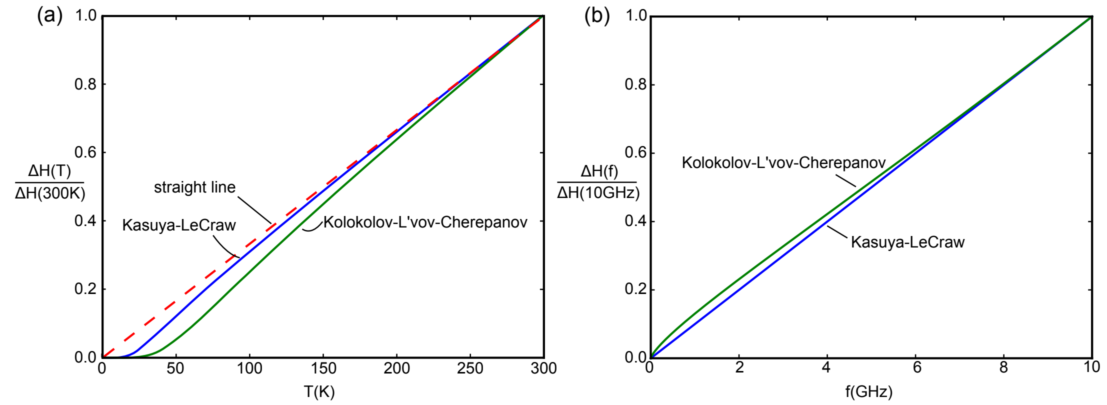

Figure 6.2: Temperature- and frequency- dependent behaviour of the linewidth contribution due to the first Kasuya-LeCraw ($\hbar\omega_{q2}/k_\mathrm{B} = 100\,\mathrm{K}$ [53]) and Kolokolov-L'vov-Cherepanov ($\Omega = 200\,\mathrm{K}$ [153]) processes. The displayed linewidths are relative to the value at $T = 300\,\mathrm{K}$ for panel (a) and its value at $f = 10\,\mathrm{GHz}$ for panel (b).

$k = 0$ magnon linewidth at room temperature. The Kolokolov-L'vov-Cherepanov linewidth can be expressed as [58, 153]:

$$\Delta H_{KLC} \approx C_\mathrm{KLC}\left(13.52(\omega)^{3/4} + 1.15(\omega)^{3/2}\right) G(T) \tag{6.3}$$

where

$$G(T) = \frac{\exp\left(\Omega/T\right)}{T(\exp\left(\Omega/T\right) - 1)^2}. \tag{6.4}$$

Here, C_KLC is a constant related to the properties of the YIG's magnon spectrum and the interaction strength. The parameter Ω is determined by the gap in the optical magnon spectrum. Figure 6.2 shows the temperature- and frequency-dependence of the linewidth contributions due to the first Kasuya-LeCraw and the Kolokolov-L'vov-Cherepanov processes.

6.4 Two-magnon process

The term 'two-magnon process' usually refers to a relaxation process where a uniformly precessing magnon ($k = 0$) is annihilated and a degenerate magnon ($k \neq 0$) is created [34, 53]. Such processes are forbidden in an ideal crystal because they do not conserve momentum. However, if there are non-uniformities within the crystal, this can provide the extra momentum contribution required to activate the process. Examples of possible non-uniformities include: disorder in the ionic distribution in the lattice [155], variation in the direction of the crystal axes [156], and geometrical non-uniformities such as pores and surface roughness [144, 157, 158].

As a rule of thumb, two-magnon processes in high quality YIG crystals are usually dominated by the contribution from the sample's surface roughness [34, 53]. A number of investigations at the end of the 1950s showed that the quality of the surface polish substantially influences the $k = 0$ magnon linewidth in YIG spheres [144, 157]. By modelling the surface roughness as hemispherical pits on the surface [34, 53, 158], the associated linewidth contribution can be expressed as

$$\Delta H_{2\mathrm{m}} = C_{2\mathrm{m}} \frac{R_\mathrm{s}}{R_0} M_\mathrm{s} \tag{6.5}$$

where $C_{2\mathrm{m}}$ is a constant related to the scattering properties of the pits and the density of states available for the relaxation process, R_s is the radius of the pit, R_0 is the radius of the sphere, and M_s is the saturation magnetisation. The expression shows that the linewidth contribution increases as the ratio of the pit size to the sample size is increased. Because the presence of a thermal magnon is not required to induce two-magnon processes (in contrast to contributions from the Kasuya-LeCraw and the Kolokolov-L'vov-Cherepanov processes), their contribution to the damping does not decrease with decreasing temperature. The only temperature dependence in the two-magnon case comes from the saturation magnetisation (M_s), which increases as the temperature is decreased [143, 159].

In some cases, namely those in which the YIG has a very rough surface, two-magnon process can dominate over the Kasuya-LeCraw and the Kolokolov-L'vov-Cherepanov mechanisms in relaxing the $k = 0$ magnons. It has been reported that the linewidth of a YIG sphere can be as low as ~0.5 Oe if it is well polished and as high as ~ 10 Oe when polished with a 35 μm grit size polishing paper [157]. Reference [34] claims that a really well polished YIG sphere can have a linewidth as low as ~ 0.3 Oe at room temperature. For comparison, an estimation by Sparks [53] suggested that the first Kasuya-LeCraw process can contribute ~0.2 Oe (at 9 GHz frequency) to the $k = 0$ magnon linewidth in YIG at room temperature.

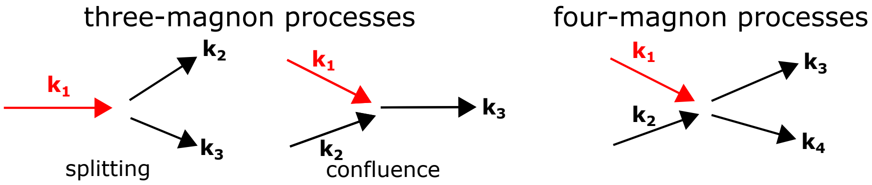

Figure 6.3: Illustration of the three-magnon and four-magnon processes.

It should also be understood that two-magnon processes contribute not only to initial scattering events but to subsequent relaxation events.

6.5 Inherent spin-spin processes

Spin-spin damping has its origin in the magnetic dipolar and exchange interactions [34, 53, 160]. Such processes lead to the redistribution of energy between magnon modes even in ideal systems without non-uniformities.

Spin-spin processes are generally classified into three-magnon and four-magnon processes, both of which are illustrated in fig. 6.3. In three-magnon processes, the number of interacting magnons is not conserved. These can only be caused by the magnetic dipolar interaction [34]. Four-magnon process, on the other hand, can be brought about by both the dipolar and exchange interactions. Usually, the probability of a relaxation process occurring is smaller, the larger the number of participating magnons. However, as a four-magnon process can be caused by both magnetic interactions, they can dominate over their three-magnon counterparts, especially at high temperature and when participating magnons have high-k values [34].

Three-magnon processes can be splitting or confluent in nature as illustrated in fig. 6.3. Both mechanisms require momentum and energy to be conserved; as a result, a three-magnon confluence process cannot relax magnons with low-k values (in particular $k = 0$) [53] while three-magnon splitting process can contribute to the relaxation of low-k magnons (including the $k = 0$) so long as the applied field is low enough [34]. Both splitting and confluence processes are active in relaxing magnons with large-k values (with no special requirement for applied field). Four-magnon processes originating from the exchange interaction can only contribute to the relaxation of $k \neq 0$ magnons. In contrast, those brought about by the dipolar interaction can cause relaxation of $k = 0$ magnons but their contribution is less significant than the other processes mentioned above [160].

Compared to relaxations through scattering with optical phonons or magnons, or through a two-magnon process, spin-spin processes play a less important role in relaxing $k = 0$ magnons. They are more dominant in subsequent relaxation events where magnons with higher k-values are involved [34].

6.6 Temperature-peak processes

The temperature dependence of the magnon linewidth of commercially-available YIG between 1 K and 150 K usually features one or more local maxima [143, 144, 146, 161–165]. Such behaviour cannot be accounted for by Kasuya-LeCraw or Kolokolov-L'vov-Cherepanov theories, spin-spin processes, or two-magnon process.

Through a number of experimental investigations, it has been shown that this peaking behaviour is caused by the presence of rare-earth ionic impurities introduced during crystal growth [34, 53, 166, 167]. A small impurity density can give rise to a large temperature-dependent linewidth. Three models have been put forward to explain this so-called *temperature-peak* behaviour: slowly relaxing impurities, the valence-exchange mechanism, and rapidly-relaxing impurities.

It should be noted that it is possible to decrease the linewidth contributions from these temperature-peak processes by further purifying the YIG as shown by Refs. [144, 165]. However, these additional steps are generally expensive and tedious. Since YIG-based devices are usually made for room-temperature applications, they are generally not part of the production process of most commercially available YIG.

6.6.1 The slowly-relaxing-impurity model

The central idea of the slowly-relaxing-impurity model is that the energy levels of each substitutional ionic impurity are modulated by the precessional motion of the magnetisation (or the Fe^{3+} ions). Under the right conditions, this leads to net energy transfer from magnons to the lattice as the impurities attempt to reach thermal equilibrium.

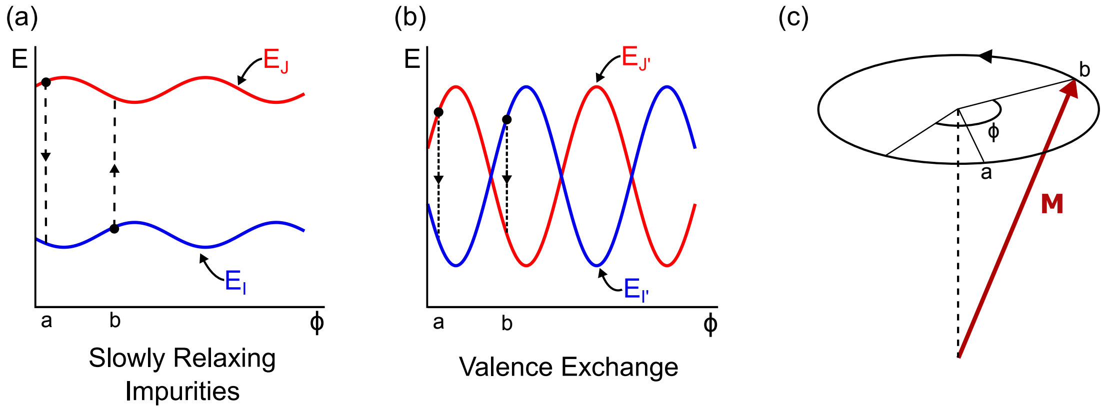

Figure 6.4: Energy variation of the two lowest ground states, I and J, of Yb^{3+} ions in the slowly-relaxing-impurity model (panel (a)) and of the extra electron in both sites I' and J' for the valence-exchange model (panel (b)) as the magnetization M precesses around its equilibrium position (panel (c)). Adapted from figs. 6.3 and 6.6 in Ref. [53].

To illustrate the process, consider the case in which some of the Y^{3+} ions in the YIG (which do not contribute to its magnetisation) are replaced by another rare-earth ion such as paramagnetic Yb^{3+}. This effectively produces a second magnetic sublattice in the crystal structure to which the original Fe^{3+} sublattice can couple via the exchange interaction. For ease of explanation, we shall use Yb^{3+} as a running example, however the same reasoning can, of course, be applied to a host of other rare-earth impurities [162, 163, 168, 169]. Like many rare-earth ions, Yb^{3+} has a low-lying doublet [34], whose degeneracy is lifted through exchange coupling to the Fe^{3+}, forming two levels, denoted as I and J [53]. As the strength of the exchange coupling depends on the relative orientation of the Fe^{3+} and Yb^{3+} sublattices, precession of the Fe^{3+} system creates a modulation of the energy spacing (δE) between the two I and J states of the Yb^{3+} as shown in fig. 6.4(a). As a result, the thermal population is redistributed between the two levels.

Around position a, $\Delta E(\mathrm{a}) = E_\mathrm{J}(\mathrm{a}) - E_\mathrm{I}(\mathrm{a})$ increases with the precession angle (ϕ) and this causes the thermal equilibrium population ratio between level J and level I, i.e. $N_\mathrm{J}/N_\mathrm{I} = \exp\left(-\Delta E/k_\mathrm{B}T\right)$, to decrease. As a result, some of the ions in level J have to transition to level I, transferring energy to the lattice in the process. At position b, $\Delta E(\mathrm{b})$ decreases with increasing ϕ, causing the thermal equilibrium population ratio $N_\mathrm{J}/N_\mathrm{I}$ to increase. Accordingly, this leads to some ions in level I to transition to level J, absorbing energy from the lattice. The competition between the rate at which thermal equilibrium is established ($1/\tau_\mathrm{r}$) and the rate at which the ionic energy level is modulated (ω) determines the net energy transferred to the lattice. When both rates are equal, i.e. $\omega\tau_\mathrm{r} \sim 1$, the energy transfer to the lattice is maximal.

The linewidth contribution from the slowly-relaxing-impurity model is [34, 170, 171]

$$\Delta H_\mathrm{SR} = \frac{1}{M_\mathrm{s}} P_1 \Omega_1 \tag{6.6}$$

where:

$$P_1 = \frac{C_\mathrm{SR}}{k_\mathrm{B}T\left(\cosh\left(\frac{\delta E}{2k_\mathrm{B}T}\right)\right)^2}, \tag{6.7}$$

$$\Omega_1 = \frac{\omega\tau_\mathrm{r}}{1+(\omega\tau_\mathrm{r})^2}. \tag{6.8}$$

C_SR is a constant that depends on the number of ionic impurities and the change in the energy spacing (δE) as the magnetisation precesses around its equilibrium position, M_S is the saturation magnetisation, ω is the precessional angular frequency, and τ_r is the relaxation time of the ionic energy levels.

Different processes contribute to the relaxation of the ionic energy level to the lattice as discussed in Refs. [34, 168, 172, 173]. At temperatures below $\sim 60\,\mathrm{K}$, relaxation is governed by the one-particle Orbach process (the so-called direct process):

$$\tau_r = \tau_{r,0} \tanh\frac{\delta E}{2k_\mathrm{B}T}. \tag{6.9}$$

The parameter $\tau_{r,0}$ in eq. (6.9) also depends on δE with the exact nature of its dependence being determined by the specific process involved [34]. At higher temperatures, relaxation is governed either by the two-quasiparticle Orbach process or the Raman process, which have different temperature dependencies [168, 172].

Note that Ω_1 is the only frequency-dependent term in eq. (6.6). It is maximum when $\omega\tau_\mathrm{r} \sim 1$ (see eq. (6.8)), a condition that corresponds to maximum energy transfer to the lattice. At a given precessional frequency ω, Ω_1 is maximum

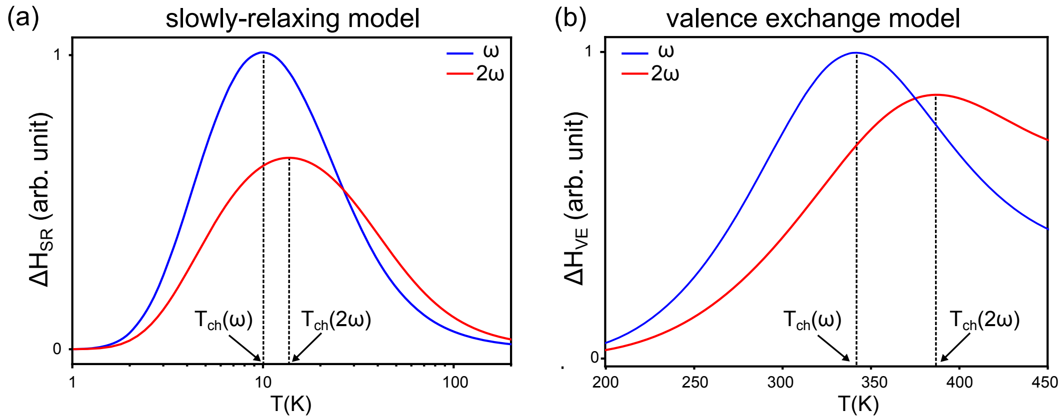

Figure 6.5: Temperature-dependent linewidth (ΔH) contribution calculated at two different magnon frequencies (ω, 2ω). (a) Slowly-relaxing-impurity model with $\delta E = 8\,\mathrm{cm}^{-1}$, $\omega\tau_{\mathrm{r},0} = 3.3$ [169]. Note that the horizontal axis is logarithmic. (b) Valence-exchange model with $\tau_{\mathrm{h},0} = 0.5 \times 10^{-13}\,\mathrm{s}$, $E_{\mathrm{b}} = 0.2\,\mathrm{eV}$ [177]. In both models, the saturation magnetisation is modelled according to Ref. [143]. Notice that the characteristic temperature T_{ch} becomes higher as ω increases.

only at a particular characteristic temperature T_{ch} as the relaxation time (τ_{r}) is temperature dependent. Also, eq. (6.9) implies that the relaxation time increases with decreasing temperature. Accordingly, the higher the precessional frequency, the higher the characteristic temperature T_{c} at which the local maxima of the linewidth also occurs, as shown in fig. 6.5(a).

6.6.2 The valence-exchange model

The valence-exchange model, also referred to as the charge-transfer model in [53] or the jumping mechanism in [34], is caused by the presence of Fe^{2+} or Fe^{4+} impurity ions within the system [34, 174, 175]. We recall that the magnetisation of a pure YIG crystal is due to Fe^{3+} ions located within its crystal structure. If a ferrous impurity is substituted, the extra electron from Fe^{2+} (or the lack of electron from Fe^{4+}) is mobile and can hop to other Fe^{3+} sites. Under the right conditions, this hopping leads to a net energy transfer from magnons to lattice. We shall use the example of the Fe^{2+} ion to demonstrate why.

Consider a case in which an extra electron, presents on account of a substitutional Fe^{2+} ion, can hop between two equivalent Fe^{3+} sites, denoted as I' and J'. The energy of the extra electron at each site depends on the relative angle between the overall magnetisation of the sample and the axis of the local ion [34]. As the magnetisation precesses (angular frequency ω) with respect to its equilibrium position (fig. 6.4(c)), the energy of sites I' and J' vary as illustrated in fig. 6.4(b). As a result, the thermal equilibrium population of ions on sites I' and J' also vary with ϕ. At position a in fig. 6.4(c), an extra electron that is at site J' (with higher energy) will attempt to hop to site I' (with lower energy), transferring $E_{\mathrm{J}'}(\mathrm{a}) - E_{\mathrm{I}'}(\mathrm{a})$ from the precessional energy to the lattice. Similarly, at position b, extra electrons at site I' will attempt to hop to site J', giving away $E_{\mathrm{I}'}(\mathrm{b}) - E_{\mathrm{J}'}(\mathrm{b})$ to the lattice. In a manner similar to the slowly-relaxing-impurity model, competition between the rate at which the thermal equilibrium is established ($1/\tau_{\mathrm{h}}$) and the rate at which the site energy varies (ω) determines the net energy transferred to the lattice per unit time. When the two rates coincide, i.e. $\omega\tau_{\mathrm{h}} \sim 1$, the energy transfer to the lattice is maximum.

The theory of the valence-exchange model was first developed by Clogston [170] and further improved by Hartwick and Smit [176]; its contribution due to the linewidth is given by [176]:

$$\Delta H_{\mathrm{VE}} = \frac{1}{M_{\mathrm{s}}} P_2 \Omega_2 \tag{6.10}$$

where

$$P_2 = \frac{C_{\mathrm{VE}}}{(k_{\mathrm{B}}T)^3}, \tag{6.11}$$

$$\Omega_2 = \frac{\omega\tau_{\mathrm{h}}}{1 + (\omega\tau_{\mathrm{h}})^2}. \tag{6.12}$$

Here, C_{VE} is a constant that depends on the number of substitutional ferrous impurities and the nature of energy level modulation, M_{s} is the saturation magnetisation, ω is the angular frequency of precession, and τ_{h} is the electron hopping time. The hopping time is determined by the energy barrier associated with the hopping process, E_{B}, according to [53, 177]:

$$\tau_{\mathrm{h}} = \tau_{\mathrm{h},0} \exp\left(\frac{E_{\mathrm{b}}}{k_{\mathrm{B}}T}\right). \tag{6.13}$$

Here, both $\tau_{\mathrm{h},0}$ and E_{b} depend on the environment of the hopping sites.

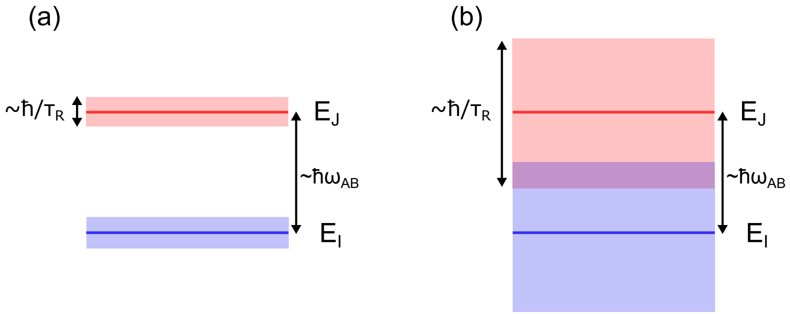

Figure 6.6: Illustration of the rapidly-relaxing-impurity model. The figure shows the two lowest ground states of the impurity ion and the corresponding energy broadening. (a) The transition probability is small because the broadening is not wide enough. (b) When the broadening is at the same order as the level separation ($\omega\tau_\mathrm{r} \sim 1$), the impurity ion can be excited by absorbing energy from the magnons. Adapted from Ref. [34].

Equation (6.10) has the same form as that which describes the slowly-relaxing-impurity model (compare eq. (6.6)) and, as in the equivalent expression, Ω_2 is the only frequency-dependent term. The magnitude of eq. (6.12) is maximum when $\omega\tau_\mathrm{h} \sim 1$. It can be seen from eq. (6.13) that the hopping time increases with decreasing temperature. As a result, the higher the precessional frequency, the higher the characteristic temperature (T_ch) at which the local maximum of the linewidth occurs, as shown in fig. 6.5(b).

Prior to 1964 [53, 178–180], the valence-exchange model was thought to be the origin of the low-temperature maxima measured in the linewidths of some ferrites. In particular, in YIG, Spencer et al. showed that by increasing the amount of substitutional Fe^{2+}, they were able to reproduce the low-temperature linewidth maximum which seemed to be strongly suggestive of the validity of the valence-exchange model [179]. However, more recently, experimental evidence has indicated that, in fact, the low-temperature maximum (at $\sim 40\,\mathrm{K}$) is caused by the slowly-relaxing-impurity mechanism mediated by Fe^{2+} ions [34, 176, 177, 181, 182]. A higher temperature linewidth maximum (370 K) was also observed and found to be explicable by the valence-exchange model [176, 177].

6.6.3 The rapidly-relaxing-impurity model

Rapidly relaxing impurities contribute to the magnon linewidth through ionic energy levels that relax on short timescales (τ_r). This relaxation process leads to broadening of the ionic energy levels as shown in fig. 6.6. When this broadening is comparable to the energy level separation ($\delta E = \hbar\omega_\mathrm{AB}$), i.e. $\omega_\mathrm{AB}\tau_\mathrm{r} \sim 1$, it can, in principle, excite an ionic impurity while absorbing energy from a magnon even though it is not resonant with the energy level spacing (usually $\hbar\omega \ll \delta E$). The excited ionic impurity then relaxes by decaying to the lattice.

Detailed derivation of the rapidly-relaxing-impurity model can be found in [53, 183–185]. Its linewidth contribution in the high-temperature limit ($\hbar\omega \ll k_\mathrm{B}T$) is [53]

$$\Delta H_\mathrm{RR} = C_\mathrm{RR}\left(\frac{\hbar\omega}{k_\mathrm{B}T}\right)(\hbar\omega_\mathrm{AB})^2\frac{\tau_\mathrm{r}}{1+(\omega_\mathrm{AB}\tau_\mathrm{r})^2} \tag{6.14}$$

where C_2 is a constant that depends on the population of the ionic impurity population and the exchange interaction strength between the ionic impurity and the Fe^{3+}. In this high-temperature limit, the linewidth scales linearly with the angular precession frequency ω. i.e. it follows the Gilbert damping model. This is not the case for the slowly-relaxing-impurity or the valence-exchange models. The term $\frac{\tau_\mathrm{r}}{1+(\omega_\mathrm{AB}\tau_\mathrm{r})^2}$ displays a maximum at a characteristic temperature that satisfies $\omega_\mathrm{AB}\tau_\mathrm{r} \sim 1$. In contrast to the slowly-relaxing-impurity ($\omega\tau_\mathrm{r} \sim 1$) and the valence-exchange ($\omega\tau_\mathrm{h} \sim 1$) mechanisms, the characteristic temperature in the rapidly-relaxing-impurity model does not depend on ω. To the best of the author's knowledge, there has never been an experimental study in which the rapidly-relaxing-impurity model has been directly observed experimentally.

6.7 Two-level fluctuators

At temperatures below 1 K (for excitations in the GHz-frequency regime), an additional contribution to the damping in bulk YIG is found to have characteristics that are consistent with the two-level fluctuator (TLF) model [30, 186]. The TLF

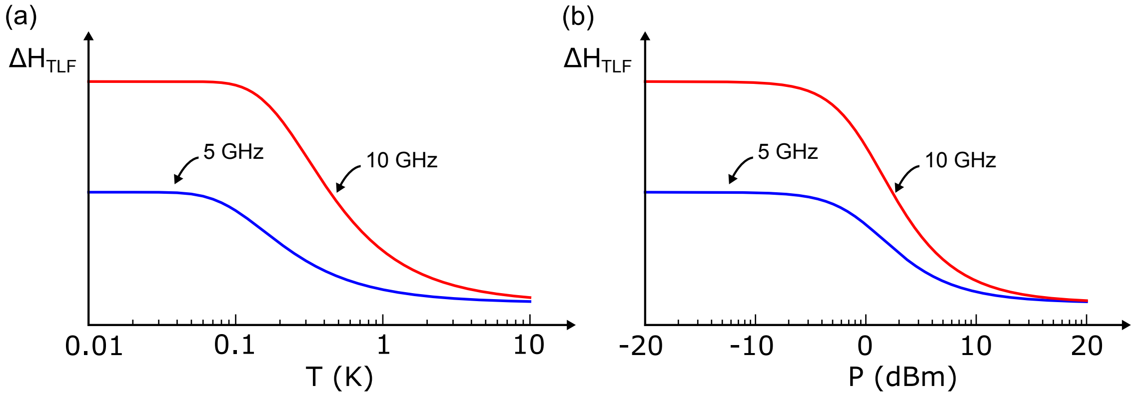

Figure 6.7: Temperature-dependent behaviour (panel(a)) and power-dependent behaviour (panel (b)) of the linewidth contribution due to TLF. Panel (a) is calculated assuming a weak external field. Panel (b) is calculated at 20 mK and 0 dBm saturation power.

model was first proposed to explain the anomalous thermal properties of vitreous silica at temperatures below 10 K [147, 187], but was later found to be a good model to explain the damping behaviour in superconducting resonators [188]. In most of the investigations to date concerning the linewidth of YIG, damping due to TLFs was not observed as the lowest temperatures were around $\sim 2\,\mathrm{K}$ and the mechanism does not become a significant contributor to the damping until the temperature is lowered below 1 K.

Conceptually, the idea underpinning the TLF model is as follows: there are impurities within the material that can be modelled as an ensemble of two-level systems (fluctuators) with a broad frequency spectrum. At high temperature ($\hbar\omega_{\mathrm{TLF}} \ll k_{\mathrm{B}}T$), these TLFs are saturated by thermal phonons and, therefore, the material behaves as if they were not present. This is the reason why damping due to TLFs has not been observed at high temperature. At low temperature ($\hbar\omega_{\mathrm{TLF}} \gg k_{\mathrm{B}}T$), there are not enough thermal phonons to saturate the TLFs. If there is no external microwave drive or the drive power is low enough ($P \ll P_{\mathrm{sat}}$), most TLFs are in their ground state and ready to absorb any resonant excitation – in our case: magnons – within the system. If we assume that the TLFs preferentially relax to the lattice, this mechanism produces an additional damping channel. At these low temperatures, it is possible to saturate the TLFs using a strong external microwave drive ($P \gg P_{\mathrm{sat}}$); when fully saturated, they are unable to absorb more excitations from within the system and, as a result, the TLF damping becomes negligible.

The loss tangent arising from TLFs can be modelled as [189]

$$\delta_{\mathrm{TLF}} = C_{\mathrm{TLF}} \frac{\tanh\left(\hbar\omega/2k_{\mathrm{B}}T\right)}{\sqrt{1+\left(P/P_{\mathrm{sat}}\right)}} \tag{6.15}$$

where C_{TLF} is a factor that depends on the density and the dipole strength of the TLF. As the loss tangent is the inverse of the quality factor, i.e. $1/Q = \Delta\omega/\omega \approx \delta_{\mathrm{TLF}}$ for $\delta_{\mathrm{TLF}} \ll 1$, then the linewidth contribution from the TLF is

$$\Delta H_{\mathrm{TLF}} = \frac{\omega}{\gamma\mu_{\circ}} \delta_{\mathrm{TLF}} \tag{6.16}$$

where γ is the gyromagnetic ratio, and $\mu_{\circ}$ is the vacuum permeability. The power ratio within the square root of eq. (6.15) can be expressed as $(P/P_{\mathrm{sat}}) = \omega_{\mathrm{TLF}}^2 \tau_1 \tau_2$ where ω_{TLF} is the Rabi frequency, τ_1 and τ_2 are respectively the longitudinal and transverse relaxation time constants of the TLFs. Figure 6.7 shows the behaviour of ΔH_{TLF} as a function of temperature (T) and power (P).

It is important to note that the TLF mechanism is just a phenomenological model. It does not propose an origin for this behaviour in the system. In other physical systems such as the vitreous silica, the TLFs are thought to consist of tunnelling states between neighbouring defect sites [147]. Each state is modelled as a particle tunnelling across a double well potential minimum. The origin of TLFs in bulk YIG is still unknown.

6.8 Summary

At this point, it is helpful to summarise the dominant relaxation processes of $k = 0$ magnons in bulk YIG from room temperature down to the mK regime. From room temperature to $\sim 100\,\mathrm{K}$ [143], the dominant damping process is either scattering with optical phonons (first Kasuya-LeCraw process, Section 6.3) or optical magnons (Kolokolov-L'vov-Cherepanov process, Section 6.3). In this temperature range, the magnon linewidth has a linear frequency dependence and decreases with temperature. Between $1\,\mathrm{K}$ and $100\,\mathrm{K}$, temperature-peak processes become

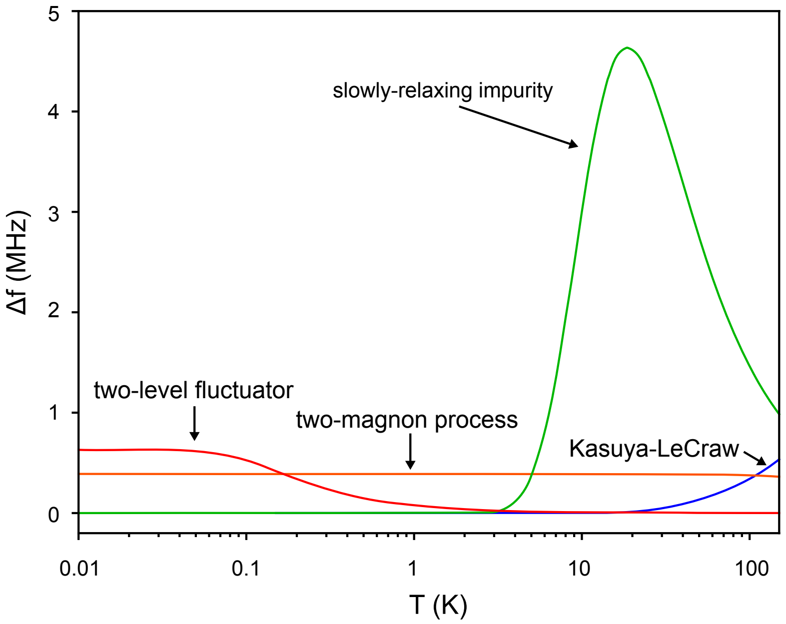

Figure 6.8: Contributions to magnon linewidth in a YIG sphere ($f = 10\,\mathrm{GHz}$). The Kasuya-LeCraw line is calculated with $\hbar\omega_{q2}/k_{\mathrm{B}} = 100\,\mathrm{K}$ and normalised to 1 MHz at 300K. The two-magnon line is calculated assuming temperature dependent behaviour in Ref. [143] and is normalised to 0.39 MHz at 10 mK [30]. The two-level fluctuator (TLF) line is calculated with $P = 0$ and is normalised to 0.63 MHz at 10 mK [30]. The slowly-relaxing line is calculated assuming $\delta E = 20\,\mathrm{cm}^{-1}$ and $2\pi f \tau_{\mathrm{r},0} = 3.3$, and is normalised to 3 MHz at 10 K [30].

dominant due to the presence of rare-earth impurities (Section 6.6). Below 1 K, TLF-type impurities have been observed to be dominant (Section 6.7). Poor surface quality will lead to increased linewidths (enhanced two-magnon processes, Section 6.4) across all temperature range.

The total $k = 0$ magnon linewidth in a bulk YIG (ΔH_{YIG}) can be written as follows:

$$\Delta H_{\mathrm{YIG}} = \Delta H_{\mathrm{KL/KLC}} + \Delta H_{\mathrm{2m}} + \Delta H_{\mathrm{TP}} + \Delta H_{\mathrm{TLF}} \tag{6.17}$$

where the contributing terms are, from left to right, the Kasuya-LeCraw term or Kolokolov-L'vov-Cherepanov term, the two-magnon term, the temperature-peak term, and the TLF term. The relative contribution of these different processes as a function of tempearture is illustrated in fig. 6.8.

As we shall discover in the next chapter, in the case of YIG *films*, there is an additional damping channel that becomes important at low temperature.

7

Magnon Damping in YIG Films

This chapter reports on measurements of magnon damping in YIG films at both room and low temperatures (20 mK to 9 K). First, we shall describe various practical aspects of our sample and measurement configuration. Following on from this, we shall discuss the characteristics of our samples at room temperature, and compare the measurement results we obtain at room and low temperatures. In particular, we shall focus on the low-temperature influence of the substrate and two-level fluctuators (TLFs). The electronic preprint of this work has been uploaded in the arχiv repository [190].

7.1 Introduction

To couple quantum circuits to magnons in YIG, it is essential that the dampings of both the quantum circuit and the magnon systems is low in order to preserve quantum coherence as long as possible. In particular, for magnon-based quantum devices to be truly feasible, YIG itself has to be shown to exhibit low damping at the temperatures needed for the operation of a quantum circuit. To date, only *bulk* YIG has been shown to retain its low magnon damping behaviour at mK temperatures [30, 71, 89, 90, 186].

The story is more complicated in the case of YIG *films*. As described in Chapter 3, YIG films are typically grown on a gadolinium gallium garnet (GGG) substrate. GGG is a geometrically frustrated magnetic system that is known to be paramagnetic below 70 K [148, 191, 192]. Recent measurements at 20 K [165] showed that GGG increases the magnon damping in YIG films, but its behaviour at mK temperatures is yet to be completely understood [149, 150, 193]. Having measured YIG films on GGG at 20 mK and found the damping to be significantly increased above the room-temperature value, we set out to address the question of whether this behaviour could be attributable to the substrate.

7.2 Measurement technique

7.2.1 Introduction

Three techniques are frequently used to characterise magnon damping or linewidth in YIG: parallel pumping, fixed-frequency FMR, and broadband FMR techniques [3, 194].

The parallel-pumping technique relies on the phenomenon of parametric instability: application of a sufficiently strong microwave pump (angular frequency 2ω) parallel to the bias field will lead to the creation of counterpropagating magnons in the YIG (wavevectors k, $-k$, and angular frequency ω) [3, 34, 53, 195]. The threshold pump field needed to initiate the instability is directly related to the linewidth of the excited magnons [195]. Due to the high power required, a resonator is generally employed to amplify the energy pumped into the system. As such, the accessible frequency range of this technique is limited by that the bandwidth of the resonator. Accordingly, this technique is best suited for applications in which it is desirable to characterise the linewidth of magnons with specific k-values as shown in Refs. [152, 154, 165].

In the fixed-frequency FMR technique, a cavity which can support a highly uniform microwave excitation field is typically employed to measure the linewidth of uniformly-precessing magnons ($k = 0$) [30, 88, 96]. A microwave tone excites the cavity containing the YIG at resonance while the magnetic bias field is varied.

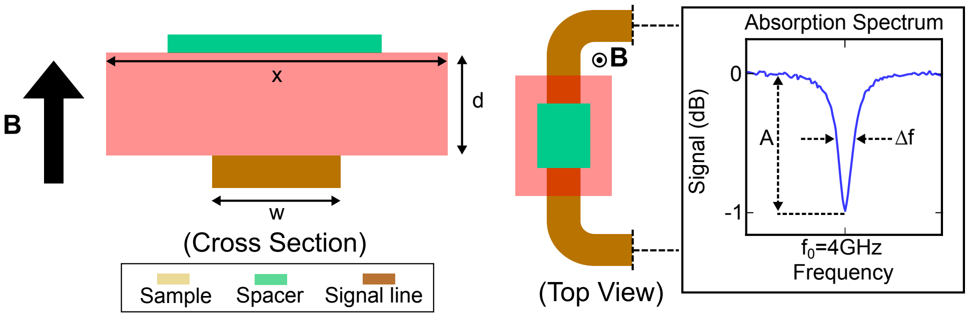

Figure 7.1: Microstrip-based technique used for the measurement of magnon linewidths.

If the frequency of a particular magnon mode coincides with the microwave tone inside the cavity, the sample starts to absorb energy, changing the amplitude of signal transmitted through it (S_{21}). The width of the absorption curve as a function of the bias field strength provides a measure of the linewidth of the excited magnon mode. This technique can typically measure only over a narrow frequency range determined by the quality factor of the cavity. Therefore, like the parallel-pumping technique, it is not well-suited to investigations in which the frequency-dependent behaviour of the linewidth are of interest.

The broadband FMR technique commonly employs a stripline as the microwave signal conduit. In contrast to the two techniques already discussed, it allows the linewidth to be measured across a wide range of frequencies (up to $\sim 40\,\mathrm{GHz}$) – all with a single stripline [57, 143, 146, 194]. The methodology is similar to the fixed-frequency FMR technique, except that measurements can also be made in which the bias field is fixed and the frequency of the microwave input signal is swept. This capability is invaluable in the study of frequency-dependent relaxation processes. There are, however, a number of drawbacks — notably the need to account for the unwanted excitations of propagating magnons (Section 7.2.3) and radiation damping (Section 7.2.4) [35, 196]. Nonetheless, in the context of our investigations, the ability to measure over a wide range of frequencies was considered to trump these inconveniences and we chose to use this technique in our experiments.

7.2.2 Experimental configuration

The stripline employed in this work is a microstrip line above which the sample is positioned as shown in fig. 7.1. It is magnetised by an external out-of-plane magnetic field (B). This field configuration minimizes the linewidth contribution from two-magnon processes (Section 6.4) brought about by the film's surface roughness [197–199]. Alternating currents transmitted through the microstrip create a microwave field which is then used to probe magnon resonances within the sample as shown in fig. 7.1. The absorption signal is fitted with a Lorentzian function and the magnon linewidth (Δf) is the full width at half maximum of the Lorentzian fit.

For low-temperature experiments, the sample is mounted at the mixing chamber stage of a dilution refrigerator in the setup shown in fig. 3.1. Our measurement frequency range is limited from 3.5 GHz to 7 GHz. Here, the low-frequency limit is imposed by the limited bandwidth of the cryogenic circulators. The high-frequency limit is imposed by the maximum magnetic field that can be produced by our setup.

7.2.3 Choosing microstrip width and sample size

In order to limit the maximum k-values, k_m, of unwanted propagating magnons that can be excited, a wide microstrip is required. Figure 7.2 shows the radiation resistance per unit length calculated for two different microstrip widths (w). The radiation resistance is proportional to the amount of power that is coupled into the magnon system. The calculations plotted in fig. 7.2 shows that the cutoff value k_m is indeed higher for a narrower microstrip. Mathematically, the theoretical radiation resistance plotted in fig. 7.2 is proportional to the Fourier transform of the current distribution within the microstrip [35]. For a homogeneous current distribution across the width, the Fourier transform is proportional to $\mathrm{sinc}(kw/2)$ with its first zero giving the corresponding cutoff wavevector $k_\mathrm{m}w/2 = \pi$. Care needs to be taken not to make the microstrip too wide as this will have the effect of making the current density within the antenna so small as to deleteriously weaken the sensitivity of the measurement setup.

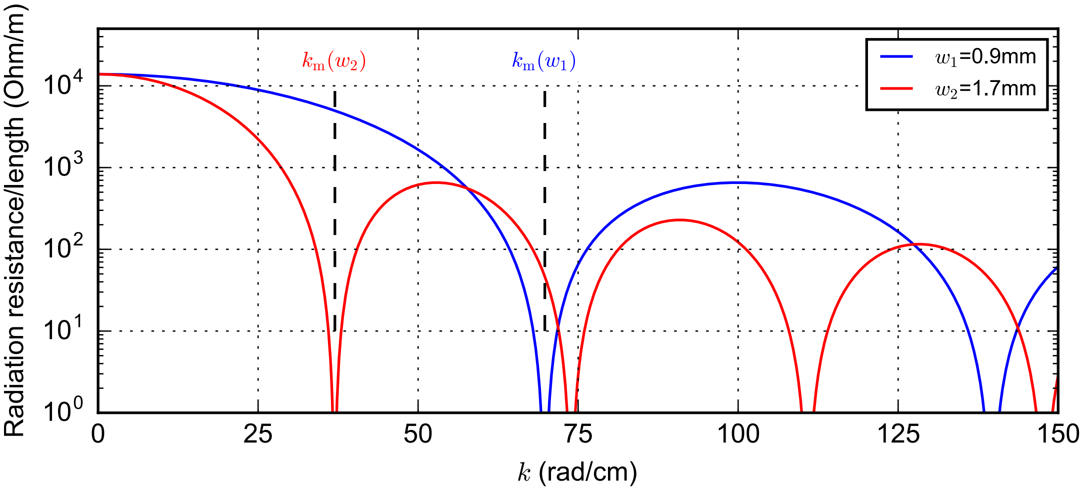

Figure 7.2: The radiation resistance per unit length of the lowest order forward volume mode [35]. The calculation assumes $M_{\mathrm{s}} = 139\,\mathrm{kA/m}$, $B = 300\,\mathrm{mT}$, a film thickness of $D = 11\,\mu\mathrm{m}$, and that the film is positioned directly on top of the antenna. The two curves correspond to two different microstrip widths ($w_1 = 0.9\,\mathrm{mm}$, $w_2 = 1.7\,\mathrm{mm}$). The current distribution is assumed to be constant across the width of the microstrip. Wavevectors corresponding to the first zero of each curve (denoted by k_{m}) are typically the maximum k value that can be excited by the microstrip.

Beyond working with a relatively wide antenna, excitations of a continuum of propagating magnons can be further suppressed by forcing the creation of standing wave modes within the samples [200, 201]. This is achieved by reducing its lateral size such that there can be multiple wave reflections from its boundaries. By analogy with a photonic cavity or resonator, only certain multiples of wavelength can create standing waves. The smaller the lateral size of the sample, the smaller the wavelength (higher the k-value) associated with the first order standing mode. Ideally, therefore, we would like to position the first-order standing wave mode as far as possible from the $k = 0$ mode by making the sample as small as possible. However, miniaturisation also decreases the absorption strength of the sample (A in fig. 7.1) since the smaller the volume, the smaller the number of spins available to interact with the input microwave signal.

Given the previous discussion concerning the geometry of the sample, it is natural to ask what would be the biggest sample size that might be used in order to achieve the highest absorption strength while still ensuring that the higher-order

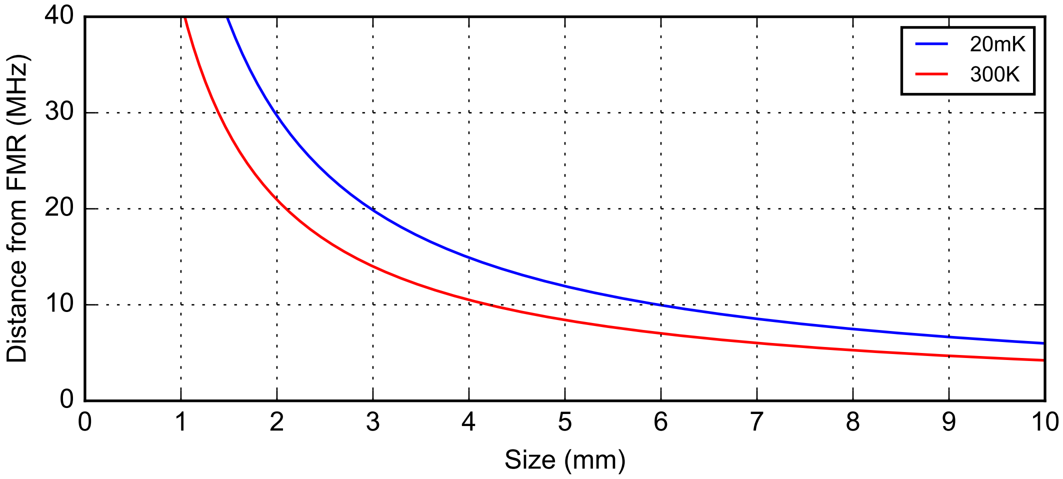

Figure 7.3: Frequency of the first standing wave mode, i.e. $f(k = \pi/x)$, relative to the $k = 0$ mode, i.e. $f(k = 0)$, as a function of the maximum lateral size of the sample x, calculated based on the dispersion relation of forward volume magnons (eq. (2.80)). Both curves are calculated for an FMR frequency of 4 GHz.

standing wave modes are not so close in frequency to the $k = 0$ mode. This ensures that they are not broadened by the presence of overlapping standing wave modes that are too near to the $k = 0$ mode — a particularly important consideration given that we anticipate that the linewidth of the $k = 0$ mode will increase at low temperatures. If we estimate that the upper bound on the magnon linewidth at 20 mK is not more than $\sim$ 15 MHz, then the nearest higher-order mode should be spaced at least 15 MHz away from the $k = 0$ mode. To estimate the position of lowest-frequency standing-wave mode, we assume it corresponds to magnons having a wavelength twice the maximum lateral size of the sample x, i.e. $\lambda = 2x$ and $k_1 = 2\pi/\lambda = \pi/x$. The corresponding wavevector k_1 is converted into a frequency value via the FVMSW dispersion relation (eq. (2.80)).

The frequency difference between the $k = 0$ mode (uniform precession) and the k_1 mode as a function of the maximum dimension of the sample x is shown in fig. 7.3 for values of M_s at 300 K and at 20 mK. Based on our approximations, for experiments at 20 mK, the result shows that $x = 4$ mm is the maximum sample size that should be used. Choosing from a selection of YIG films available to us, we opted to use a 3 mm×2 mm-sized sample.

7.2.4 Radiation damping

Radiation damping increases the measured damping of the sample and must therefore be carefully considered [196, 202]. As mentioned previously, the alternating current within the microstrip creates a microwave field that excites magnons within the sample. Radiation damping comes about as back-action of the magnons into the microstrip — the magnetic field of magnons excited within the sample induces alternating currents within the microstrip, and the ohmic dissipation of this induced current leads to an additional spurious contribution to the magnon damping.

The linewidth contribution due to radiation damping is modelled in Ref. [196] in terms of an equivalent Gilbert damping parameter α_{rad}, i.e.

$$\alpha_{\mathrm{rad}} = \eta \frac{\gamma \mu_{\circ}}{Z_{\circ}} M_{\mathrm{s}} \tilde{L}, \tag{7.1}$$

where η is a factor related to the amplitude profile of the magnetisation within the sample, $Z_{\circ}$ is the characteristic impedance of the microstrip (usually fixed at $50\,\Omega$), γ is the gyromagnetic ratio, $\mu_{\circ}$ is the vacuum permeability, M_{s} is the saturation magnetisation, and $\tilde{L}$ is the normalised mode inductance of the magnetisation mode within the sample. The normalised mode inductance is a coupling term that depends on the geometry of the system and the overlap integral (i.e. mode matching) between the microwave field of the microstrip and the amplitude profile of the magnetisation within the sample.

Radiation damping can be minimized by decreasing the coupling between the sample and the microstrip. In terms of eq. (7.1), this corresponds to reducing $\tilde{L}$. This can be achieved, for instance, by increasing the separation (d in fig. 7.1) between the sample and the microstrip. However, this comes at the expense of decreasing the absorption strength (A) in the sample and, accordingly, the effective sensitivity of the measurement setup. In light of these factors, there is a tradeoff to be made between being able to measure a linewidth that is very close to the intrinsic linewidth of the sample and being able to obtain an adequate signal-to-noise ratio (SNR). The latter is achieved by positioning the sample nearer to the stripline (negligible separation

d), thus increasing its absorption strength but at the expense of measuring linewidth values that contain a substantial radiation damping contribution.

It should be noted that the sole temperature dependency of α_{rad} originates from the saturation magnetisation M_{s}, which is expected to increase with decreasing temperature [143, 159]. If the measurement configuration is maintained between room temperature and 20 mK, i.e. no changes in the experimental geometry, α_{rad} is expected to be enhanced by a factor of approximately $M_{\mathrm{s}}(20\,\mathrm{mK})/M_{\mathrm{s}}(300\,\mathrm{K})$.

7.3 Experimental results

We now examine the results of experiments designed to probe the magnon damping in YIG films both at room temperature (300 K) and at low temperature (20 mK to 9 K). By comparing data obtained from different samples at different temperatures, we are able to move closer to an understanding of the impact of the GGG substrate on the low-temperature linewidth and uncover an additional damping mechanism that only becomes dominant at below 1 K.

Our room-temperature experiments are conducted by varying the input microwave frequency f under constant bias field B. Our low-temperature data are obtained at fixed frequency by varying the bias field, As a consequence of the lower SNR at low temperature (on account of the input being highly attenuated), significant signal averaging is needed. Each field sweep takes about 10 s. The measured absorption signal is then fitted with a Lorentzian function to extract the linewidth. This process is repeated 30 to 40 times and the calculated linewidths are averaged. The error is quantified in terms of the standard deviation of the spread of the averaged values. The linewidths can be expressed either in units of magnetic field (the measurement parameter) or converted to units of frequency via the relation $\Delta f = \gamma \Delta B / 2\pi$.

7.3.1 Room-temperature characterisation

We chose to perform experiments on two epitaxial YIG films: one of 11 µm-thickness grown on a GGG substrate and a second of 30 µm-thickness without a substrate.

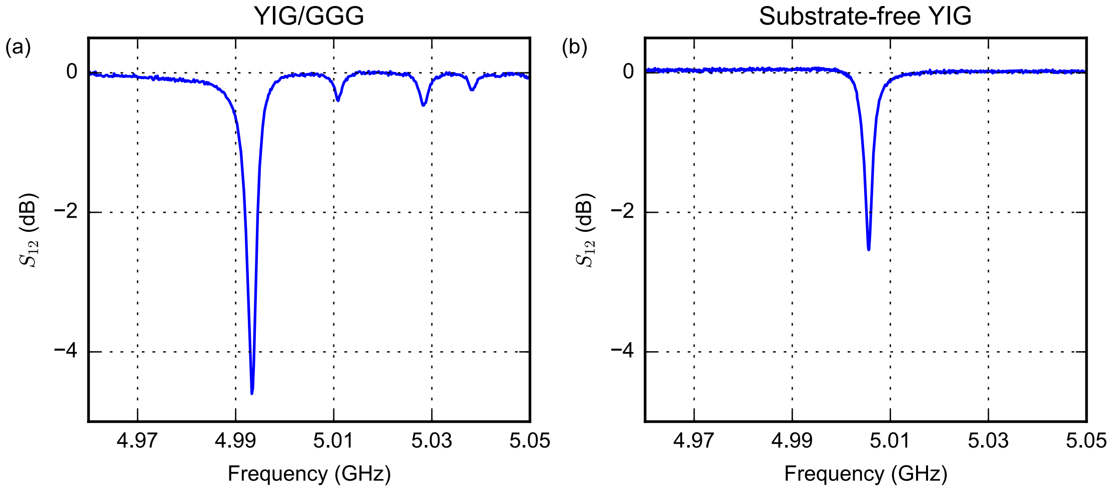

Figure 7.4: Absorption spectrum of a YIG/GGG film (panel (a)) and a substrate-free YIG film (panel(b)) measured at room temperature. Raw data have been compensated to take into account the frequency-dependent properties of the measurement setup by subtracting the measured transmission characteristics measured at zero field. YIG/GGG data is taken with the sample placed directly on top of the microstrip. Substrate-free YIG data is taken with the sample spaced by $\approx 500\,\mu\text{m}$ from the microstrip.

In what follows, these will be referred to as the YIG/GGG and substrate-free YIG. The substrate-free YIG was obtained by polishing away the GGG layer from a YIG/GGG sample with 53 μm-thick YIG layer [165].

The YIG/GGG sample has a lateral size of $\sim 3\,\text{mm}\times 2\,\text{mm}$ (see Section 7.2.3) and is used in conjunction with a 1.7 mm-wide microstrip with a characteristic impedance of 50 Ω. The long axis of the sample is oriented along the long axis of the stripline. Figure 7.4(a) shows the observed magnon resonances for the film at room temperature. The data shows a strong absorption dip at $\approx 4.992\,\text{GHz}$, thought to be the uniform precession mode of the sample ($k = 0$), and a series of weaker dips at higher frequencies. This is to be expected since the uniform precession mode of forward volume magnons ($k = 0$) has a lower frequency compared to propagating modes ($k \neq 0$). In addition, the nearest secondary dip is ~16 MHz from frequency of the uniform precession mode, roughly as predicted according to fig. 7.3 (red line).

To examine the linewidths (Δf) of the $k = 0$ mode, we performed a linear fit of the data to the relation $\Delta f = 2\alpha f_\circ + \Delta f_\circ$, where $f_\circ$ is the resonance frequency. This fit gives the characteristic Gilbert damping constant α (unitless) and the

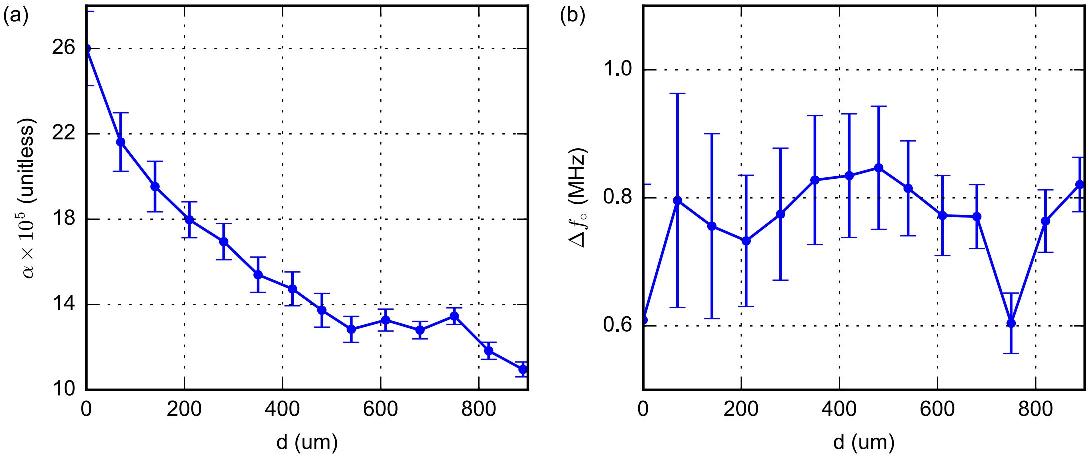

Figure 7.5: The measured damping constant (α) and inhomogeneous contribution term ($\Delta f_\circ$) as a function of the separation (d) between the YIG/GGG sample and the microstrip. The error bar reflects the fitting uncertainty for each data point.

inhomogeneous broadening contribution $\Delta f_\circ$. Typically, the Gilbert damping constant quantifies the amount of internal magnon damping within the sample itself, which we denote as α_{mag}. In our experiments, the measured damping constant also includes the radiation damping contribution (α_{rad}, see Section 7.2.4), i.e. $\alpha = \alpha_{\text{mag}} + \alpha_{\text{rad}}$. The inhomogeneous contribution $\Delta f_\circ$ represents the frequency-independent part of the linewidth. This typically originates from the inhomogeneity of the sample, the spatial inhomogeneity of the field, and broadening due to the process of averaging over multiple measurements.

Figure 7.5 shows the evolution of both α and $\Delta f_\circ$ as the spacing d between the YIG/GGG sample and the microstrip is increased. The spacer employed comprises of either a few layers of Kapton tape (1 layer $\approx$ 70 µm), a piece of single crystal sapphire (thickness $\sim$ 540 µm), or a combination of these. As expected, the measured damping constant α decreases as d is increased, in agreement with the model presented previously (eq. (7.1)). The inhomogeneous contribution term $\Delta f_\circ$, is not in general affected by the change in the spacing between the sample and the microstrip. In anticipation of increased linewidth at low temperature, a spacing of d =70 µm was used in measurements of the YIG/GGG film. Such a spacing leads to a substantial radiation damping contribution in the measured magnon linewidth, but can be expected to assure good signal-to-noise ratio even if the sample becomes much more lossy.

The substrate-free YIG film, which has a lateral size of $\sim 1\,\mathrm{mm}\times 1\,\mathrm{mm}$ (the largest sample available), is measured using a 0.9 mm-wide 50 Ω microstrip. In the case of this sample, the antennae were spaced much further from the surface ($d = 540\,\mu\mathrm{m}$), leading to smaller radiation damping contribution. Figure 7.4(b) shows the observed magnon resonance for the substrate-free YIG film at room temperature. Only one absorption dip is observed in this case — the $k = 0$ mode. The absorption strength is smaller than in case of YIG/GGG sample, owing to a larger value of d and a smaller sample volume.

7.3.2 Role of GGG at 20 mK

Figure 7.6 compares the magnon linewidth Δf of each sample at 300 K (room temperature) and at 20 mK as a function of resonance frequency f_o. Table 7.1 provides a summary of linear fits to these data.

Table 7.1: Comparing results at 300 K and at 20 mK

	YIG/GGG	**Substrate-free YIG**
Size	$2\,\mathrm{mm}\times 3\,\mathrm{mm}\times 11\,\mu\mathrm{m}$	$\sim 1\,\mathrm{mm}\times 1\,\mathrm{mm}\times 30\,\mu\mathrm{m}$
w/d	$1.7\,\mathrm{mm}$ / $70\,\mu\mathrm{m}$	$0.9\,\mathrm{mm}$ / $540\,\mu\mathrm{m}$
300 K	$\alpha_{1\mathrm{a}} = (22 \pm 4) \times 10^{-5}$ $\Delta f_{\mathrm{o},1\mathrm{a}} = (0.7 \pm 0.4)\,\mathrm{MHz}$	$\alpha_{2\mathrm{a}} = (8.9 \pm 0.5) \times 10^{-5}$ $\Delta f_{\mathrm{o},2\mathrm{a}} = (0.9 \pm 0.1)\,\mathrm{MHz}$
20 mK P_b=-65 dBm	$\alpha_{1\mathrm{b}} = (74 \pm 5) \times 10^{-5}$ $\Delta f_{\mathrm{o},1\mathrm{b}} = (1.7 \pm 0.6)\,\mathrm{MHz}$	$\alpha_{2\mathrm{b}} = (2.3 \pm 0.7) \times 10^{-5}$ $\Delta f_{\mathrm{o},2\mathrm{b}} = (1.1 \pm 0.1)\,\mathrm{MHz}$
20 mK P_c=-100 dBm	$\alpha_{1\mathrm{c}} = (85 \pm 6) \times 10^{-5}$ $\Delta f_{\mathrm{o},1\mathrm{c}} = (2.6 \pm 0.6)\,\mathrm{MHz}$	$\alpha_{2\mathrm{c}} = (9.3 \pm 1.0) \times 10^{-5}$ $\Delta f_{\mathrm{o},2\mathrm{c}} = (2.0 \pm 0.1)\,\mathrm{MHz}$

We first compare the results at 300 K and at 20 mK obtained with high input power ($P_\mathrm{b} = -65\,\mathrm{dBm}$). At 20 mK, the measured linewidth of the uniformly-precessing ($k = 0$) mode in substrate-free YIG decreases to approximately 1.4 MHz, lower than its room-temperature value across the measurement frequency range (3.5 GHz-7.0 GHz). The sample's Gilbert damping constant at 20 mK ($\alpha_{2\mathrm{b}} \approx 2.3 \times 10^{-5}$) is almost four times lower than its room-temperature value ($\alpha_{2\mathrm{a}}$).

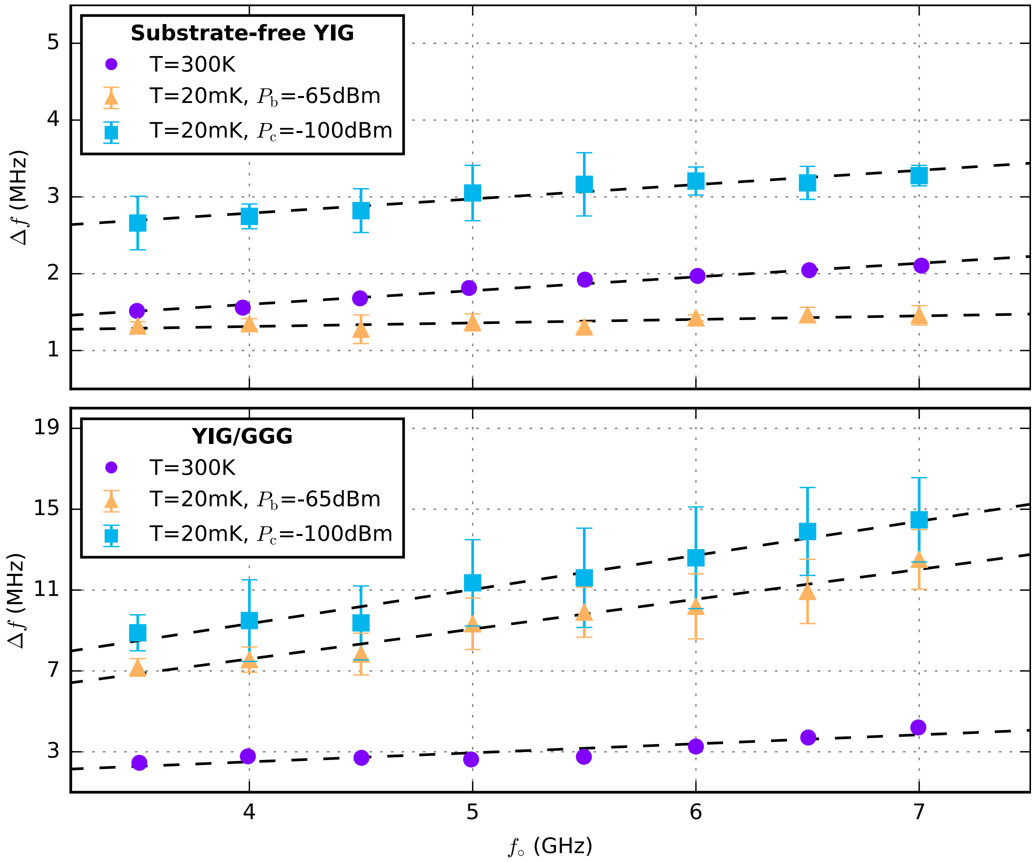

Figure 7.6: Magnon linewidths Δf versus its resonance frequency $f_\circ$ for a YIG/GGG film and a substrate-free YIG film. The datasets at room temperature (300 K, •) are obtained with an input power of -25 dBm. The datasets at 20 mK are obtained for two input powers $P_\mathrm{b} = -65$ dBm, and $P_\mathrm{c} = -100$ dBm. Dashed lines are linear fits and the fit results are summarised in table 7.1. Note the different scaling in the vertical axis of the plots.

We recall that the measured damping constant is the sum of the intrinsic damping and the radiation damping, i.e. $\alpha = \alpha_\mathrm{mag} + \alpha_\mathrm{rad}$. The radiation damping α_rad is expected to increase at low temperature (due to the M_s dependence in eq. (7.1)). The data therefore suggest that the intrinsic contribution decreases as the temperature is lowered down to 20 mK:

$$\alpha_\mathrm{2b} < \alpha_\mathrm{2a} \quad \Rightarrow \quad \alpha_\mathrm{mag}(\mathrm{T{=}20\,mK}) < \alpha_\mathrm{mag}(\mathrm{T{=}300\,K}). \tag{7.2}$$

Such a decrease in intrinsic damping is expected as most of the internal relaxation processes for the $k = 0$ mode, such as the Kasuya-LeCraw and the Kolokolov-L'vov-Cherepanov, are expected to become less effective as the temperature is lowered (see Section 6.3). We also learn from these results that the radiation damping only constitutes a small part of the total damping at room temperature (α_{2a}) — this is not unexpected given the large spacing between the sample and the microstrip ($d = 540\,\mu\mathrm{m}$).

The inhomogeneous broadening contribution to the damping in the substrate-free YIG at 20 mK ($\Delta f_{\circ,\mathrm{2b}}$) is slightly higher than its value at room temperature ($\Delta f_{\circ,\mathrm{2a}}$). This is probably an artefact of the measurement procedure: the results at low temperature are obtained with high averaging, which likely inhomogeneously broadens the measured linewidths if the current source of the magnet is not completely drift-free.

Results from the measurements of the YIG/GGG film, are very different. Its damping constant at 20 mK (α_{1b}) is 3.4 times *larger* than its value at room temperature (α_{1a}). In addition, the increase in the inhomogeneous contribution ($\Delta f_{\circ,\mathrm{1b}}/\Delta f_{\circ,\mathrm{1a}} \approx 2.4$) is also much larger than the increase seen for the substrate-free YIG ($\Delta f_{\circ,\mathrm{2b}}/\Delta f_{\circ,\mathrm{2a}} \approx 1.2$) and too large to be attributable to instability of the measurement setup.

Before any conclusions can be drawn from comparing the results of YIG/GGG and the substrate-free YIG samples, it is necessary to estimate the upper bound of the radiation damping contribution to the measured damping constant of YIG/GGG at 20 mK. The radiation damping, modelled according to eqn. (7.1), depends on the geometry of the system and the saturation magnetisation M_s of the sample. As characterisations at both 300 K and 20 mK are performed with the same configuration of microstrip and sample, it is reasonable to expect that the change in α_{rad} as the temperature is lowered is due solely to the change in M_s. Therefore, the increase in α_{rad} between 20 mK and 300 K is determined by the ratio of the saturation magnetisation, i.e. $M_\mathrm{s}(20\,\mathrm{mK})/M_\mathrm{s}(300\,\mathrm{K}) \approx 1.4$ [143], and

$$\alpha_{\mathrm{rad}}(\mathrm{T{=}20\,mK}) \approx 1.4\,\alpha_{\mathrm{rad}}(\mathrm{T{=}300\,K}). \tag{7.3}$$

If we assume that the measured damping constant (α) of the YIG/GGG film only consists of intrinsic damping within the YIG itself (α_{mag}) and the radiation damping contribution (α_{rad}), then taking into account eqn. (7.2) and (7.3), we can make the following argument:

$$\begin{aligned}
\alpha(\text{T}{=}20\,\text{mK}) &= \alpha_{\text{mag}}(\text{T}{=}20\,\text{mK}) + \alpha_{\text{rad}}(\text{T}{=}20\,\text{mK}), && (7.4)\\
&\approx \alpha_{\text{mag}}(\text{T}{=}20\,\text{mK}) + 1.4\,\alpha_{\text{rad}}(\text{T}{=}300\,\text{K}), && (7.5)\\
&< \alpha_{\text{mag}}(\text{T}{=}300\,\text{K}) + 1.4\,\alpha_{\text{rad}}(\text{T}{=}300\,\text{K}), && (7.6)\\
&< 1.4\,\left(\alpha_{\text{mag}}(\text{T}{=}300\,\text{K}) + \alpha_{\text{rad}}(\text{T}{=}300\,\text{K})\right), && (7.7)\\
\alpha(\text{T}{=}20\,\text{mK}) &< 1.4\,\alpha(\text{T}{=}300\,\text{K}). && (7.8)
\end{aligned}$$

That is, the radiation damping accounts for, at most, an increase of approximately 1.4 times in the measured damping constant of the YIG/GGG sample when it is cooled from 300 K to 20 mK. Accordingly, the fact that we measure a much larger increase in the damping constant of the YIG/GGG sample, i.e. $\alpha_{1\text{b}} \approx 3.4\,\alpha_{1\text{a}}$, implies that there is an additional damping channel for magnons in the YIG/GGG film that is not accounted for in eqn. (7.4). As the difference between the YIG/GGG sample and the substrate-free YIG sample lies solely in the presence of the GGG substrate, our result is a strong indication that the GGG plays a significant role in increasing the magnon linewidths in the YIG/GGG sample at 20 mK.

From table 7.1, we see that the damping constants and the inhomogeneous contributions for both samples at 20 mK increase when the input power is lowered (P_{c}). As we shall explore in the next section, this behaviour can be understood by taking into account additional damping behaviour originating from two-level fluctuators (TLF, see Section 6.7) that are only significant at low temperature and low drive power.

7.3.3 Temperature-dependent damping

Figure 7.7 shows the temperature dependence of the magnon linewidth of both samples measured with low input power ($P_{\text{c}} = -100\,\text{dBm}$).

When examining the results for YIG/GGG in fig. 7.7, the radiation damping contribution across the examined temperature range amounts to an approximately

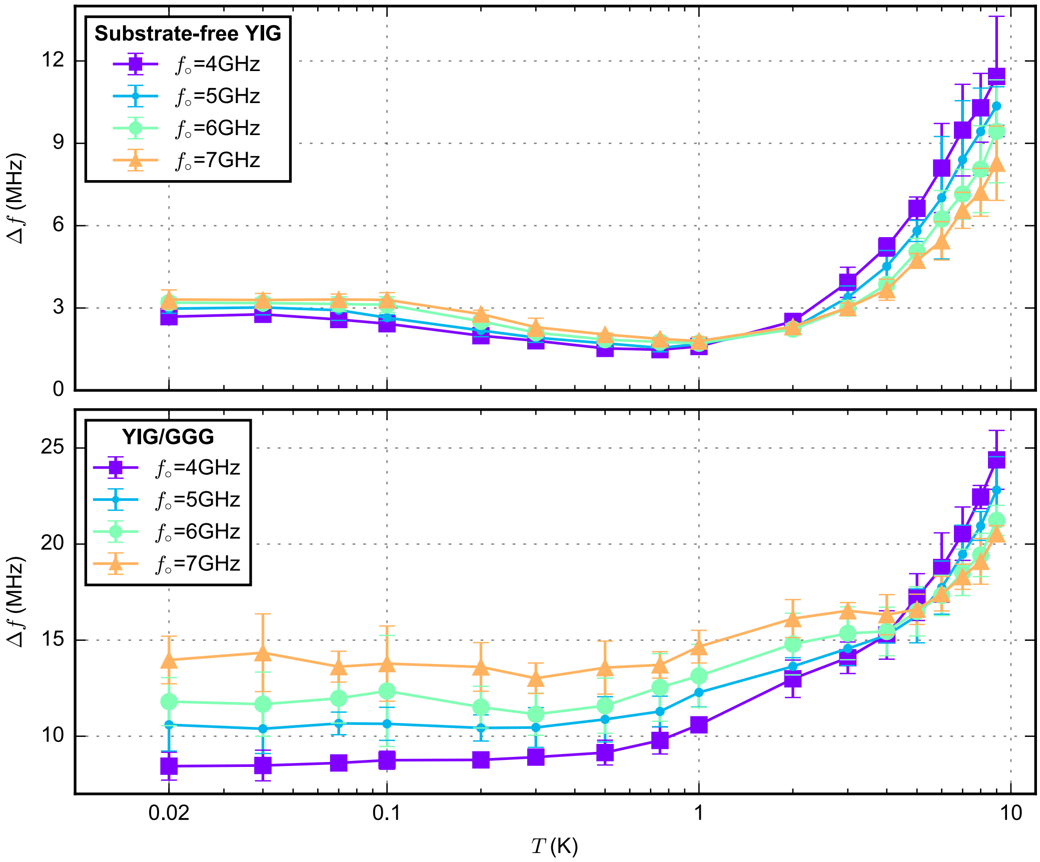

Figure 7.7: Temperature (T) dependent magnon linewidths (Δf) for both YIG/GGG film and substrate-free YIG, measured with input power $P_c = -100\,\mathrm{dBm}$. Note the different scaling in the vertical axis of the plots.

constant vertical offset to each dataset. This is due to the small change (less than 0.03%) in the value of M_s for YIG between 20 mK and 9 K [159].

Above 1 K, linewidths of both samples increase as the temperature is increased to 9 K. In this temperature regime, the dominant damping is usually associated with temperature-peak processes (see Section 6.6). When temperature-peak processes are dominant, the linewidth of the sample peaks at a characteristic temperature (T_ch).

As discussed in Section 6.6, the three known temperature-peak processes are due to rapidly-relaxing impurities, slowly-relaxing impurities, and the valence exchange mechanism. The rapidly relaxing model produces a Gilbert-like damping and has a characteristic temperature (T_ch) that is independent of the magnon resonance frequency $f_\circ$. The slowly-relaxing and the valence-exchange models exhibit a non-Gilbert-like form and a characteristic temperature (T_{ch}) that reduces as the resonance frequency ($f_{\circ}$) is lowered.

The behaviour observed in fig. 7.7 at 9 K, in which the linewidth for $f_{\circ} = 4\,\mathrm{GHz}$ is higher than that measured at $f_{\circ} = 7\,\mathrm{GHz}$, indicates that whatever mechanism is dominating the damping is not Gilbert-like in character; this immediately excludes the rapidly-relaxing model. The valence-exchange effect due to Fe^{2+} has previously been shown to be dominant above room temperature (as discussed in Section 6.4). By process of elimination, therefore, the slowly-relaxing model is the only mechanism that can be dominant at this temperature range.

7.3.4 Damping due to two-level fluctuators

As the temperature is decreased below 1 K, the linewidth of the substrate-free YIG starts to increase and eventually saturates at mK temperatures as shown in fig. 7.7. We propose that this behaviour can be explained by the TLF model discussed in Section 6.7. Note that previously this mechanism had only been observed in *bulk* YIG [30, 186].

Evidence for the TLF-induced damping is seen in fig. 7.6, fig. 7.8 and fig. 7.9. The 20 mK datasets in fig. 7.6 show that the linewidths for both samples are lower when the drive level is higher (P_{b} vs P_{c}). This is confirmed by the extracted damping constants and inhomogeneous contribution terms obtained at low power P_{c} which are found to be higher than the ones obtained at high power P_{b} (Table 7.1). Figure 7.8 shows the magnon linewidth of the substrate-free YIG as a function of drive levels P at three different temperatures (1 K, 300 mK, and 20 mK). At 1 K, there is no observable power dependence. We propose that this is because the TLFs have been saturated by thermal phonons. At 20 mK and 300 mK, the linewidths increase as the power decreases and saturate progressively as the temperature is reduced, in agreement with the previous discussions. The data are fitted using eq. (6.16) with an additional y-intercept to account for non-TLF contributions to the linewidth.

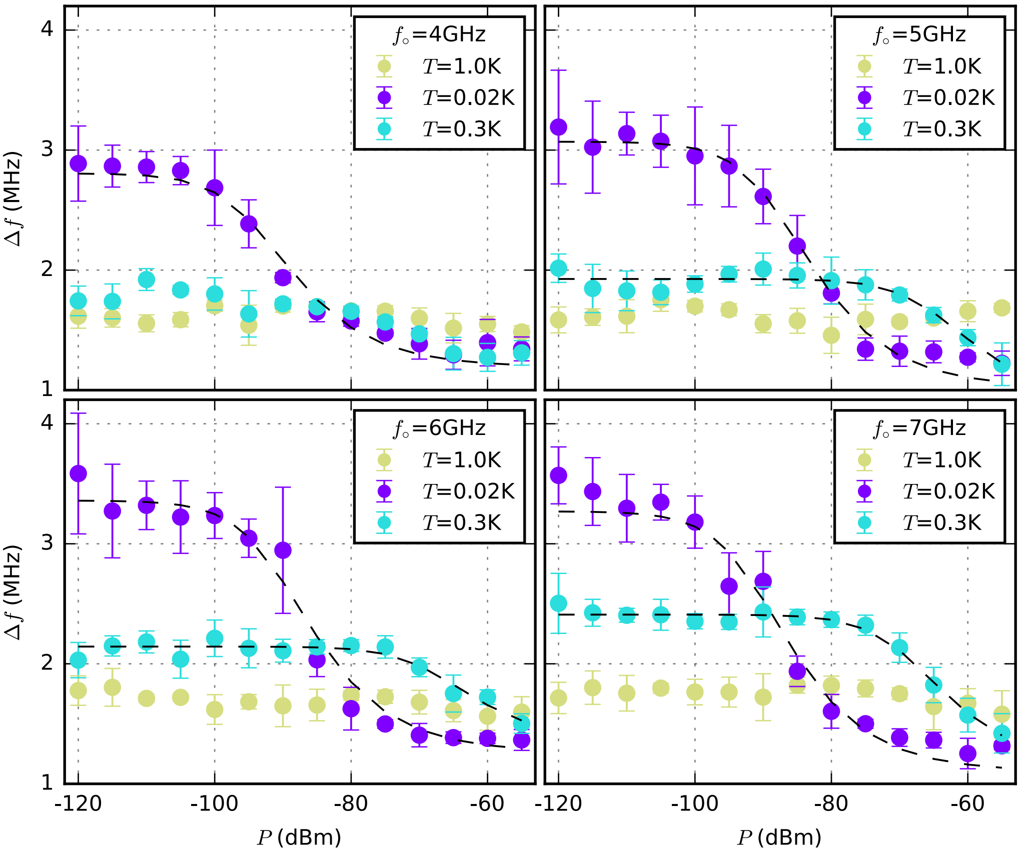

Figure 7.8: Magnon linewidths Δf in the substrate-free YIG film as a function of input powers P, obtained at 20 mK, 300 mK, and 1 K. The dashed lines are fits to the data.

For the $f_\circ = 5\,\mathrm{GHz}, 6\,\mathrm{GHz}, 7\,\mathrm{GHz}$ dataset in fig. 7.8, P_{sat} at 300 mK is clearly higher than at 20 mK. This is in-line with expectations: τ_1 and τ_2, the TLF longitudinal and transverse relaxation times, are anticipated to decrease as the temperature is increased, leading to a higher P_{sat} (recall that $P_{\mathrm{sat}} \propto 1/\tau_1\tau_2$ from previous chapter). The exact temperature dependence of $1/\tau_1\tau_2$ is not clear. In previous experiments, a phenomenological model was suggested with the quantity $1/\tau_1\tau_2$ varying from T^2 to T^4 [203]. This places the ratio $(P_{\mathrm{sat}}(300\,\mathrm{mK})/P_{\mathrm{sat}}(20\,\mathrm{mK}))_{\mathrm{theory}}$ in the range between 23.5 dB and 47 dB. The fitted P_{sat} values from our data correspond to a ratio $(P_{\mathrm{sat}}(300\,\mathrm{mK})/P_{\mathrm{sat}}(20\,\mathrm{mK}))_{\mathrm{data}}$ of approximately 23 dB, suggestive of a T^2 behaviour.

It should be noted that the $f_\circ = 4\,\mathrm{GHz}$, $T = 300\,\mathrm{mK}$ dataset in fig. 7.8 is not fitted with the TLF model. Here, the TLF effect is very weak since there are sufficient

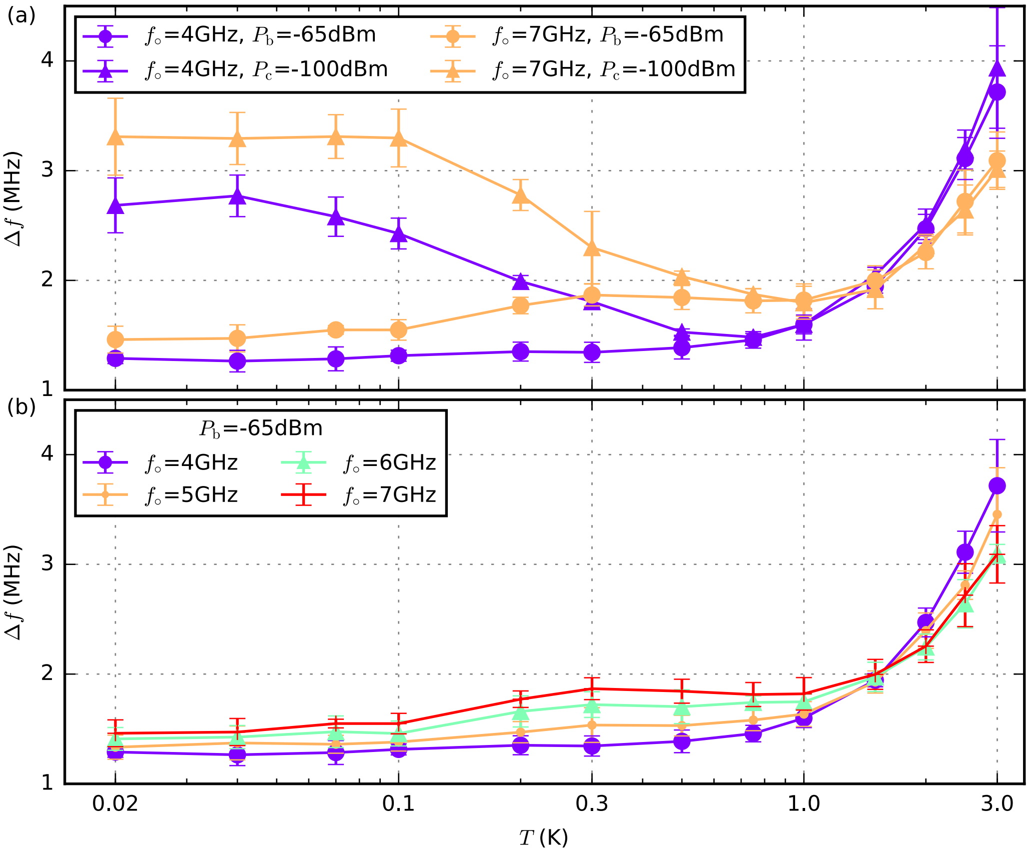

Figure 7.9: Magnon linewidths Δf of the substrate-free YIG film from $T = 20\,\mathrm{mK}$ to $T = 3\,\mathrm{K}$. (a) Comparison between the two different input powers $P_\mathrm{b} = -65\,\mathrm{dBm}$ and $P_\mathrm{c} = -100\,\mathrm{dBm}$. (b) Comparison between different resonance frequencies $f_\circ$ at input power $P_\mathrm{b} = -65\,\mathrm{dBm}$.

thermal phonons to saturate those fluctuators with central frequencies around 4 GHz.

Figure 7.9(a) shows the manifestation of the TLF effect as a function of temperature. Above 1 K, linewidths for both input powers coincide. This is an indication that the relevant TLFs have been saturated by the thermal phonons. At lower temperatures, the magnon linewidths for measured at both powers split, with the linewidths at low input power P_b being higher than the ones at high input power P_c.

A quick comparison with the data in fig. 7.8 shows that input power $P_\mathrm{b} = -65\,\mathrm{dBm}$ is not enough to saturate the TLFs at 300 mK. The datasets obtained with high drive level (P_b) in fig. 7.9(b) show that the linewidth difference $\delta f = |\Delta f(f_\circ = 7\,\mathrm{GHz}) - \Delta f(f_\circ = 4\,\mathrm{GHz})|$ broadens as the temperature is increased

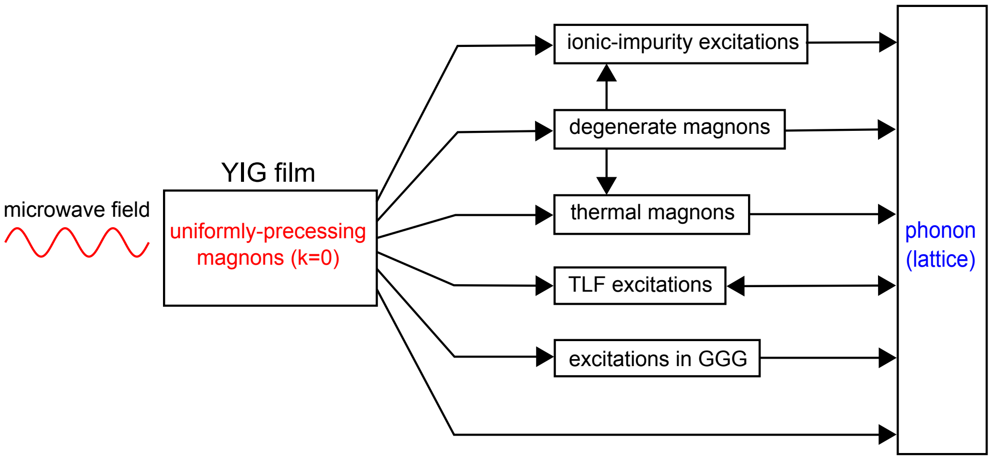

Figure 7.10: Relaxation paths for uniformly-precessing microwave magnons ($k = 0$) in YIG *films*, from mK temperatures to room temperature.

from 100 mK to 300 mK, narrowing back as the temperature reaches 1 K. If a much higher drive level were to be used, the TLFs would be expected to also be saturated (between 100 mK and 1 K) and we would predict a smaller value of δf.

7.4 Summary

For the first time, we have been able to show that GGG, the substrate on which YIG films are usually grown, plays an important role in increasing magnon linewidths at millikelvin temperatures (Section 7.3.2). Temperature-dependent linewidths above 1 K in YIG/GGG and substrate-free samples are associated with the slowly-relaxing-impurity mechanism typically observed in YIG with rare-earth impurities (Section 7.3.3). Damping due to the presence of unsaturated TLFs is observed in both YIG/GGG and substrate-free YIG films below 1 K (Section 7.3.4). The TLF saturation power at 300 mK is found to be higher than at 20 mK; the ratio between the two values suggests a T^{-2}-dependent behaviour for the product of TLF relaxation times ($\tau_1\tau_2$). Furthermore, we verify that using high-drive power can lower the $k = 0$ magnon linewidth of substrate-free YIG down to $\sim$ 1.4 MHz ($f_\circ$ = 3.5 GHz to 7.0 GHz) at 20 mK — lower than its room-temperature value and comparable to that measured in bulk YIG at 20 mK [30, 186]. Figure 7.10

summarises the known relaxation paths for uniformly-precessing magnons in YIG *films* excited by a microwave field (compare this with those for *bulk* YIG, fig. 6.1).

8

Outlook

The preceding chapters have taken the readers on a journey through several microwave magnonic experiments carried out in a millikelvin-temperature environment. In the last chapter of this thesis, the author will attempt to summarise the various findings and outline several experiments that might form a natural extension of the work.

In Chapter 4, we explored a hybrid system in which magnons in a YIG sphere were strongly coupled to photons in a niobium-based superconducting planar resonator. The planar superconducting circuit architecture showcased in this experiment is extremely versatile and potentially opens doors to a wide range of related investigations. Three such opportunities are particular apparent.

Firstly, as can be seen from fig. 8.1, the magnetic fields in vicinity of the meandering section of the resonator used in our experiments (linecuts B and C in fig. 4.1) are very different from those at the center (linecut A in fig. 4.1, field plot in fig. 4.3(b)). This hints at the possibility of demonstrating strong coupling to different magnetostatic modes of the magnonic system selected by judicious positioning relative to the resonator. Such an experiment could be an enabling step towards the development of a device that selectively stores information in specific non-interacting modes of a magnetic system.

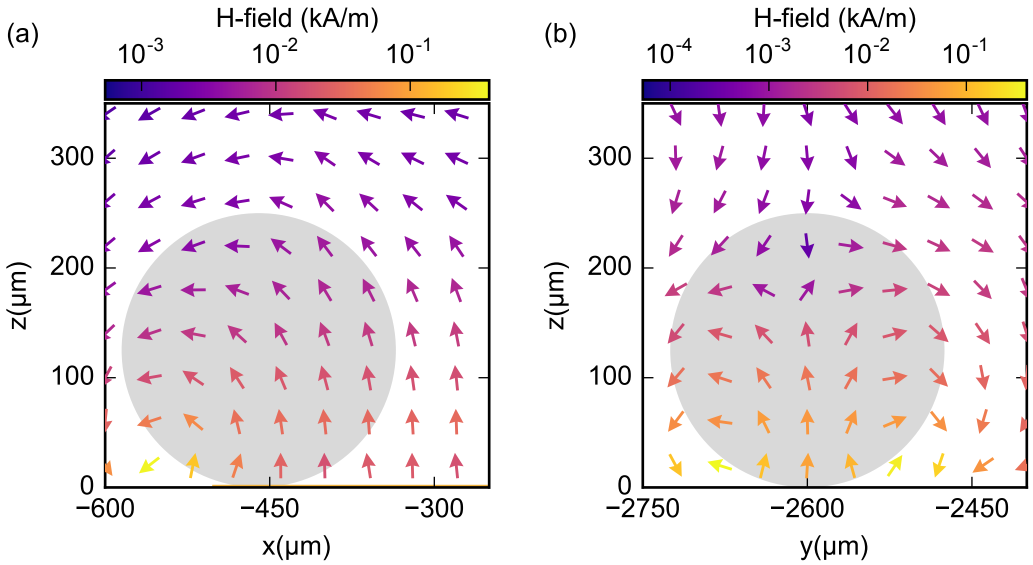

Figure 8.1: The magnetic vector fields around the meandering line of our resonator (cross section B and C in fig. 4.1) excited at its fundamental mode. Compare this with the field directions at the middle of resonator (fig. 4.3). Note that the colour map is plotted on a logarithmic scale. Shown on the plot is a 0.25 mm diameter circle representing the YIG sphere. If the resonator is excited at its higher order modes, the field amplitudes in this region can be enhanced. (a) Cross section B ($y = -2600\,\mu$m). (b) Cross section C ($x = -450\,\mu$m).

Secondly, it should be possible to study the indirect coupling between two magnonic systems via the photons in the 2D superconducting resonator; a related experiment has been conducted using a coaxial resonator [107], but could be directly translated into our 2D geometry. Such an architecture, if combined with electronics to allow the local bias field at one of the spheres to be altered, would allow for selective information transfer between (and readout from) the two magnetic systems — a functionality that could be invaluable in the context of a quantum device.

Thirdly, one could adapt the geometry of the experiment to allow for the study of the coupling between two planar superconducting resonators mediated by non-reciprocal travelling magnons (MSSW, see Chapter 2) in a magnonic *film* (see discussion on chiral light-matter interaction in Ref. [204]).

In Chapter 5, we demonstrated the measurement of a bandgap in a YIG waveguide-based static magnonic crystal under continuous- and pulsed- microwave excitations at millikelvin temperatures. We observed that the damping in the magnonic crystal was markedly higher at 20 mK than at room temperature and were able to attribute this increased damping to the substrate on which the film was grown — gadolinium gallium garnet (GGG, see Chapter 7). The magnetic state of GGG at millikelvin temperatures remains somewhat mysterious [149, 150, 190, 193]. A future low-temperature study to probe the properties of GGG more closely would therefore be invaluable – perhaps through further investigation of the extent to which ferromagnetic resonance in YIG is influenced by the presence of GGG across wide ranges of temperature and magnetic field.

To be useful in the context of quantum devices, the YIG waveguide-based magnonic crystal (both static and dynamic versions) must be a low-loss system. Our findings (Chapters 5 and 7) suggest that one potential way of assuring this would be to create a device free from the GGG substrate. This could either be achieved by depositing a thick film and removing the GGG layer, or growing the film on an alternative substrate [205]. Neither of these approaches are straightforward, but the associated challenges are essentially engineering ones rather than those originating from fundamental physical constraints and — with the application of sufficient effort — can be realistically expected to be surmountable.

In our measurements of substrate-free YIG in Chapter 7, we showed that, by lowering the temperature of the material to 20 mK and saturating the two-level fluctuators (TLFs, see Chapter 6) with high-drive microwave power, we were able to reduce the magnon damping to a level below its room-temperature value. Though the high drive power required to achieve this is not compatible with magnon-based devices that operate at the single-magnon or photon level, this is nonetheless a promising result. We suggest that further investigation into the origin of TLFs in YIG is essential. For instance, highly-purified YIG with negligible rare-earth substitutional impurities could perform well at low temperatures [144, 165]. TLFs have been shown to be an important damping mechanism both in bulk material [30, 186] and, through our study, in films. One interesting unresolved question relates to how the TLFs may be distributed through the material – are they, for example, more localised at the surface, or spread throughout the volume?

Finally, against the backdrop of our findings, a useful experiment to undertake might be one that involves measuring a standing-mode resonance of a YIG film on a GGG substrate in a 3D superconducting cavity. Though less interesting in a device context than an architecture comprising a 2D resonator and a YIG film, such a measurement geometry would make it relatively easy to assess whether it is possible to enter the strong-coupling regime when working with a YIG/GGG system and a photonic resonator.

References

[1] V.V. Kruglyak, S.O. Demokritov, and D. Grundler. “Magnonics”. In: *Journal of Physics D: Applied Physics* 43.26 (July 2010), p. 264001. URL: http://stacks.iop.org/0022-3727/43/i=26/a=264001?key=crossref.7d59bbfceddaf0f03df576a620cfcdf3.

[2] J.H.E. Griffiths. “Anomalous High-frequency Resistance of Ferromagnetic Metals”. In: *Nature* 158.4019 (Nov. 1946), pp. 670–671. URL: http://www.nature.com/articles/158670a0.

[3] A.A. Serga, A.V. Chumak, and B. Hillebrands. “YIG magnonics”. In: *Journal of Physics D: Applied Physics* 43.26 (July 2010), p. 264002. URL: http://stacks.iop.org/0022-3727/43/i=26/a=264002?key=crossref.6a073bfc1c8ba106fa1ba87bbfe37df3.

[4] G. Gubbiotti et al. “Brillouin light scattering studies of planar metallic magnonic crystals”. In: *Journal of Physics D: Applied Physics* 43.26 (July 2010), p. 264003. arXiv: 1004.1881. URL: http://stacks.iop.org/0022-3727/43/i=26/a=264003?key=crossref.92ba5f72027b0a61fe73d4a1e52657e9.

[5] S.-K. Kim. “Micromagnetic computer simulations of spin waves in nanometre-scale patterned magnetic elements”. In: *Journal of Physics D: Applied Physics* 43.26 (July 2010), p. 264004. arXiv: /arxiv.org/abs/1101.0479 [http:]. URL: http://stacks.iop.org/0022-3727/43/i=26/a=264004?key=crossref.6792db59ffb74954bc53f5b6fb0ce47a.

[6] A. Khitun, M.Q. Bao, and K.L. Wang. “Magnonic logic circuits”. In: *Journal of Physics D: Applied Physics* 43.26 (July 2010), p. 264005. URL: http://stacks.iop.org/0022-3727/43/i=26/a=264005?key=crossref.f9dd566068384c0f843c64d4110dbb4d.

[7] B. Lenk et al. “The building blocks of magnonics”. In: *Physics Reports* 507.4-5 (Oct. 2011), pp. 107–136. arXiv: 1101.0479. URL: http://dx.doi.org/10.1016/j.physrep.2011.06.003.

[8] S.O. Demokritov and A.N. Slavin, eds. *Magnonics*. Vol. 125. Topics in Applied Physics. Berlin, Heidelberg: Springer Berlin Heidelberg, 2013. URL: http://link.springer.com/10.1007/978-3-642-30247-3.

[9] M. Krawczyk and D. Grundler. “Review and prospects of magnonic crystals and devices with reprogrammable band structure”. In: *Journal of Physics: Condensed Matter* 26.12 (Mar. 2014), p. 123202. URL: http://stacks.iop.org/0953-8984/26/i=12/a=123202?key=crossref.350fe7c4c80a04d5d71300397a719757.

[10] A.V. Chumak et al. “Magnon spintronics”. In: *Nature Physics* 11.6 (June 2015), pp. 453–461. URL: http://www.nature.com/articles/nphys3347.

[11] C. Sun, T. Nattermann, and V.L. Pokrovsky. "Bose–Einstein condensation and superfluidity of magnons in yttrium iron garnet films". In: *Journal of Physics D: Applied Physics* 50.14 (Apr. 2017), p. 143002. URL: `http://stacks.iop.org/0022-3727/50/i=14/a=143002?key=crossref.d41e44262194f0de4cd15c294addb1ba`.

[12] K. Nakata, P. Simon, and D. Loss. "Spin currents and magnon dynamics in insulating magnets". In: *Journal of Physics D: Applied Physics* 50.11 (Mar. 2017), p. 114004. arXiv: `1610.08901`. URL: `http://stacks.iop.org/0022-3727/50/i=11/a=114004?key=crossref.ceca069820e6a4325424815f4abdf6bb`.

[13] M. Garst, J. Waizner, and D. Grundler. "Collective spin excitations of helices and magnetic skyrmions: review and perspectives of magnonics in non-centrosymmetric magnets". In: *Journal of Physics D: Applied Physics* 50.29 (July 2017), p. 293002. URL: `http://stacks.iop.org/0022-3727/50/i=29/a=293002?key=crossref.20fc6ecb1a45d58744090fb9c4bf195b`.

[14] A.V. Chumak, A.A. Serga, and B. Hillebrands. "Magnonic crystals for data processing". In: *Journal of Physics D: Applied Physics* 50.24 (June 2017), p. 244001. arXiv: `1702.06701`. URL: `http://stacks.iop.org/0022-3727/50/i=24/a=244001?key=crossref.a2a8d5a441fab4b58ca8c55e719bcd9d`.

[15] G. Csaba, Á. Papp, and W. Porod. "Perspectives of using spin waves for computing and signal processing". In: *Physics Letters A* 381.17 (May 2017), pp. 1471–1476. URL: `https://linkinghub.elsevier.com/retrieve/pii/S0375960116316486`.

[16] K. Zakeri. "Terahertz magnonics: Feasibility of using terahertz magnons for information processing". In: *Physica C: Superconductivity and its Applications* 549.March (June 2018), pp. 164–170. URL: `https://linkinghub.elsevier.com/retrieve/pii/S0921453417303349`.

[17] S.O. Demokritov et al. "Bose-Einstein condensation of quasi-equilibrium magnons at room temperature under pumping". In: *Nature* 443.7110 (Sept. 2006), pp. 430–433. URL: `http://dx.doi.org/10.1038/nature05117`.

[18] A.V. Chumak, A.A. Serga, and B. Hillebrands. "Magnon transistor for all-magnon data processing". In: *Nature Communications* 5.1 (Dec. 2014), p. 4700. URL: `http://www.nature.com/articles/ncomms5700`.

[19] A.V. Chumak et al. "All-linear time reversal by a dynamic artificial crystal". In: *Nature Communications* 1.9 (Dec. 2010), p. 141. URL: `http://dx.doi.org/10.1038/ncomms1142`.

[20] M. Harder and C.-M. Hu. "Chapter Two - Cavity Spintronics: An Early Review of Recent Progress in the Study of Magnon–Photon Level Repulsion". In: ed. by Robert E Camley and Robert L Stamps. Vol. 69. Solid State Physics. Academic Press, 2018, pp. 47–121. URL: `http://www.sciencedirect.com/science/article/pii/S0081194718300018`.

[21] J.A. Haigh et al. "Triple-Resonant Brillouin Light Scattering in Magneto-Optical Cavities". In: *Physical Review Letters* 117.13 (Sept. 2016), p. 133602. arXiv: `1607.02985`. URL: `https://link.aps.org/doi/10.1103/PhysRevLett.117.133602`.

[22] A. Osada et al. “Cavity Optomagnonics with Spin-Orbit Coupled Photons”. In: *Phys. Rev. Lett.* 116.22 (June 2016). URL: http://dx.doi.org/10.1103/PhysRevLett.116.223601.

[23] X. Zhang et al. “Optomagnonic Whispering Gallery Microresonators”. In: *Physical Review Letters* 117.12 (Sept. 2016), p. 123605. arXiv: 1510.03545. URL: https://link.aps.org/doi/10.1103/PhysRevLett.117.123605.

[24] J. Graf et al. “Cavity optomagnonics with magnetic textures: Coupling a magnetic vortex to light”. In: *Physical Review B* 98.24 (Dec. 2018), p. 241406. arXiv: 1806.06727. URL: https://link.aps.org/doi/10.1103/PhysRevB.98.241406.

[25] A. Osada et al. “Brillouin Light Scattering by Magnetic Quasivortices in Cavity Optomagnonics”. In: *Physical Review Letters* 120.13 (Mar. 2018), p. 133602. arXiv: 1711.09319. URL: https://link.aps.org/doi/10.1103/PhysRevLett.120.133602.

[26] J.A. Haigh et al. “Selection rules for cavity-enhanced Brillouin light scattering from magnetostatic modes”. In: *Physical Review B* 97.21 (June 2018), p. 214423. arXiv: 1804.00965. URL: https://link.aps.org/doi/10.1103/PhysRevB.97.214423.

[27] H.J. Kimble. “The quantum internet”. In: *Nature* 453.7198 (June 2008), pp. 1023–1030. URL: http://www.nature.com/articles/nature07127.

[28] M.H. Devoret and R.J. Schoelkopf. “Superconducting Circuits for Quantum Information: An Outlook”. In: *Science* 339.6124 (2013), pp. 1169–1174. URL: http://www.sciencemag.org/cgi/doi/10.1126/science.1231930.

[29] Y. Tabuchi et al. “Quantum magnonics: The magnon meets the superconducting qubit”. In: *Comptes Rendus Physique* 17.7 (Aug. 2016), pp. 729–739. arXiv: 1508.05290. URL: https://linkinghub.elsevier.com/retrieve/pii/S1631070516300603.

[30] Y. Tabuchi et al. “Hybridizing Ferromagnetic Magnons and Microwave Photons in the Quantum Limit”. In: *Physical Review Letters* 113.8 (Aug. 2014), p. 083603. arXiv: 1405.1913. URL: https://link.aps.org/doi/10.1103/PhysRevLett.113.083603.

[31] Y. Tabuchi et al. “Coherent coupling between a ferromagnetic magnon and a superconducting qubit”. In: *Science* 349.6246 (July 2015), pp. 405–408. arXiv: 1410.3781. URL: http://science.sciencemag.org/content/349/6246/405.

[32] D. Lachance-Quirion et al. “Resolving quanta of collective spin excitations in a millimeter-sized ferromagnet”. In: *Science Advances* 3.7 (July 2017), e1603150. arXiv: 1610.00839. URL: http://advances.sciencemag.org/lookup/doi/10.1126/sciadv.1603150.

[33] A. Schneider et al. “Transmon Qubit in a Magnetic Field: Evolution of Coherence and Transition Frequency”. In: (2019), pp. 1–8. arXiv: 1904.00208. URL: http://arxiv.org/abs/1904.00208.

[34] A.G. Gurevich and G.A. Melkov. *Magnetization Oscillations and Waves*. CRC Press, Inc, 1996. URL: http://books.google.com/books?hl=en%7B%5C&%7Dlr=%7B%5C&%7Did=YgQtSvFIvFQC%7B%5C&%7Doi=fnd%7B%5C&%7Dpg=PR9%7B%5C&%7Ddq=Magnetization+Oscillations+Waves%7B%5C&%7Dots=Ptq5EAvcP4%7B%5C&%7Dsig=GGWX2%7B%5C_%7D%7B%5C_%7Duxp4FDmBwB51MzWBwo3o.

[35] D.D. Stancil and A. Prabhakar. *Spin Waves: Theory and Applications.* 1st ed. Boston, MA: Springer US, 2009, pp. 1–348. URL: `http://link.springer.com/10.1007/978-0-387-77865-5`.

[36] M.J. Hurben and C.E. Patton. “Theory of magnetostatic waves for in-plane magnetized isotropic films”. In: *Journal of Magnetism and Magnetic Materials* 139.3 (Jan. 1995), pp. 263–291. URL: `http://linkinghub.elsevier.com/retrieve/pii/0304885395900063`.

[37] L.R. Walker. “Resonant Modes of Ferromagnetic Spheroids”. In: *Journal of Applied Physics* 29.3 (Mar. 1958), pp. 318–323. URL: `http://aip.scitation.org/doi/10.1063/1.1723117`.

[38] B.A. Kalinikos and A.N. Slavin. “Theory of dipole-exchange spin wave spectrum for ferromagnetic films with mixed exchange boundary conditions”. In: *Journal of Physics C: Solid State Physics* 19.35 (Dec. 1986), pp. 7013–7033. URL: `http://stacks.iop.org/0022-3719/19/i=35/a=014?key=crossref.9081737748ccc34b4ad98884dc70157e`.

[39] D. Kleppner and R.J. Kolenkow. *An Introduction to Mechanics.* Cambridge: Cambridge University Press, 2010. URL: `https://www.cambridge.org/core/books/an-introduction-to-mechanics/5014FDB906B127C08616DA14C9EDA1E2`.

[40] R.P. Feynman, R.B. Leighton, and M. Sands. *The Feynman lectures on physics.* English. Reading, Mass.: Addison-Wesley Pub. Co., 1963.

[41] D. Polder. “VIII. On the theory of ferromagnetic resonance”. In: *The London, Edinburgh, and Dublin Philosophical Magazine and Journal of Science* 40.300 (Jan. 1949), pp. 99–115. URL: `http://www.tandfonline.com/doi/abs/10.1080/14786444908561215`.

[42] J.D. Jackson. *Classical electrodynamics.* 3rd ed. New York, {NY}: Wiley, 1999.

[43] J.C. Maxwell. “VIII. A dynamical theory of the electromagnetic field”. In: *Philosophical Transactions of the Royal Society of London* 155.2986 (Jan. 1865), pp. 459–512. URL: `http://www.royalsocietypublishing.org/doi/10.1098/rstl.1865.0008`.

[44] A.D.M. Walker and J.F. McKenzie. “Properties of electromagnetic waves in ferrites”. In: *Proceedings of the Royal Society of London. Series A, Mathematical and Physical Sciences* 399.1817 (1985), pp. 217–241. URL: `https://www.jstor.org/stable/2397689`.

[45] L.R. Walker. “Magnetostatic Modes in Ferromagnetic Resonance”. In: *Physical Review* 105.2 (Jan. 1957), pp. 390–399. URL: `https://link.aps.org/doi/10.1103/PhysRev.105.390`.

[46] P.C. Fletcher and R.O. Bell. “Ferrimagnetic Resonance Modes in Spheres”. In: *Journal of Applied Physics* 30.5 (May 1959), pp. 687–698. URL: `http://aip.scitation.org/doi/10.1063/1.1735216`.

[47] C. Kittel. “On the Theory of Ferromagnetic Resonance Absorption”. In: *Physical Review* 73.2 (Jan. 1948), pp. 155–161. URL: `https://link.aps.org/doi/10.1103/PhysRev.73.155`.

[48] R.W. Damon and H. Van De Vaart. “Propagation of Magnetostatic Spin Waves at Microwave Frequencies in a Normally-Magnetized Disk”. In: *Journal of Applied Physics* 36.11 (Nov. 1965), pp. 3453–3459. URL: `http://aip.scitation.org/doi/10.1063/1.1703018`.

[49] R.W. Damon and J.R. Eshbach. “Magnetostatic modes of a ferromagnet slab”. In: *Journal of Physics and Chemistry of Solids* 19.3-4 (May 1961), pp. 308–320. URL: `http://linkinghub.elsevier.com/retrieve/pii/0022369761900415`.

[50] G. Batey and G. Teleberg. *Principle of dilution refrigeration.* 2015. URL: `http://www.oxford-instruments.cn/OxfordInstruments/media/nanoscience/Priciples-of-dilution-refrigeration%7B%5C_%7Dv14.pdf`.

[51] R. Morris. “Studies towards quantum magnonics”. PhD thesis. University of Oxford, 2017. URL: `https://ora.ox.ac.uk/objects/uuid:89784b64-de31-457f-b9b2-54125c862632`.

[52] R. Heeres, P. de Groot, and M. Schaafma. *QTLab Measurement Software.* 2016. URL: `https://github.com/dchristle/qtlab`.

[53] M. Sparks. *Ferromagnetic-Relaxation Theory.* McGraw-Hill, 1964.

[54] T.H. Morgan. “Sex Limited Inheritance in Drosophila”. In: *Science* 32.812 (1910), pp. 120–122. URL: `http://www.jstor.org/stable/1635471`.

[55] C. Hauser et al. “Yttrium Iron Garnet Thin Films with Very Low Damping Obtained by Recrystallization of Amorphous Material”. In: *Scientific Reports* 6.1 (Aug. 2016), p. 20827. URL: `http://www.nature.com/articles/srep20827`.

[56] H.C. Chang et al. “Nanometer-Thick Yttrium Iron Garnet Films With Extremely Low Damping”. In: *IEEE Magnetics Letters* 5 (2014), pp. 1–4. URL: `https://doi.org/10.1109/LMAG.2014.2350958`.

[57] S. Klingler et al. “Gilbert damping of magnetostatic modes in a yttrium iron garnet sphere”. In: *Applied Physics Letters* 110.9 (Feb. 2017), p. 092409. arXiv: `1612.02360`. URL: `http://aip.scitation.org/doi/10.1063/1.4977423`.

[58] V. Cherepanov, I. Kolokolov, and V. L’vov. “The saga of YIG: Spectra, thermodynamics, interaction and relaxation of magnons in a complex magnet”. In: *Physics Reports* 229.3 (July 1993), pp. 81–144. URL: `http://linkinghub.elsevier.com/retrieve/pii/037015739390107O`.

[59] L.J. Cornelissen. “Magnon spin transport in magnetic insulators”. PhD thesis. University of Groningen, 2018. URL: `https://www.rug.nl/research/portal/files/59286993/Complete%7B%5C_%7Dthesis.pdf`.

[60] H.L. Glass. “Ferrite films for microwave and millimeter-wave devices”. In: *Proceedings of the IEEE* 76.2 (1988), pp. 151–158. URL: `http://ieeexplore.ieee.org/document/4391/`.

[61] S. Geller and M.A. Gilleo. “The crystal structure and ferrimagnetism of yttrium-iron garnet, Y3Fe2(FeO4)3”. In: *Journal of Physics and Chemistry of Solids* 3.1-2 (Jan. 1957), pp. 30–36. URL: `http://linkinghub.elsevier.com/retrieve/pii/0022369757900446`.

[62] S. Kimura and I. Shindo. "Single crystal growth of YIG by the floating zone method". In: *Journal of Crystal Growth* 41.2 (Dec. 1977), pp. 192–198. URL: `http://linkinghub.elsevier.com/retrieve/pii/0022024877900458`.

[63] P. Röschmann. "YIG Filters". In: *Philips technical review* 32.9/10/11/12 (1971), pp. 322–327. URL: `http://www.extra.research.philips.com/hera/people/aarts/%7B%5C_%7DPhilips%20Bound%20Archive/PTechReview/PTechReview-32-1971-322.pdf`.

[64] H. Tanbakuchi. "A Broadband Tracking YIG-Tuned Mixer for a State-of-the-Art Spectrum Analyzer". In: *17th European Microwave Conference, 1987*. IEEE, Oct. 1987, pp. 482–487. URL: `http://ieeexplore.ieee.org/document/4132389/`.

[65] M. Shone. "The technology of YIG film growth". In: *Circuits, Systems, and Signal Processing* 4.1-2 (Mar. 1985), pp. 89–103. URL: `http://link.springer.com/10.1007/BF01600074`.

[66] Y. Zhang et al. "Growth of Phase Pure Yttrium Iron Garnet Thin Films on Silicon: The Effect of Substrate and Postdeposition Annealing Temperatures". In: *IEEE Transactions on Magnetics* 51.11 (Nov. 2015), pp. 1–4. URL: `http://ieeexplore.ieee.org/document/7120983/`.

[67] S. Trudel et al. "Magnetic anisotropy, exchange and damping in cobalt-based full-Heusler compounds: an experimental review". In: *Journal of Physics D: Applied Physics* 43.19 (May 2010), p. 193001. URL: `http://stacks.iop.org/0022-3727/43/i=19/a=193001?key=crossref.73d992f879c99c4a85bf2caf28185cd6`.

[68] T. Sebastian et al. "Low-damping spin-wave propagation in a micro-structured Co 2 Mn 0.6 Fe 0.4 Si Heusler waveguide". In: *Applied Physics Letters* 100.11 (Mar. 2012), p. 112402. URL: `http://aip.scitation.org/doi/10.1063/1.3693391`.

[69] H.L. Liu et al. "Organic-based magnon spintronics". In: *Nature Materials* 17.4 (2018), pp. 308–312. URL: `http://dx.doi.org/10.1038/s41563-018-0035-3`.

[70] N. Zhu et al. "Low loss spin wave resonances in organic-based ferrimagnet vanadium tetracyanoethylene thin films". In: *Applied Physics Letters* 109.8 (Aug. 2016), p. 082402. URL: `http://aip.scitation.org/doi/10.1063/1.4961579`.

[71] R.G.E. Morris et al. "Strong coupling of magnons in a YIG sphere to photons in a planar superconducting resonator in the quantum limit". In: *Scientific Reports* 7.1 (Dec. 2017), p. 11511. arXiv: `1610.09963`. URL: `http://www.nature.com/articles/s41598-017-11835-4`.

[72] G. Grynberg et al. *Introduction to Quantum Optics*. Cambridge: Cambridge University Press, 2010. URL: `http://ebooks.cambridge.org/ref/id/CBO9780511778261`.

[73] S. Haroche and J.-M. Raimond. *Exploring the Quantum*. Oxford University Press, Aug. 2006. URL: `http://www.oxfordscholarship.com/view/10.1093/acprof:oso/9780198509141.001.0001/acprof-9780198509141`.

[74] D. Kleppner. "Inhibited Spontaneous Emission". In: *Phys. Rev. Lett.* 47.4 (July 1981), pp. 233–236. URL: `https://link.aps.org/doi/10.1103/PhysRevLett.47.233`.

[75] E. Yablonovitch. “Inhibited Spontaneous Emission in Solid-State Physics and Electronics”. In: *Physical Review Letters* 58.20 (May 1987), pp. 2059–2062. URL: `https://link.aps.org/doi/10.1103/PhysRevLett.58.2059`.

[76] S.J. van Enk, H.J. Kimble, and H. Mabuchi. “Quantum Information Processing in Cavity-QED”. In: *Quantum Information Processing* 3.1-5 (Oct. 2004), pp. 75–90. URL: `http://link.springer.com/10.1007/s11128-004-3104-2`.

[77] R.J. Thompson, G. Rempe, and H.J. Kimble. “Observation of normal-mode splitting for an atom in an optical cavity”. In: *Phys. Rev. Lett.* 68.8 (Feb. 1992), pp. 1132–1135. URL: `https://link.aps.org/doi/10.1103/PhysRevLett.68.1132`.

[78] A. Megrant et al. “Planar superconducting resonators with internal quality factors above one million”. In: *Applied Physics Letters* 100.11 (Mar. 2012), p. 113510. URL: `http://aip.scitation.org/doi/10.1063/1.3693409`.

[79] G. Nogues et al. “Seeing a single photon without destroying it”. In: *Nature* 400.6741 (July 1999), pp. 239–242. URL: `http://www.nature.com/articles/22275`.

[80] M.K. Tey et al. “Strong interaction between light and a single trapped atom without the need for a cavity”. In: *Nature Physics* 4.12 (Oct. 2008), pp. 924–927. URL: `http://www.nature.com/doifinder/10.1038/nphys1096`.

[81] A. Imamoğlu. “Cavity QED Based on Collective Magnetic Dipole Coupling: Spin Ensembles as Hybrid Two-Level Systems”. In: *Physical Review Letters* 102.8 (Feb. 2009), p. 083602. URL: `https://link.aps.org/doi/10.1103/PhysRevLett.102.083602`.

[82] C. Carr et al. “Nonequilibrium Phase Transition in a Dilute Rydberg Ensemble”. In: *Physical Review Letters* 111.11 (Sept. 2013), p. 113901. URL: `https://link.aps.org/doi/10.1103/PhysRevLett.111.113901`.

[83] P.L. Stanwix et al. “Coherence of nitrogen-vacancy electronic spin ensembles in diamond”. In: *Physical Review B* 82.20 (Nov. 2010), p. 201201. URL: `https://link.aps.org/doi/10.1103/PhysRevB.82.201201`.

[84] Y. Kubo et al. “Strong Coupling of a Spin Ensemble to a Superconducting Resonator”. In: *Phys. Rev. Lett.* 105.14 (Sept. 2010), p. 140502. URL: `https://link.aps.org/doi/10.1103/PhysRevLett.105.140502`.

[85] C.-M. Hu. “Dawn of Cavity Spintronics”. In: *Physics in Canada* 72.2 (2016), pp. 76–80. URL: `https://services.cap.ca/drupal/sites/cap.ca/files/article/3535/pic-72-2-offprint-c-m-hu-highres.pdf`.

[86] G.E.W. Bauer, K. Usami, and J. Sinova. *Spin Cavitronics 2018 Program.* 2018. URL: `https://www.spice.uni-mainz.de/spin-cavitronics-2018-program/`.

[87] H. Huebl et al. “High Cooperativity in Coupled Microwave Resonator Ferrimagnetic Insulator Hybrids”. In: *Physical Review Letters* 111.12 (Sept. 2013), p. 127003. arXiv: `1207.6039`. URL: `https://link.aps.org/doi/10.1103/PhysRevLett.111.127003`.

[88] X.F. Zhang et al. “Strongly Coupled Magnons and Cavity Microwave Photons”. In: *Physical Review Letters* 113.15 (Oct. 2014), p. 156401. URL: `https://link.aps.org/doi/10.1103/PhysRevLett.113.156401`.

[89] D.K. Zhang et al. “Cavity quantum electrodynamics with ferromagnetic magnons in a small yttrium-iron-garnet sphere”. In: *npj Quantum Information* 1.1 (Dec. 2015), p. 15014. arXiv: `1512.00983`. URL: `http://www.nature.com/articles/npjqi201514`.

[90] I. Boventer et al. “Complex temperature dependence of coupling and dissipation of cavity magnon polaritons from millikelvin to room temperature”. In: *Physical Review B* 97.18 (May 2018), p. 184420. arXiv: `1801.01439`. URL: `https://link.aps.org/doi/10.1103/PhysRevB.97.184420`.

[91] X. Zhang et al. “Magnon dark modes and gradient memory”. In: *Nature Communications* 6 (2015), p. 18. arXiv: `arXiv:1507.02791v1`. URL: `http://dx.doi.org/10.1038/ncomms9914`.

[92] Y.-P. Wang et al. “Magnon Kerr effect in a strongly coupled cavity-magnon system”. In: *Physical Review B* 94.22 (Dec. 2016), p. 224410. arXiv: `1609.07891`. URL: `https://link.aps.org/doi/10.1103/PhysRevB.94.224410`.

[93] X.F. Zhang et al. “Cavity magnomechanics”. In: *Science Advances* 2.3 (Mar. 2016), e1501286. arXiv: `1511.03680`. URL: `http://advances.sciencemag.org/lookup/doi/10.1126/sciadv.1501286`.

[94] Y.P. Wang et al. “Bistability of Cavity Magnon Polaritons”. In: *Physical Review Letters* 120.5 (Jan. 2018), p. 057202. arXiv: `1707.06509`. URL: `https://link.aps.org/doi/10.1103/PhysRevLett.120.057202`.

[95] L.H. Bai et al. “Spin Pumping in Electrodynamically Coupled Magnon-Photon Systems”. In: *Physical Review Letters* 114.22 (June 2015), p. 227201. arXiv: `1504.01335`. URL: `https://link.aps.org/doi/10.1103/PhysRevLett.114.227201`.

[96] X. Zhang et al. “Superstrong coupling of thin film magnetostatic waves with microwave cavity”. In: *Journal of Applied Physics* 119.2 (2016). URL: `http://dx.doi.org/10.1063/1.4939134`.

[97] H. Maier-Flaig et al. “Tunable magnon-photon coupling in a compensating ferrimagnet—from weak to strong coupling”. In: *Applied Physics Letters* 110.13 (Mar. 2017), p. 132401. arXiv: `1701.08969`. URL: `http://aip.scitation.org/doi/10.1063/1.4979409`.

[98] J. Bourhill et al. “Ultrahigh cooperativity interactions between magnons and resonant photons in a YIG sphere”. In: *Physical Review B* 93.14 (Apr. 2016), p. 144420. URL: `https://link.aps.org/doi/10.1103/PhysRevB.93.144420`.

[99] P. Hyde et al. “Indirect coupling between two cavity modes via ferromagnetic resonance”. In: *Applied Physics Letters* 109.15 (Oct. 2016), p. 152405. arXiv: `1606.03469`. URL: `http://aip.scitation.org/doi/10.1063/1.4964602`.

[100] M. Harder et al. “Spin dynamical phase and antiresonance in a strongly coupled magnon-photon system”. In: *Physical Review B* 94.5 (Aug. 2016), p. 054403. arXiv: `1606.03056`. URL: `https://link.aps.org/doi/10.1103/PhysRevB.94.054403`.

[101] S. Probst et al. “Three-dimensional cavity quantum electrodynamics with a rare-earth spin ensemble”. In: *Physical Review B* 90.10 (Sept. 2014), p. 100404. arXiv: `1406.3535`. URL: `https://link.aps.org/doi/10.1103/PhysRevB.90.100404`.

[102] W.G. Farr et al. “Evidence of dilute ferromagnetism in rare-earth doped yttrium aluminium garnet”. In: *Applied Physics Letters* 107.12 (Sept. 2015), p. 122401. arXiv: `1412.0086`. URL: `http://aip.scitation.org/doi/10.1063/1.4931432`.

[103] M. Goryachev et al. “High-Cooperativity Cavity QED with Magnons at Microwave Frequencies”. In: *Physical Review Applied* 2.5 (Nov. 2014), p. 054002. URL: `https://link.aps.org/doi/10.1103/PhysRevApplied.2.054002`.

[104] N. Kostylev, M. Goryachev, and M.E. Tobar. “Superstrong coupling of a microwave cavity to yttrium iron garnet magnons”. In: *Applied Physics Letters* 108.6 (2016). arXiv: `1508.04967`. URL: `http://dx.doi.org/10.1063/1.4941730`.

[105] M. Goryachev, M. Kostylev, and M.E. Tobar. “Strong Coupling of 3D Cavity Photons to Travelling Magnons At Low Temperatures”. In: (2017), pp. 1–5. arXiv: `1710.06601`. URL: `http://arxiv.org/abs/1710.06601`.

[106] N.J. Lambert, J.A. Haigh, and A.J. Ferguson. “Identification of spin wave modes in yttrium iron garnet strongly coupled to a co-axial cavity”. In: *Journal of Applied Physics* 117.5 (Feb. 2015), p. 053910. URL: `http://aip.scitation.org/doi/10.1063/1.4907694`.

[107] N.J. Lambert et al. “Cavity-mediated coherent coupling of magnetic moments”. In: *Phys. Rev. A* 93.2 (Feb. 2016). URL: `http://dx.doi.org/10.1103/PhysRevA.93.021803`.

[108] J.A. Haigh et al. “Dispersive readout of ferromagnetic resonance for strongly coupled magnons and microwave photons”. In: *Physical Review B* 91.10 (Mar. 2015), p. 104410. arXiv: `arXiv:1506.05631v1`. URL: `https://link.aps.org/doi/10.1103/PhysRevB.91.104410`.

[109] B.M. Yao et al. “Theory and experiment on cavity magnon-polariton in the one-dimensional configuration”. In: *Physical Review B* 92.18 (Nov. 2015), p. 184407. arXiv: `1509.05804`. URL: `https://link.aps.org/doi/10.1103/PhysRevB.92.184407`.

[110] M. Harder et al. “Level Attraction Due to Dissipative Magnon-Photon Coupling”. In: *Physical Review Letters* 121.13 (Sept. 2018), p. 137203. arXiv: `1809.01233`. URL: `https://link.aps.org/doi/10.1103/PhysRevLett.121.137203`.

[111] H. Maier-Flaig et al. “Spin pumping in strongly coupled magnon-photon systems”. In: *Phys. Rev. B* 94.5 (Aug. 2016). URL: `http://dx.doi.org/10.1103/PhysRevB.94.054433`.

[112] V. Castel, A. Manchec, and J. Ben Youssef. “Control of Magnon-Photon Coupling Strength in a Planar Resonator/Yttrium-Iron-Garnet Thin-Film Configuration”. In: *IEEE Magnetics Letters* 8 (2017), pp. 1–5. arXiv: `1607.02358`. URL: `http://ieeexplore.ieee.org/document/7769241/`.

[113] J.W. Rao et al. “Characterization of the non-resonant radiation damping in coupled cavity photon magnon system”. In: *Applied Physics Letters* 110.26 (June 2017), p. 262404. URL: `http://aip.scitation.org/doi/10.1063/1.4990977`.

[114] B. Bhoi et al. “Study of photon–magnon coupling in a YIG-film split-ring resonant system”. In: *Journal of Applied Physics* 116.24 (2014), p. 243906. URL: `https://doi.org/10.1063/1.4904857`.

[115] S. Kaur et al. “Voltage control of cavity magnon polariton”. In: *Applied Physics Letters* 109.3 (July 2016), p. 032404. URL: `http://aip.scitation.org/doi/10.1063/1.4959140`.

[116] B. Bhoi et al. “Robust magnon-photon coupling in a planar-geometry hybrid of inverted split-ring resonator and YIG film”. In: *Scientific Reports* 7.1 (2017), pp. 1–12. URL: `http://dx.doi.org/10.1038/s41598-017-12215-8`.

[117] C. W. Zollitsch et al. “High cooperativity coupling between a phosphorus donor spin ensemble and a superconducting microwave resonator”. In: *Applied Physics Letters* 107.14 (Oct. 2015), p. 142105. arXiv: `1507.03739`. URL: `http://aip.scitation.org/doi/10.1063/1.4932658`.

[118] J.T. Hou and L.Q. Liu. “Strong Coupling between Microwave Photons and Nanomagnet Magnons”. In: (2019), pp. 1–7. arXiv: `1903.01887`. URL: `http://arxiv.org/abs/1903.01887`.

[119] P. Forn-Díaz et al. “Ultrastrong coupling regimes of light-matter interaction”. In: (2018). arXiv: `1804.09275`. URL: `http://arxiv.org/abs/1804.09275`.

[120] B.Z. Rameshti, Y.S. Cao, and G.E.W. Bauer. “Magnetic spheres in microwave cavities”. In: *Physical Review B* 91.21 (June 2015), p. 214430. arXiv: `1503.02419`. URL: `https://link.aps.org/doi/10.1103/PhysRevB.91.214430`.

[121] R.N. Simons. *Coplanar waveguide circuits, components, and systems.* John Wiley & Sons, 2001, pp. 1–464.

[122] D.M. Pozar. *Microwave Engineering.* 4th ed. John Wiley & Sons, 2011, pp. 1–752.

[123] A. Blais et al. “Cavity quantum electrodynamics for superconducting electrical circuits: An architecture for quantum computation”. In: *Physical Review A* 69.6 (June 2004), p. 062320. URL: `https://link.aps.org/doi/10.1103/PhysRevA.69.062320`.

[124] C. Reale. “Thickness and temperature dependence of the critical magnetic field of thin superconducting films of the aluminium group metals”. In: *Acta Physica Academiae Scientiarum Hungaricae* 37.1-2 (June 1974), pp. 53–60. URL: `http://link.springer.com/10.1007/BF03157926`.

[125] Y. Asada and H. Nosé. “Superconductivity of Niobium Films”. In: *Journal of the Physical Society of Japan* 26.2 (Feb. 1969), pp. 347–354. URL: `http://journals.jps.jp/doi/10.1143/JPSJ.26.347`.

[126] D. Bothner et al. “Magnetic hysteresis effects in superconducting coplanar microwave resonators”. In: *Physical Review B* 86.1 (July 2012), p. 014517. URL: `https://link.aps.org/doi/10.1103/PhysRevB.86.014517`.

[127] H.J. Pain. *The physics of vibrations and waves.* London ; New York: Wiley, 1976.

[128] S. Kosen et al. “Measurement of a magnonic crystal at millikelvin temperatures”. In: *Applied Physics Letters* 112.1 (Jan. 2018), p. 012402. arXiv: `1711.00958`. URL: `http://aip.scitation.org/doi/10.1063/1.5011767`.

[129] A.D. Karenowska et al. “Oscillatory Energy Exchange between Waves Coupled by a Dynamic Artificial Crystal”. In: *Phys. Rev. Lett.* 108.1 (Jan. 2012). URL: `http://dx.doi.org/10.1103/PhysRevLett.108.015505`.

[130] A.V. Chumak et al. “Storage-Recovery Phenomenon in Magnonic Crystal”. In: *Phys. Rev. Lett.* 108.25 (June 2012). arXiv: `1107.0984`. URL: `http://dx.doi.org/10.1103/PhysRevLett.108.257207`.

[131] D.A. Bozhko et al. “Formation of Bose-Einstein magnon condensate via dipolar and exchange thermalization channels”. In: *Low Temperature Physics* 41.10 (Oct. 2015), pp. 801–805. URL: `http://dx.doi.org/10.1063/1.4932354`.

[132] A.D. Karenowska et al. “Magnonic crystal based forced dominant wavenumber selection in a spin-wave active ring”. In: *Applied Physics Letters* 96.8 (Feb. 2010), p. 082505. arXiv: `0912.2029`. URL: `http://aip.scitation.org/doi/10.1063/1.3318258`.

[133] A.A. Nikitin et al. “A spin-wave logic gate based on a width-modulated dynamic magnonic crystal”. In: *Applied Physics Letters* 106.10 (2015). arXiv: `1501.03486v2`. URL: `http://dx.doi.org/10.1063/1.4914506`.

[134] A.V. Chumak et al. “Scattering of backward spin waves in a one-dimensional magnonic crystal”. In: *Applied Physics Letters* 93.2 (July 2008), p. 022508. arXiv: `0805.4142`. URL: `http://aip.scitation.org/doi/10.1063/1.2963027`.

[135] A.V. Chumak et al. “Scattering of surface and volume spin waves in a magnonic crystal”. In: *Applied Physics Letters* 94.17 (Apr. 2009), p. 172511. arXiv: `0903.3686`. URL: `http://aip.scitation.org/doi/10.1063/1.3127227`.

[136] A.V. Chumak et al. “Spin-wave propagation in a microstructured magnonic crystal”. In: *Applied Physics Letters* 95.26 (Dec. 2009), p. 262508. arXiv: `0911.1920`. URL: `http://aip.scitation.org/doi/10.1063/1.3279138`.

[137] B. Obry et al. “A micro-structured ion-implanted magnonic crystal”. In: *Applied Physics Letters* 102.20 (May 2013), p. 202403. arXiv: `arXiv:1304.7122v1`. URL: `http://aip.scitation.org/doi/10.1063/1.4807721`.

[138] A.V. Chumak et al. “A current-controlled, dynamic magnonic crystal”. In: *Journal of Physics D: Applied Physics* 42.20 (2009), p. 205005. arXiv: `0904.0332`. URL: `http://stacks.iop.org/0022-3727/42/i=20/a=205005`.

[139] M. Vogel et al. “Optically reconfigurable magnetic materials”. In: *Nature Physics* 11.6 (2015), pp. 487–491. URL: `http://www.nature.com/nphys/journal/v11/n6/full/nphys3325.html?WT.ec%7B%5C_%7Did=NPHYS-201506`.

[140] R.G. Kryshtal and A.V. Medved. “Surface acoustic wave in yttrium iron garnet as tunable magnonic crystals for sensors and signal processing applications”. In: *Applied Physics Letters* 100.19 (May 2012), p. 192410. URL: `http://aip.scitation.org/doi/10.1063/1.4714507`.

[141] P. Markors and C.M. Soukoulis. *Wave Propagation: From Electrons to Photonic Crystals and Left-Handed Materials.* Princeton University Press, 2008, pp. 1–376.

[142] A.F. Van Loo, R.G.E. Morris, and A.D. Karenowska. “Time-Resolved Measurements of Surface Spin-Wave Pulses at Millikelvin Temperatures”. In: *Physical Review Applied* 10.4 (2018), p. 1. arXiv: `1610.08402`. URL: `https://doi.org/10.1103/PhysRevApplied.10.044070`.

[143] H. Maier-Flaig et al. “Temperature dependent magnetic damping of yttrium iron garnet spheres”. In: *Physical Review B* 95.21 (Mar. 2017), p. 214423. arXiv: `1703.09444`. URL: `http://link.aps.org/doi/10.1103/PhysRevB.95.214423`.

[144] E.G. Spencer, R.C. LeCraw, and A.M. Clogston. “Low-Temperature Line-Width Maximum in Yttrium Iron Garnet”. In: *Physical Review Letters* 3.1 (July 1959), pp. 32–33. URL: `https://link.aps.org/doi/10.1103/PhysRevLett.3.32`.

[145] M. Haidar et al. “Thickness- and temperature-dependent magnetodynamic properties of yttrium iron garnet thin films”. In: *Journal of Applied Physics* 117.17 (May 2015), p. 17D119. URL: `http://aip.scitation.org/doi/10.1063/1.4914363`.

[146] C.L. Jermain et al. “Increased low-temperature damping in yttrium iron garnet thin films”. In: *Physical Review B* 95.17 (May 2017), p. 174411. arXiv: `1612.01954`. URL: `http://link.aps.org/doi/10.1103/PhysRevB.95.174411`.

[147] W.A. Phillips. “Two-level states in glasses”. In: *Reports on Progress in Physics* 50.12 (Dec. 1987), pp. 1657–1708. URL: `http://stacks.iop.org/0034-4885/50/i=12/a=003?key=crossref.66639792cf567885bb142822e2ebe90a`.

[148] V.V. Danilov et al. “Low-temperature ferromagnetic resonance in epitaxial garnet films on paramagnetic substrates”. In: *Soviet Physics Journal* 32.4 (Apr. 1989), pp. 276–280. URL: `http://link.springer.com/10.1007/BF00897267`.

[149] P. Schiffer et al. “Investigation of the Field Induced Antiferromagnetic Phase Transition in the Frustrated Magnet: Gadolinium Gallium Garnet”. In: *Physical Review Letters* 73.18 (Oct. 1994), pp. 2500–2503. URL: `https://link.aps.org/doi/10.1103/PhysRevLett.73.2500`.

[150] P. Schiffer et al. “Frustration Induced Spin Freezing in a Site-Ordered Magnet: Gadolinium Gallium Garnet”. In: *Physical Review Letters* 74.12 (Mar. 1995), pp. 2379–2382. URL: `https://link.aps.org/doi/10.1103/PhysRevLett.74.2379`.

[151] L.R. Walker. “Ferromagnetic-Relaxation Theory. Marshall Sparks. McGraw-Hill, New York, 1964. xii + 227 pp. Illus. $12.50”. In: *Science* 148.3667 (1965), p. 218. URL: `http://science.sciencemag.org/content/148/3667/218.1`.

[152] T. Kasuya and R.C. LeCraw. “Relaxation Mechanisms in Ferromagnetic Resonance”. In: *Physical Review Letters* 6.5 (Mar. 1961), pp. 223–225. URL: `https://link.aps.org/doi/10.1103/PhysRevLett.6.223`.

[153] I.V. Kolokolov, V.S. L’vov, and V.B. Cherepanov. “Magnon interaction and relaxation in YIG, a twenty-sublattice ferromagnet”. In: *Soviet Journal of Experimental and Theoretical Physics* 59.5 (1984), pp. 1131–1139. URL: `http://jetp.ac.ru/cgi-bin/dn/e%7B%5C_%7D059%7B%5C_%7D05%7B%5C_%7D1131.pdf`.

[154] A.G. Gurevich and A.N. Anisimov. “Intrinsic spin wave relaxation processes in yttrium iron garnets”. In: *Soviet Journal of Experimental and Theoretical Physics* 41.2 (1975), pp. 336–341. URL: `http://www.jetp.ac.ru/cgi-bin/dn/e%7B%5C_%7D041%7B%5C_%7D02%7B%5C_%7D0336.pdf`.

[155] A.M. Clogston et al. “Ferromagnetic resonance line width in insulating materials”. In: *Journal of Physics and Chemistry of Solids* 1.3 (Nov. 1956), pp. 129–136. URL: `http://linkinghub.elsevier.com/retrieve/pii/0022369756900191`.

[156] C.R. Buffler. “Ferromagnetic Resonance near the Upper Limit of the Spin Wave Manifold”. In: *Journal of Applied Physics* 30.4 (Apr. 1959), S172–S175. URL: `http://aip.scitation.org/doi/10.1063/1.2185872`.

[157] R.C. LeCraw, E.G. Spencer, and C.S. Porter. “Ferromagnetic Resonance Line Width in Yttrium Iron Garnet Single Crystals”. In: *Physical Review* 110.6 (June 1958), pp. 1311–1313. arXiv: `0504598 [cond-mat]`. URL: `https://link.aps.org/doi/10.1103/PhysRev.110.1311`.

[158] M. Sparks, R. Loudon, and C. Kittel. “Ferromagnetic Relaxation. I. Theory of the Relaxation of the Uniform Precession and the Degenerate Spectrum in Insulators at Low Temperatures”. In: *Physical Review* 122.3 (May 1961), pp. 791–803. URL: `https://link.aps.org/doi/10.1103/PhysRev.122.791`.

[159] I.H. Solt. “Temperature Dependence of YIG Magnetization”. In: *Journal of Applied Physics* 33.3 (Mar. 1962), pp. 1189–1191. URL: `http://aip.scitation.org/doi/10.1063/1.1728651`.

[160] A.I. Akhiezer, V.G. Bar’yakhtar, and S.V. Peletminskii. *Spin Waves.* Amsterdam: North-Holland, 1968.

[161] J.F. Dillon and J.W. Nielsen. “Effects of Rare Earth Impurities on Ferrimagnetic Resonance in Yttrium Iron Garnet”. In: *Physical Review Letters* 3.1 (July 1959), pp. 30–31. URL: `https://link.aps.org/doi/10.1103/PhysRevLett.3.30`.

[162] J.F. Dillon. “Ferrimagnetic Resonance in Rare-Earth-Doped Yttrium Iron Garnet. III. Linewidth”. In: *Physical Review* 127.5 (Sept. 1962), pp. 1495–1501. URL: `https://link.aps.org/doi/10.1103/PhysRev.127.1495`.

[163] R.W. Teale and K. Tweedale. “Ytterbium-ion relaxation in ferrimagnetic resonance”. In: *Physics Letters* 1.7 (July 1962), pp. 298–300. URL: `http://linkinghub.elsevier.com/retrieve/pii/0031916362913926`.

[164] P.E. Seiden. “Ferrimagnetic Resonance Relaxation in Rare-Earth Iron Garnets”. In: *Journal of Applied Physics* 35.3 (Mar. 1964), pp. 891–891. URL: `http://aip.scitation.org/doi/10.1063/1.1713522`.

[165] L. Mihalceanu et al. “Temperature-dependent relaxation of dipole-exchange magnons in yttrium iron garnet films”. In: *Physical Review B* 97.21 (June 2018), p. 214405. arXiv: `1711.07517`. URL: `https://link.aps.org/doi/10.1103/PhysRevB.97.214405`.

[166] S. Geller. “Magnetic Interactions and Distribution of Ions in the Garnets”. In: *Journal of Applied Physics* 31.5 (May 1960), S30–S37. URL: `http://aip.scitation.org/doi/10.1063/1.1984593`.

[167] S. Geller et al. “Substitutions of Divalent Transition Metal Ions in Yttrium Iron Garnet”. In: *Journal of Applied Physics* 33.3 (Mar. 1962), pp. 1195–1196. URL: `http://aip.scitation.org/doi/10.1063/1.1728655`.

[168] B.H. Clarke, K. Tweedale, and R.W. Teale. “Rare-Earth Ion Relaxation Time and G Tensor in Rare-Earth-Doped Yttrium Iron Garnet. I. Ytterbium”. In: *Physical Review* 139.6A (Sept. 1965), A1933–A1943. URL: `https://link.aps.org/doi/10.1103/PhysRev.139.A1933`.

[169] A.G. Gurevich, A.N. Ageev, and M.I. Klinger. “Resonance in Ferrimagnets Containing Paramagnetic Ions with Near Crossing Energy Levels”. In: *Journal of Applied Physics* 41.3 (Mar. 1970), pp. 1295–1302. URL: `http://aip.scitation.org/doi/10.1063/1.1658916`.

[170] A.M. Clogston. “Relaxation Phenomena in Ferrites”. In: *Bell System Technical Journal* 34.4 (July 1955), pp. 739–760. URL: `http://ieeexplore.ieee.org/lpdocs/epic03/wrapper.htm?arnumber=6771685`.

[171] F. Hartmann-Boutron. “Effect of Rare-Earth Impurities on the Ferrimagnetic Resonance and Nuclear Relaxation in Yttrium Iron Garnet”. In: *Journal of Applied Physics* 35.3 (Mar. 1964), pp. 889–891. URL: `http://aip.scitation.org/doi/10.1063/1.1713521`.

[172] B.H. Clarke. “Rare-Earth Ion Relaxation Time and G Tensor in Rare-Earth-Doped Yttrium Iron Garnet. II. Neodymium”. In: *Physical Review* 139.6A (Sept. 1965), A1944–A1948. URL: `https://link.aps.org/doi/10.1103/PhysRev.139.A1944`.

[173] R. Orbach. “Spin-lattice relaxation in rare-earth salts”. In: *Proceedings of the Royal Society of London. Series A. Mathematical and Physical Sciences* 264.1319 (Dec. 1961), pp. 458–484. URL: `http://www.royalsocietypublishing.org/doi/10.1098/rspa.1961.0211`.

[174] D.I. Tchernev. “Effect of Low-Temperature Magnetic Anneal on the Linewidth of Garnets Containing Fe 2+ Ions”. In: *Journal of Applied Physics* 38.3 (Mar. 1967), pp. 1046–1047. URL: `http://aip.scitation.org/doi/10.1063/1.1709477`.

[175] D.I. Tchernev. “Temperature Dependence of the Linewidth of Garnets Containing Fe 4+ Ions”. In: *Journal of Applied Physics* 39.2 (Feb. 1968), pp. 826–827. URL: `http://aip.scitation.org/doi/10.1063/1.2163630`.

[176] T.S. Hartwick and J. Smit. “Ferromagnetic Resonance in Si-Doped YIG”. In: *Journal of Applied Physics* 39.2 (Feb. 1968), pp. 827–827. URL: `http://aip.scitation.org/doi/10.1063/1.2163631`.

[177] P. Hansen, W. Tolksdorf, and J. Schuldt. “Anisotropy and magnetostriction of germanium-substituted yttrium iron garnet”. In: *Journal of Applied Physics* 43.11 (Nov. 1972), pp. 4740–4746. URL: `http://aip.scitation.org/doi/10.1063/1.1660999`.

[178] H.P.J. Wijn and H. van der Heide. “A Richter Type After-Effect in Ferrites Containing Ferrous and Ferric Ions”. In: *Reviews of Modern Physics* 25.1 (Jan. 1953), pp. 98–99. URL: `https://link.aps.org/doi/10.1103/RevModPhys.25.98`.

[179] E.G. Spencer, R.C. LeCraw, and R.C. Linares. “Low-Temperature Ferromagnetic Relaxation in Yttrium Iron Garnet”. In: *Physical Review* 123.6 (Sept. 1961), pp. 1937–1938. URL: `https://link.aps.org/doi/10.1103/PhysRev.123.1937`.

[180] W.A. Yager, J.K. Galt, and F.R. Merritt. “Ferromagnetic Resonance in Two Nickel-Iron Ferrites”. In: *Physical Review* 99.4 (Aug. 1955), pp. 1203–1210. URL: `https://link.aps.org/doi/10.1103/PhysRev.99.1203`.

[181] J.H. Judy. “Anisotropic Magnetic Resonance and Relaxation in Silicon-Substituted YIG”. In: *Journal of Applied Physics* 37.3 (Mar. 1966), pp. 1328–1330. URL: `http://aip.scitation.org/doi/10.1063/1.1708455`.

[182] D.J. Epstein and L. Tocci. “High temperature resonance losses in silicon-doped yttrium-iron garnet (YIG)”. In: *Applied Physics Letters* 11.2 (July 1967), pp. 55–58. URL: `http://aip.scitation.org/doi/10.1063/1.1755026`.

[183] C. Kittel. “Theory of Ferromagnetic Resonance in Rare Earth Garnets. I. g Values”. In: *Physical Review* 115.6 (Sept. 1959), pp. 1587–1590. URL: `https://link.aps.org/doi/10.1103/PhysRev.115.1587`.

[184] P.G. De Gennes, C. Kittel, and A.M. Portis. “Theory of Ferromagnetic Resonance in Rare Earth Garnets. II. Line Widths”. In: *Physical Review* 116.2 (Oct. 1959), pp. 323–330. URL: `https://link.aps.org/doi/10.1103/PhysRev.116.323`.

[185] J.H. Van Vleck. “Ferrimagnetic Resonance of Rare-Earth-Doped Iron Garnets”. In: *Journal of Applied Physics* 35.3 (Mar. 1964), pp. 882–888. URL: `http://aip.scitation.org/doi/10.1063/1.1713520`.

[186] M. Pfirrmann et al. “Magnons at low excitations: Observation of incoherent coupling to a bath of two-level-systems”. In: (2019), pp. 1–8. arXiv: `1903.03981`. URL: `http://arxiv.org/abs/1903.03981`.

[187] P.W. Anderson, B.I. Halperin, and C.M. Varma. “Anomalous low-temperature thermal properties of glasses and spin glasses”. In: *Philosophical Magazine* 25.1 (Jan. 1972), pp. 1–9. arXiv: `arXiv:1011.1669v3`. URL: `http://www.tandfonline.com/doi/abs/10.1080/14786437208229210`.

[188] J. Zmuidzinas. “Superconducting Microresonators: Physics and Applications”. In: *Annual Review of Condensed Matter Physics* 3.1 (Mar. 2012), pp. 169–214. URL: `http://www.annualreviews.org/doi/10.1146/annurev-conmatphys-020911-125022`.

[189] J.M. Martinis et al. “Decoherence in Josephson Qubits from Dielectric Loss”. In: *Physical Review Letters* 95.21 (Nov. 2005), p. 210503. arXiv: `0507622 [cond-mat]`. URL: `https://link.aps.org/doi/10.1103/PhysRevLett.95.210503`.

[190] S. Kosen et al. “Microwave magnon damping in YIG films at millikelvin temperatures”. In: (Mar. 2019), pp. 2–6. arXiv: `1903.02527`. URL: `http://arxiv.org/abs/1903.02527`.

[191] O.A. Petrenko et al. “Magnetic frustration and order in gadolinium gallium garnet”. In: *Physica B: Condensed Matter* 266.1-2 (May 1999), pp. 41–48. URL: `http://linkinghub.elsevier.com/retrieve/pii/S0921452698014902`.

[192] V.V. Danilov and A.Y. Nechiporuk. “Experimental investigation of the quantum amplification effect for magnetostatic waves in ferrite-paramagnet structures”. In: *Technical Physics Letters* 28.5 (May 2002), pp. 369–370. URL: `http://link.springer.com/10.1134/1.1482739`.

[193] A. Rousseau, J.-M. Parent, and J.A. Quilliam. “Anisotropic phase diagram and spin fluctuations of the hyperkagome magnet Gd3Ga5O12 as revealed by sound velocity measurements”. In: *Physical Review B* 96.6 (Aug. 2017), 060411(R). arXiv: `1708.04916`. URL: `https://link.aps.org/doi/10.1103/PhysRevB.96.060411`.

[194] I.S. Maksymov and M. Kostylev. “Broadband stripline ferromagnetic resonance spectroscopy of ferromagnetic films, multilayers and nanostructures”. In: *Physica E: Low-dimensional Systems and Nanostructures* 69 (May 2015), pp. 253–293. URL: `https://linkinghub.elsevier.com/retrieve/pii/S1386947714004664`.

[195] E. Schlömann, J.J. Green, and U. Milano. “Recent Developments in Ferromagnetic Resonance at High Power Levels”. In: *Journal of Applied Physics* 31.5 (May 1960), S386–S395. URL: `http://aip.scitation.org/doi/10.1063/1.1984759`.

[196] M.A.W. Schoen et al. “Radiative damping in waveguide-based ferromagnetic resonance measured via analysis of perpendicular standing spin waves in sputtered permalloy films”. In: *Physical Review B* 92.18 (Nov. 2015), p. 184417. arXiv: `1508.05265`. URL: `https://link.aps.org/doi/10.1103/PhysRevB.92.184417`.

[197] P. Landeros, R.E. Arias, and D.L. Mills. “Two magnon scattering in ultrathin ferromagnets: The case where the magnetization is out of plane”. In: *Physical Review B* 77.21 (June 2008), p. 214405. URL: `https://link.aps.org/doi/10.1103/PhysRevB.77.214405`.

[198] M.J. Hurben and C.E. Patton. “Theory of two magnon scattering microwave relaxation and ferromagnetic resonance linewidth in magnetic thin films”. In: *Journal of Applied Physics* 83.8 (Apr. 1998), pp. 4344–4365. URL: `http://aip.scitation.org/doi/10.1063/1.367194`.

[199] R.D. McMichael and P. Krivosik. “Classical Model of Extrinsic Ferromagnetic Resonance Linewidth in Ultrathin Films”. In: *IEEE Transactions on Magnetics* 40.1 (Jan. 2004), pp. 2–11. URL: `http://ieeexplore.ieee.org/document/1264116/`.

[200] K.Y. Guslienko et al. “Effective dipolar boundary conditions for dynamic magnetization in thin magnetic stripes”. In: *Physical Review B* 66.13 (2002), p. 132402. URL: `https://link.aps.org/doi/10.1103/PhysRevB.66.132402`.

[201] K .Y. Guslienko, R.W. Chantrell, and A.N. Slavin. “Dipolar localization of quantized spin-wave modes in thin rectangular magnetic elements”. In: *Phys. Rev. B* 68.2 (July 2003), p. 24422. URL: `http://link.aps.org/doi/10.1103/PhysRevB.68.024422`.

[202] M. Kostylev. “Coupling of microwave magnetic dynamics in thin ferromagnetic films to stripline transducers in the geometry of the broadband stripline ferromagnetic resonance”. In: *Journal of Applied Physics* 119.1 (Jan. 2016), p. 013901. arXiv: `1511.01201`. URL: `http://aip.scitation.org/doi/10.1063/1.4939470`.

[203] M. Von Schickfus and S. Hunklinger. “Saturation of the dielectric absorption of vitreous silica at low temperatures”. In: *Physics Letters A* 64.1 (Nov. 1977), pp. 144–146. URL: `http://linkinghub.elsevier.com/retrieve/pii/0375960177905588`.

[204] P. Lodahl et al. “Chiral quantum optics”. In: *Nature* 541.7638 (Jan. 2017), pp. 473–480. URL: `http://www.nature.com/articles/nature21037`.

[205] M. Levy et al. “Narrow-Linewidth Yttrium Iron Garnet Films for Heterogeneous Integration”. In: *MRS Proceedings* 603 (Jan. 1999), p. 119. URL: `http://journals.cambridge.org/abstract%7B%5C_%7DS1946427400181126`.